Low temperature oxidation of VOCs in air by catalytic ozonation

A Thesis Submitted to the College of

Graduate Studies and Research

In Partial Fulfillment of the Requirements

For the Degree of Doctor of Philosophy

In the Department of Chemical & Biological Engineering

University of Saskatchewan

Saskatoon

By

Ebrahim Rezaei Geshnizgani

PERMISSION TO USE

In presenting this thesis in partial fulfilment of the requirements for a Postgraduate degree from the University of Saskatchewan, I agree that the Libraries of this University may make it freely available for inspection. I further agree that permission for copying of this thesis in any manner, in whole or in part, for scholarly purposes may be granted by the professor or professors who supervised my thesis work or, in their absence, by the Head of the Department or the Dean of the College in which my thesis work was done. It is understood that any copying or publication or use of this thesis or parts thereof for financial gain shall not be allowed without my written permission. It is also understood that due recognition shall be given to me and to the University of Saskatchewan in any scholarly use which may be made of any material in my thesis.

Requests for permission to copy or to make other use of material in this thesis in whole or part should be addressed to:

Head of the Department of Chemical and Biological Engineering

University of Saskatchewan

1C01 Engineering Building

57 Campus Drive, Saskatoon, Saskatchewan (S7N 5A9)

ABSTRACT

Alumina supported manganese oxides were used in the gas phase oxidation of toluene by ozone. Catalyst activity and characterization, the promotional effect of noble metals (Pt and Pd) on the activity of manganese oxides, and the kinetics and mechanism of the reaction were investigated in this PhD thesis. It was shown that MnO_2 and Mn_2O_3 were the active sites of the catalyst capable of oxidizing toluene to CO and CO_2 below 100 ^oC. Catalysts were deactivated at room temperature due to the accumulation of carbonaceous species on their surface. At least 65 ^oC was required for the stable operation of the catalysts. X-ray absorption spectroscopy was used to study the structure and electronic properties of the mono metallic and bimetallic catalysts. It was found that the catalysts with higher Mn loading resulted in higher oxidation states of Mn which were less favorable for the oxidation of toluene. The addition of Pt to the Mn containing catalyst increased the reaction rate by transferring electrons from Pt to Mn. On the other hand, no promotional effect was observed by the addition of Pd to Mn. The Oxidation state of Mn atoms was one of the most important parameters, controlling the rate of toluene oxidation. Lower oxidation states of Mn were able to easily transfer electrons to ozone, accelerating the rate of toluene oxidation. A reaction mechanism was proposed for the catalytic oxidation of toluene over manganese oxides. In this mechanism, the oxidation of toluene was carried out by the abstraction of hydrogen atoms followed by the oxidation of toluene carbon skeleton. A rate equation was derived based on this mechanism, determining the reaction orders of -1 and 2 for toluene and ozone, respectively. It was concluded that catalytic ozonation is an effective method for the low temperature oxidation of volatile organic compounds (VOCs) in air. The significance of this method is related to energy saving in air purifying systems by reducing the required temperature to oxidize VOCs. Catalytic ozonation can be used in indoor and outdoor applications for removal of VOCs from enclosed environments or polluted industrial streams.

ACKNOWLEDGMENTS

My first acknowledgment goes to my supervisor, Dr Jafar Soltan, for his continuous supervision throughout my PhD program. His understanding of the pace of the research and having patience to overcome the difficulties are greatly appreciated. It would not be possible to complete this PhD thesis without the efforts of Dr Soltan to provide funding for this work. I also appreciate his endless support to help me to grow as an instructor by teaching an undergraduate course in the Department of Chemical & Biological Engineering, University of Saskatchewan.

I would like to thank the members of my advisory committee, Dr Mehdi Nemati, Dr Catherine Niu, Dr Hui Wang, and Dr Lee Wilson for their valuable feedback on my progress during the last four years. Their comments and suggestions greatly helped me to improve the quality of this thesis.

I am also grateful to the technical staff of the Chemical & Biological Engineering Department especially Richard Blondin, Dragan Cekic, and Heli Eunike for helping me with the purchasing of laboratory supplies and equipment and developing analytical methods.

The next appreciation belongs to Dr Ning Chen who is in charge of HXMA beamline at Canadian Light Source (CLS). He kindly collaborated with our laboratory in order to run and analyze the EXAFS of catalysts.

University of Saskatchewan, NSERC, and MITACS should also be acknowledged for providing funding for this research project.

I would like to express my gratitude to Pooyan Zahedi, Hesam Yunesi, and Babak Roshani who have been my good friends in Saskatoon. I am also thankful to Janice Tracey who has helped me to become familiar and to absorb Canadian values and culture while staying in Saskatoon.

My last acknowledgement is for my mother, Azam Talebian, my father, Gholam Rezaei, and my sister, Parisa Rezaei, who have supported and encouraged me to pursue my PhD overseas in Canada. Their emotional and financial supports have been the greatest help for me while living far away from home.

TABLE OF CONTENTS

page

LIST OF TABLES

Table page

LIST OF FIGURES

Figure page

NOMENCLATURE

BE	biding energy (eV)
BET	Brunauer–Emmett–Teller
CLS	Canadian Light Source
CN	coordination number
d_p	particle size (μm)
E	activation energy (kJ mol^{-1})
EPA	Environmental Protection Agency
EXAFS	extended X-ray absorption fine structure
ΔE_o	difference between theory and data in EXAFS energy scale (eV)
F_c	F value in Fisher's F-test
$F_{tol.}$	toluene molar flow rate ($mol_{tol.}$ s^{-1})
FT-IR	Fourier transform infra red
GC	gas chromatograph
HVAC	heating, ventilating and air conditioning
ΔH	enthalpy of adsorption (kJ mol^{-1})
IAQ	indoor air quality
ICP-MS	inductively coupled plasma mass spectrometry
k	kinetic rate constant (atm^{-1}, $mol_{tol.}$ $kg_{cat.}^{-1}$ s^{-1} atm^{-2}, $mol_{tol.}$ $kg_{cat.}^{-1}$ s^{-1} atm^{-1})
k_o	pre-exponential factor of kinetic rate constant (atm^{-1}, $mol_{tol.}$ $kg_{cat.}^{-1}$ s^{-1} atm^{-2}, $mol_{tol.}$ $kg_{cat.}^{-1}$ s^{-1} atm^{-1})
K	equilibrium constant
$K_{tol.}$	toluene pressure equilibrium constant (atm^{-1})

LH	Langmuir-Hinshelwood
Mn1	first Mn site in Mn_2O_3 structure
Mn2	second Mn site in Mn_2O_3 structure
MnO_x	manganese oxides
MS	mass spectrometer
NTP	non-thermal plasma
p	number of fitting parameter
P	pressure (atm)
PCO	photo-catalytic oxidation
PDF	powder diffraction file
r	reaction rate ($mol_{tol.}\ kg_{cat}^{-1}\ s^{-1}$)
R_f	absolute misfit between theory and data in EXAFS fitting
R_{ij}	interatomic distance between cation i and anion j (Å)
ΔR	change in the bond length between atoms (Å)
S	reaction selectivity
SBS	sick building syndrome
S_o^2	amplitude reduction factor (-)
S_{ij}	valence of the bond between cation i and anion j (-)
ΔS	entropy of adsorption ($J\ mol^{-1}\ K^{-1}$)
T	temperature (^oC or K)
TIC	total ion chromatograph
TPR	temperature programmed reduction
UV	ultra violet

VOCs	volatile organic compounds
V_i	formal oxidation state of cation i
WHO	World Health Organization
$W_{cat.}$	catalyst weight (kg)
$X_{tol.}$	toluene conversion ($mol_{tol.}\ mol_{tol.,in}^{-1}$)
XANES	X-ray absorption near edge structure
XAS	X-ray absorption spectroscopy
XPS	X-ray photoelectron spectroscopy
XRD	X-ray diffraction

Greek letters

θ	fraction of occupied or vacant catalyst active sites
ν	theoretical stoichiometric coefficient
σ^2	mean-square displacement of the bond length ($Å^2$)
χ_ν^2	reduced chi-square

Subscripts

cal.	calculated
cat.	catalyst
eff.	effective
exp.	experimental
in	inlet
O	oxygen

ozo.	ozone
tol.	toluene

Superscripts

app.	apparent
o	standard state of gases
*	catalyst active site

CHAPTER 1
INTRODUCTION

1.1. Research background and motivation

There has been an increasing concern over air pollution control in recent years due to public and environmental health and safety issues. People are now dealing with the problem of air pollution more than in the past because of living in metropolitans and spending more time indoors. Outdoor air pollutants such as gaseous molecules (organic and inorganic) and particulate matters (suspended liquid or solid fine particles) can cause damage to people and the environment [1, 2]. There have been several reports on the effect of air pollutants on humans' health. "Headache, dizziness, nausea, eye and skin irritations, respiratory system damages, lung and heart diseases, neurological effects, and cancer" are among the short and long term consequences of air pollution on people [1, 2].

The issue of air pollution is not limited to outdoor air. People inside enclosed environments such as residential buildings and work offices are exposed to air pollution problems. Sick building syndrome (SBS) is believed to be responsible for the development of diseases and allergies as the result of long term exposure of people to air pollutants inside buildings [3]. World Health Organization (WHO) has indicated that SBS can be identified in almost 30% of new houses. 6 million people of the population of Canada and half a million of people working in offices in Canada suffer from SBS [4]. Asbestos, CO, formaldehyde, NO_x, SO_2, radon, and volatile organic compounds (VOCs) are the most frequently detected pollutants in indoor air [5]. WHO statistics show that human deaths as the result of indoor air pollution in large cities are 14 times higher than those caused by outdoor air pollution. The annual death rate related to indoor air pollution is about 2.8 million which is equal to 5.5% of the total deaths

occurring around the world each year [3]. WHO has considered the smoke emitted from burning solid fuels as one of the major risk factors for human health inside buildings [6].These are all showing the importance of indoor air quality (IAQ) control which is the main motivation for the current research work.

VOCs are one of the most commonly found pollutants in indoor air. The concentration of indoor VOCs can be reduced by increasing the exchange rate of make-up air in heating, ventilating and air conditioning (HVAC) systems. However, homes nowadays have lower ventilation rates compared to the past because of the energy saving in HVAC systems, causing the accumulation of VOCs inside buildings [7]. The issue of energy saving is more serious in countries such as Canada with cold weather in most seasons of a year.

Several technologies have been developed for the removal of indoor VOCs to assist reducing energy consumption of HVAC systems. Sorption filtration, photo-catalytic oxidation (PCO), biological treatment systems, ozonation, non-thermal plasma (NTP), and combustion reactors are among the methods used for removal of indoor air VOCs [8-12]. Sorption filtration seems to be the most efficient method for the removal of VOCs from indoor air [10]. However, pollutants are not eliminated by adsorption. They are only transferred from a gas phase to a solid phase, making frequent regeneration of adsorbents necessary. Combustion of VOCs can also be considered to remove VOCs from air. In spite of the effectiveness of this method, combustion processes have poor energy efficiency. Performance of combustion chambers can be enhanced by using heterogeneous catalysts. It has been shown that VOCs such as benzene, toluene and xylene can be completely oxidized at around 200 ^{o}C using appropriate catalysts [13-16].

More decrease in the oxidation temperature of VOCs can be achieved if one replaces oxygen with ozone and uses appropriate catalysts. Transition metal oxides are effective catalysts

for ozonation of VOCs. Considering the high price of noble metal catalysts used for the oxidation of VOCs by oxygen, transition metal oxides have an economic advantage over noble metals due to their substantially lower cost of synthesis.

Catalytic ozonation has been explored for the oxidation of pollutants in liquid or gas phase over the past decades [17]. Application of this method in the gas phase has opened a new catalytic approach to low temperature oxidation of VOCs at trace concentration levels. Ethanol, carbon monoxide, acetone, cyclohexane, benzene, chlorobenzene, toluene, and formaldehyde are among the pollutants which have been oxidized by ozone over various catalysts [18-27]. The results show that the apparent activation energy of the oxidation of VOCs can be greatly reduced by ozone in comparison to that of oxygen, reducing the temperature of total oxidation of VOCs to less than 100 ^{o}C.

Manganese oxides (MnO_x) are among the most active transition metal oxides for low temperature decomposition of ozone to active oxygen species necessary for the oxidation of VOCs [28]. It is believed that the exceptional catalytic activity of MnO_x is related to the capability of these oxides to have different oxidation states during a catalytic cycle, making them the most effective catalyst for the oxidation of VOCs by ozone [29].

Therefore, based on the needs for the development of novel air purifying systems, this dissertation is focusing on the oxidation of VOCs by catalytic ozonation at low temperatures. Toluene has been chosen as the model compound for this work since it has been frequently reported as one of indoor air pollutants. The catalyst of interest is manganese oxides (Mn_2O_3 and MnO_2) supported on γ-alumina because of the high activity of manganese oxides in the oxidation of VOCs by ozone.

1.2. Structure of the thesis

The framework of this thesis has been set to elucidate existing knowledge gaps in catalytic oxidation of toluene by ozone. The general performance of toluene oxidation by ozone, the catalyst activity of different manganese loadings, the effect of the addition of promoters to manganese oxides and the kinetics and mechanism of the reaction are among the topics investigated in this work. Technology development and field applications of the current method are not within the scope of this thesis which can be explored in the future works. It has to be noted that the outcomes of this work are not limited to indoor air and they can be extended to the removal of VOCs from outdoor air as well. A literature review on indoor air quality control and the oxidation of VOCs by catalytic ozonation is given in Chapter 2. Experimental details will be explained in Chapter 3 while the general performance of the catalytic oxidation of toluene is presented in Chapter 4. Chapter 5 contains the characterization and activities of different loadings of manganese oxides dispersed on alumina. The promotional effect of noble metals on manganese oxides will be presented in Chapter 6. The kinetics and mechanism of the reaction will be discussed in Chapter 7. An overall conclusion along with the recommendations for the future works are given in Chapter 8.

It has to be mentioned that the major content of this dissertation is already published in 4 peer reviewed journal articles which are quoted in this thesis. The articles are as follows:

1. Ebrahim Rezaei and Jafar Soltan, "EXAFS and kinetic study of MnO_x/γ-alumina in gas phase catalytic oxidation of toluene by ozone", Applied Catalysis B: Environmental, 148-149 (2014), 70-79.

2. Ebrahim Rezaei, Jafar Soltan, Ning Chen, "Catalytic ozonation of toluene by ozone over alumina supported manganese oxides: effect of catalyst loading", Applied Catalysis B: Environmental, 136-137 (2013), 239-247.

3. Ebrahim Rezaei, Jafar Soltan, Ning Chen, Jinru Lin, "Effect of noble metals on activity of MnO_x/γ-alumina catalyst in catalytic ozonation of toluene", Chemical Engineering Journal, 214 (2013), 219-228.

4. Ebrahim Rezaei and Jafar Soltan, "Low temperature oxidation of toluene by ozone over MnO_x/γ-alumina and MnO_x/MCM-41 catalysts", Chemical Engineering Journal, 198-199 (2012), 482-490.

The publisher of the papers is Elsevier which allows using the published papers in the dissertation, provided that the publisher is acknowledged. Therefore, by acknowledging the publisher in this section, no further citing will be made to the above mentioned papers throughout the rest of this thesis.

The author of this thesis, Ebrahim Rezaei Geshnizgani, was the major contributor of the above published papers. Literature review, ordering and purchasing the experimental supplies and equipment, design and construction of the experimental set-up, development of the analytical methods for GC-MS, planning and conducting the experiments, interpretation of the results, and writing and revising the manuscripts were done by Ebrahim Rezaei Geshnizgani. Dr Jafar Soltan was in charge of the supervision of the thesis, providing feedback on the manuscripts, and handling the submission process of the papers. Dr Ning Chen and Jinru Lin were included in the third paper for collecting the EXAFS data of the bimetallic catalysts in Chapter 6. Dr Ning Chen was also included in the second paper because of his technical assistance to Ebrahim Rezaei Geshnizgani throughout running the samples in HXMA beamline at CLS. This data was included in Chapter 5 on the study of atomic structure and the oxidation state of different loadings of MnO_x/γ-alumina. Analysis of all the characterization techniques such as XRD, BET, H_2-TPR, FT-IR, laser Raman spectroscopy, CHNS, and X-ray absorption spectroscopy were performed by Ebrahim Rezaei Geshnizgani.

CHAPTER 2
LITERATURE REVIEW

This chapter presents a review on indoor air quality (IAQ) and the currently available methods for the removal of VOCs from indoor air. It provides a brief introduction about air cleaner systems along with their advantages and disadvantages. It continues with a detail literature survey on the catalytic oxidation of VOCs by ozone in order to outline the current progress made in this area. By summarizing the work reported by different research groups, the knowledge gaps are identified and the research objectives are established.

2.1. Indoor air quality (IAQ)

It has been reported that the ancient humans were the first people affected by SBS due to exposure to the smoke from fire in caves [30]. It was in the middle of 1950s that outdoor and indoor air pollutants were clearly identified and measured [4]. However, the initial concern was only on CO_2, odors, micro-organisms and dust as indoor air pollutants [4]. It was accepted in the mid 1960s that several health problems and diseases of people inside buildings are related to indoor air pollution [4]. Since then, there has been the establishment of several acts and protocols to reduce the concentration of indoor air pollutants [7]. Some of the major steps in addressing indoor air quality are "clean air act (1963), establishment of US EPA (1970), ban of asbestos for structural insulation (1973), limiting the lead content of residential paints (1978), report of National Research Council (NRC) on indoor air pollutants (1981), restricting the maximum emission level of formaldehyde plywood used in homes by Department of Housing and Urban Development (HUD) (1985), establishment of indoor air quality office by EPA (1985), identification of high radon content areas by EPA (1988), smoking restriction in workplace in

California (1994), and issuing rules to limit the emission of VOCs from consumer products and architectural coatings by EPA (1998)".

It can be seen that the presence of several contaminants have been restricted by different organizations over the past decades. Indoor air pollutants can be generally categorized as followings [5]:

- "Inorganic contaminants such as asbestos, radon, lead, CO, SO_2, NO_x.
- Organic contaminants such as VOCs.
- Biological contaminants such as viruses, bacteria, and mold."

VOCs are one of the most commonly found pollutants inside enclosed environments. VOCs are molecules with boiling points between 50 and 260 ^oC [9]. They contain "aliphatic, cyclic hydrocarbons, aromatic hydrocarbons, aldehydes, terpenes, alcohols, esters, halocarbons, ketones, alkanes, organic acids, and ethers" [9]. WHO has identified 320 VOCs, in which 261 and 61 of them can be found in outdoor and indoor environments, respectively [4, 31]. Most of the indoor VOCs come from sources inside buildings. Some examples are chemicals used in building materials, furniture, cleaning agents, electronic appliances, and equipment [7]. High concentrations of many VOCs may result in neurological disorders [32]. They are also responsible for irritation of eyes, skin and lungs. In addition, they can cause "headache, drowsiness, fatigue, and confusion" [32]. Some VOCs such as benzene are also suspect to have carcinogenic effects. Among different VOCs, acetaldehyde, benzene, toluene, tetrachloroethylene, and trichloroethylene have been identified as some of the major pollutants by WHO, EPA, and French indoor air quality observatory (OQAI) [11]. The presence of VOCs in indoor air has made it necessary to develop new technologies for purifications of air in

enclosed environments. The next section provides a brief overview on different methods used to purify indoor air from VOCs.

2.2. Removal of VOCs from indoor air

There are five major methods for the removal of indoor VOCs. They are sorption filtration, photo-catalytic oxidation (PCO), non-thermal plasma (NTP), and ozonation. A summary on the principle and performance of these methods is provided below.

2.2.1. Sorption filtration

Gaseous VOCs can be effectively captured on the surface of adsorbents. Excellent adsorbents usually have high surface area within their porous structure. "Activated carbon (AC), zeolites, activated alumina, porous clay minerals, silica gel, and other molecular sieves" are among the commonly used adsorbents [5]. However, AC is often used for indoor air purification. The surface area of activated carbon is around 1000 m^2/g. Only a few grams of AC can adsorb most of the indoor air pollutants. One gram of activated carbon can adsorb around 1.0, 0.7, and 0.4 grams of 1,2-dibromomethane, carbon tetrachloride, and 1,1-dimethyl hydrazine, respectively [5]. AC is also an efficient adsorbent under humid conditions since it has a non-polar surface, resulting in the adsorption of hydrocarbons rather than water vapor [5].

The main problem with the sorption filtration is that adsorbents become deactivated over time and they frequently need to be regenerated. Another deficiency of adsorbents is that they cannot remove light molecules such as formaldehyde and acetaldehyde. An active catalyst can be impregnated on the surface of adsorbents in order to increase the removal efficiency of the

adsorption process by oxidizing light hydrocarbons. Nevertheless, it can be said that the most efficient method for the removal of indoor VOCs is adsorption [10].

2.2.2. Photo-catalytic oxidation (PCO)

Photo-catalytic oxidation (PCO) works under the principles of excitation of a semiconductor under ultra violet (UV) light. An electron can be ejected from the valence band of a semiconductor when it absorbs the energy of UV light, provided that UV light provides enough energy for the excitation of the electron [10]. This phenomenon creates a hole in the valence band. The holes and excited electrons are considered as active species in converting water vapor molecules to hydroxyl radicals, oxidizing organic pollutants [33]. PCO activity depends on the presence of water vapor and the activity of PCO reactors decreases in the absence of humidity. On the other hand, high concentrations of water vapor suppress the PCO reaction due to the adsorption of water molecules on PCO catalysts. In addition, it has been reported that there is an optimum point for inlet concentration of pollutants, giving the maximum oxidation rate of VOCs [8, 33].

PCO catalysts consist of semiconductors such as oxides of titanium, tin, zinc, iron, manganese, and tungsten [8]. TiO_2 is one of the most effective photo-catalysts in the oxidation of VOCs under UV light. Performance of PCO is related to several factors such as water vapor concentration, the source of UV light, and the inlet concentration of pollutants. Different types of PCO reactors also have different removal efficiencies, making the design of the reactors to be one of the major tasks in PCO based processes [33]. TiO_2 catalysts doped with transition metals have also shown to be capable of operating under visible light to oxidize VOCs, replacing UV light with natural sources such as sunlight [33].

PCO is a safe air cleaner at ambient conditions. It is effective for removal of different types of VOCs because of the high oxidation potential of OH radicals. However, there are a few drawbacks attributed to PCO. The first problem is related to the partial oxidation of VOCs and production of harmful by-products [33]. Photo-catalysts might also become deactivated by the accumulation of reaction by-products [33]. The energy efficiency of PCO is also low [10, 33]. TiO_2 has a polar structure which is not suitable for the removal of non-polar compounds. Overall, the mentioned limitations have restricted the widespread application of PCO [10, 11, 33].

2.2.3. Non-thermal plasma (NTP)

Highly energetic electrons are generated in atmospheric plasma in a way that the air matrix remains at room temperature. Gas phase molecules (nitrogen, oxygen, and water vapor) can be ionized with the produced electrons, generating reactive species such as atomic oxygen, hydroxyl radicals, and ozone [34]. These species are highly reactive and are able to oxidize organic pollutants. However, harmful by-products such as ozone, CO, and NO_x are generated by NTP with low CO_2 selectivity of 0.3-0.7 [8, 35-37]. NTP reactors do not work steadily and their energy consumption is high [8, 35, 37].

In order to enhance the degradation efficiency and the energy consumption of non-thermal plasma reactors, it is possible to couple NTP with heterogeneous catalysts. Two different configurations can be used in order to incorporate catalysts in NTP [35]. The first option is to put catalysts inside the plasma region in a configuration called in plasma catalyst (IPC). The second choice is to utilize catalysts after the NTP reactors called post plasma catalyst (PPC) configuration.

ICP allows production of new active species such as peroxide or hydroxyl radicals, oxidizing VOCs on the surface of the catalysts. On the other hand, if catalysts are used after NTP (PPC), it is possible to use the generated ozone inside NTP to further oxidize undesired reaction by-products.

Manganese oxides dispersed on alumina was used as a PPC reactor, resulting in total oxidation of benzene, toluene and xylene to CO_2 [37]. A semiconductor such as TiO_2 can also be incorporated inside NTP reactors, combining non-thermal plasma and photo-catalytic oxidation techniques. This approach was used in the oxidation of toluene using TiO_2 as IPC and Pd, Cu, and Mn containing catalysts as PPC [34, 38]. Even though the combination of NTP and PCO has proven to be effective, it has been observed that the degradation of VOCs decreases by increasing the relative humidity of the inlet gas stream.

In general, the sole NTP method is not an effective technique for the removal of VOCs due to high energy consumption and low CO_2 selectivity, producing harmful by-products. The addition of catalysts inside or after the plasma region can increase the efficiency of the NTP method, but further investigations are needed before it is introduced into the market as a commercial product.

2.2.4. Ozone generators

Gaseous ozone can be considered as a potential oxidant for the removal of odor and VOCs from indoor air. Ozone generators have been used widely worldwide. Although it has been shown that ozone can be used for the elimination of odor, it reacts very slowly with organic pollutants in the gas phase. The half life of homogeneous reaction of ozone with VOCs such as formaldehyde, cyclohexane, toluene, and xylene ranges from 0.9 to 4400 years [39]. Formaldehyde is one of the most refractory molecules to react with ozone (half life of 4400

years) and toluene is one of the reactive species toward ozone with half life of 0.9 year. Due to the low reaction rate of ozone with VOCs, it is necessary to use high concentrations of ozone to completely oxidize organic compounds.

An ozone generator was used to study the performance of gaseous ozone in the removal of phenycyclohexene, styrene, and 4-ethynylcyclohexene [39]. These VOCs were emitted from a carpet located in an experimental chamber. Even though ozone was effective to reduce the concentration of these compounds, several harmful by-products such as formaldehyde and organic acids were also generated. As a conclusion, it can be said that the use of ozone generators as indoor air cleaners is not recommended due to the low reaction rate and the production of harmful by-products [5, 10, 39].

In an extended study, the performance of the above-mentioned methods except NTP, was tested using different indoor air cleaners, including sorption filtration, photo-catalytic oxidation and ozone generators [10]. The air cleaners were tested on several model compounds consisting of alkanes, aromatics, chlorocarbons, aldehydes, ketones, and alcohols. In comparison of different methods, it was concluded that sorption methods were efficient except for the removal of light hydrocarbons such as formaldehyde, acetaldehyde, and dichloromethane. PCO showed promising results in eliminating formaldehyde and acetaldehyde. The most important deficiencies of PCO were related to the high energy consumption and the efficient design of PCO reactors. It was suggested that further studies were needed to design high performance PCO air cleaners [10]. Authors did not recommend use of ozone generators for indoor air purifications [10].

2.3. Review on catalysts used for oxidation of VOCs by ozone

As mentioned in section 2.2, currently, there is not a single promising method for the elimination of VOCs from indoor air except the sorption filtration. It seems that further studies are needed on PCO and NTP methods before they can be commercialized for indoor air applications. The homogeneous reaction of ozone and VOCs is also slow and does not lead to the mineralization of organic pollutants. These limitations have encouraged researchers to study alternative approaches such as catalytic ozonation for indoor air quality control. Transition metal oxides such as (Fe, Co, Cu, Mn, Ni, and Cr) have been used for the oxidation of various VOCs by ozone. The results show that depending on the reaction condition and the type of catalysts used, VOCs can be oxidized in the temperature range of 22-100 ^{o}C. The low temperature activity of catalytic ozonation makes this method suitable for indoor air treatment applications. This section describes the recent literature of catalytic oxidation of VOCs by ozone which helps to determine the knowledge gaps that exist in this research area.

Ozone is a reactive gas which was first discovered in 1839. But it was later in 1865 that the molecular structure of ozone was determined [17]. Ozone consists of three oxygen atoms forming an angle of 116^{o}49’ between terminal atoms. The molecule represents four resonance structures shown in Fig. 2.1. The high reactivity of ozone is attributed to the electron configurations of the molecule. Lack or excess of electrons in different resonance forms of ozone determines the electrophilic or nucleophilic characteristics of ozone, respectively [40]. These properties make ozone highly reactive and also thermodynamically unstable leading to the decomposition of the molecule to oxygen by the reaction of $2O_3 \rightarrow 3O_2$.

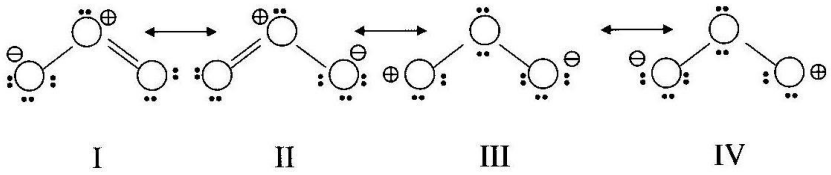

Fig. 2.1. Resonance structures of ozone; courtesy of CRC Press LLC [40].

Ozone has an oxidation potential of 2.07 eV which is only less than fluorine, atomic oxygen, OH radical, and a few other oxidants [17]. Some other properties of ozone are given in Table 2.1 [17, 40].

Table 2.1. Properties of ozone [17, 40]

Properties	Value
Standard heat of formation (ΔH^{o}_{298})	-142 kJ mol^{-1}
Standard free energy of formation (ΔG^{o}_{298})	-163 kJ mol^{-1}
Standard entropy (S^{o}_{298})	239 J K^{-1} mol^{-1}
Melting point	-251 ^{o}C
Boiling point	-112 ^{o}C

There are three main research groups worked systematically on different aspects of the catalytic ozonation in the past two decades. The first group belongs to Naydenov and Mehandjiev and co-workers which started working on the oxidation of benzene and CO over transition metal oxides since 90s [19, 41-45]. MnO_2, $NiMnO_3$, $NiMn_2O_4$, NiO_x/alumina, CoO_x/alumina, Cu-Cr/alumina, and Co-Cr/alumina are among the transition metal oxides

investigated by them. Their results show that transition metal oxides are appropriate catalysts for low temperature decomposition of ozone and oxidation of benzene [41]. They have also indicated that the activation energy of benzene oxidation is greatly reduced by using ozone instead of oxygen. It was reported that the application of ozone could reduce the oxidation temperature of benzene from 150-200°C to 20-80°C [43]. It has been suggested that the formation of atomic oxygen on the surface of the catalyst as the result of ozone decomposition is responsible for the oxidation of benzene. Alumina supported Cu-Cr and Co-Cr oxides were studied in the oxidation of benzene and CO using oxygen or ozone [44]. Ozone greatly decreased the reaction temperature in the presence of Co-Cr/Alumina catalyst. Complete oxidation of benzene was achieved at around 100 °C by ozone.

The second research group in this field is Oyama and co-workers [18, 20, 28, 29, 46-51]. They also started their work in 90s, focusing on ethanol oxidation and the mechanism of ozone decomposition reaction. One of their first conclusions was that manganese oxides were the most active transition metal oxides in the decomposition of ozone. Oxides of Mn, Co, Ni, Cr, Ag, Cu, Ce, Fe, V, and Mo were selected by Dhandapani and Oyama for ozone decomposition on γ-alumina [28]. MnO_2 was the most active metal oxide in the decomposition of ozone followed by Co_3O_4, NiO, Fe_2O_3, and Ag_2O. Conductivity measurement showed that p-type metal oxides such as manganese oxide were more favorable in ozone decomposition comparing to n-type transition metal oxides. Li and Oyama investigated the kinetics and mechanism of catalytic ozone decomposition by *in-situ* laser Raman spectroscopy, *Ab Initio* calculations, and isotope exchange techniques [47, 48]. They have proposed that the decomposition of ozone can be described by the following elementary steps:

$$O_3 + * \rightarrow O* + O_2 \qquad (2.1)$$

$$O_3 + O^* \rightarrow O_2^* + O_2 \quad (2.2)$$

$$O_2^* \rightarrow O_2 + * \quad (2.3)$$

In which * denotes catalyst active sites which are Mn atoms. Ozone is adsorbed dissociatively on the catalyst surface in step (2.1) to form a surface atomic oxygen (O*) and a gas phase oxygen molecule. The atomic oxygen reacts with the second ozone molecule in step (2.2) to form a surface peroxide (O_2*) and another oxygen molecule. The surface peroxide desorbs in step (2.3) to free the active site. Kinetic studies showed that the surface of the catalysts had a non-uniform nature. The activation energy of step (2.1) was determined to be less than the activation energy of step (2.3), showing that the desorption of ozone is controlling the rate of ozone decomposition.

Oyama and co-workers also worked on the total oxidation of acetone by ozone over silica supported manganese oxides [20, 29, 51]. They focused mainly on the characterization of the catalyst active sites by X-ray absorption spectroscopy, the effect of Mn loading on the catalyst activity, and the kinetics and mechanism of the reaction. They showed that the activation energy of acetone oxidation was reduced by ozone, leading to conversion of acetone to CO_2 below 100 ^oC [20]. Their results indicated that higher Mn loadings had better catalytic activity. It was mentioned that lower oxidation state of Mn atoms in higher Mn loadings was more favorable in the decomposition of ozone, accelerating the rate of acetone oxidation [29]. They also concluded that the reaction between acetone and ozone was structural sensitive, facilitated on larger manganese oxide clusters. They mentioned that the oxidation reaction needed adjacent Mn atoms to accommodate several atomic oxygen species required for the total oxidation of acetone [29]. Oyama and co-workers also performed fundamental studies on the kinetics and mechanism of acetone oxidation by ozone using *in-situ* laser Raman spectroscopy [51]. They proposed a

Langmuir-Hinshelwood (L-H) mechanism with the following elementary steps to explain the mechanism of acetone oxidation:

$$O_3 + * \rightarrow O* + O_2 \quad (2.4)$$

$$O_3 + O* \rightarrow O_2* + O_2 \quad (2.5)$$

$$O_2* \rightarrow O_2 + * \quad (2.6)$$

$$A + \square \leftrightarrow A\square \quad (2.7)$$

$$A\square + * \rightarrow A* + \square \quad (2.8)$$

$$A* + O* \rightarrow \text{products} \quad (2.9)$$

, □ and A represent Mn active sites, SiO_2 (support), and acetone, respectively. Steps (2.4) to (2.6) refer to the decomposition of ozone on Mn sites while step (2.7) shows quasi equilibrated adsorption of acetone on the support (SiO_2). Adsorbed acetone molecules migrate from the silica support to Mn active sites, shown by step (2.8). Surface acetone molecules are activated by reacting with atomic oxygen in step (2.9). It was assumed that further steps after step (2.9) are fast and are not important from kinetic point of view. Peroxide species (O_2) were spectators in the mechanism and they were not involved in the oxidation of acetone. Authors derived rate equations for acetone oxidation and ozone decomposition based on the mechanism explained by steps (2.4) to (2.9).

The third research group which has been working on catalytic ozonation of VOCs is led by Einaga and co-workers [21, 22, 52-59]. Einaga and Futamura investigated the performance of alumina-supported metal oxides (Mn, Fe, Co, Ni, Cu, and Ag) for the oxidation of benzene and cyclohexane by ozone at room temperature [21, 52, 53]. Mn showed the highest activity for benzene oxidation at room temperature by converting benzene to CO and CO_2. However, none of the metals showed stable activity in benzene oxidation. MnO_x/alumina lost its activity within 2

hours, due to the accumulation of reaction intermediates on the surface of the catalyst at room temperature. Weakly bound compounds including formic acid, 2,5-furandione and phenol, and strongly bound species such as formate and carboxylates were found on the catalyst surface as the result of incomplete oxidation of benzene at room temperature [53]. Einaga and Futamura showed that catalyst deactivation at room temperature can be suppressed by introducing water vapor to the gas matrix, inhibiting the accumulation of reaction by-products on the catalyst [60]. Positive effect of water vapor was also observed in the oxidation of formaldehyde by ozone over synthetic MnO_x catalysts [61]. It was observed that formaldehyde can be completely oxidized to CO_2 under humid condition at room temperature.

Different ion-exchanged zeolites including Mn-Y, Mn-β, Mn-MOR, and Mn-ZSM5 were employed by Einaga and Futamura to oxidize benzene by ozone at 70 ^oC [54]. Mn-Y had the highest activity among all the catalysts with CO and CO_2 as the main reaction products. No catalyst deactivation was observed at 70 ^oC, resulting in 80% benzene conversion using Mn-Y catalyst. CO and CO_2 selectivity were 18 and 82%, respectively. The effect of different supports (Al_2O_3, TiO_2, ZrO_2, and SiO_2) in the oxidation of benzene by manganese oxides was studied by Einaga and Ogata [56]. The results show that catalysts with higher surface area and consequently more dispersed Mn atoms result in higher rates of benzene oxidation. SiO_2 with the highest surface area had the highest activity by converting benzene to CO and CO_2 at 100 °C. 60 ^oC was needed to attain steady state activity of the catalysts. Einaga et al. also studied the effect of Mn loading on the oxidation rate of benzene by ozone [55]. In contrast to the result of Oyama et al. reported for acetone oxidation, Einaga et al. concluded that lower loadings of Mn are more favorable for the oxidation of benzene.

Einaga et al. have reported that manganese oxides impregnated on ultra stable Y (USY) zeolites with high silica to alumina ratio (Mn/USY, SiO_2/Al_2O_3=180) is able to steadily oxidize benzene to CO and CO_2 at 22 and 40 ^oC under humid and dry conditions, respectively [22, 58]. It has been mentioned that high Mn dispersion and hydrophobicity of USY might be responsible for the exceptional activity of Mn/USY. In one of their recent publications, Einaga et al. have studied unsupported perovskite catalysts ($LaMnO_3$ and $La_{0.8}Sr_{0.2}MnO_3$) in the oxidation of benzene by ozone [59]. They have also investigated the effect of addition of Fe, Co, Ni, and Cu to Mn in order to enhance the activity of unsupported manganese oxide catalysts. The results show that monometallic Mn catalysts have higher activity than the perovskite catalysts. It was indicated that bimetallic catalysts have lower activity than monometallic manganese oxides, even though Mn-Co catalysts improved the selectivity of the reaction to CO_2.

There are also works published by other research groups, focusing on model compounds other than acetone, formaldehyde, cyclohexane, and benzene which were discussed above. CO, naphthalene, chlorobenzene, and toluene have also been oxidized by ozone over various catalysts [23-25, 62-71].The results indicate that catalytic ozonation is an effective method for the oxidation of a wide variety of VOCs. Nevertheless, catalytic oxidation of toluene by ozone has received more attention among the mentioned VOCs. Chao et al. have studied the oxidation of toluene by ozone using zeolite 13X at room temperature [66]. 90% toluene conversion was observed at room temperature but the catalyst did not show stable activity because of the adsorption of CO_2, water, and reaction by-products. Zeolites NaX, NaY, and MCM-41 were chosen by Kwong et al. for toluene removal by ozone [67]. The results indicated that MCM-41 had the best performance for the ozonation of toluene at room temperature. No water and carbon dioxide were detected at the reactor outlet. This showed that reaction by-products were

accumulated on the catalyst surface, deactivating the catalyst. Sugasawa and Ogata investigated the performance of transition metals (Fe, Ni, Ag, Co, and Mn) supported on ZSM-5 in catalytic oxidation of toluene at 100 ^{o}C. Mn showed superior catalytic activity in the oxidation of benzene. They also mentioned that even though Ag was not as active as Mn, it had higher selectivity toward CO_2 among the transition metals tested [69]. This is in agreement with Einaga and Ogata, reporting higher CO_x selectivity of Ag supported catalysts in benzene oxidation [57]. Catalytic ozonation of toluene was also studied by Park et al. using Mn supported on TiO_2 ultrafine nano composites [70]. Their results showed that this catalyst was also effective in the oxidation of toluene with the highest conversion of toluene to CO and CO_2 at 100 ^{o}C. Li et al. investigated the effect of modification of MCM-41 zeolites by Cu and Co on catalytic oxidation of toluene [25]. Catalysts were prepared by two different methods. In the first method, Cu and Co were loaded on MCM-41 by the conventional impregnation technique. In the second method, Cu and Co were incorporated into the structure of MCM-41by *in-situ* synthesis of MCM-41with the metals. The Co containing catalyst prepared by the *in-situ* formation of MCM-41 showed higher and more stable activity compared to the other catalysts for low temperature oxidation of toluene. Authors mentioned that high dispersion of Co atoms might be responsible for high activity of the Co incorporated MCM-41 catalyst.

In summary, it can be said that catalytic oxidation of VOCs by ozone is an effective method for low temperature oxidation of air pollutants. CO, benzene, acetone, formaldehyde, naphthalene, chlorobenzene, cyclohexane, and toluene are among the air contaminants removed by ozone. The operating temperature of catalytic ozonation process ranges from 22 to 100 ^{o}C, depending on the type of the catalyst, nature of the pollutant, and reaction conditions. Catalysts mostly consist of supported or unsupported transition metal oxides such as Mn, Cu, Co, Ag, and

Ni. This gives an extra advantage to catalytic ozonation processes since it removes the need for the synthesis of catalysts based on noble metals which are more expensive than transition metal oxides. Mn is the most active transition metal oxide for the decomposition of ozone and the oxidation of VOCs. The high activity of Mn is attributed to the electronic configuration of this metal oxide, allowing Mn atoms to exist at different oxidation states during the catalytic cycle of VOCs oxidation. Major reaction by-products of VOCs oxidation are CO and CO_2. Catalyst deactivation has been reported in case of aromatic compounds such as benzene and toluene at room temperature. Heating the catalyst bed to 60-70 ^oC increases the activity of the catalysts and results in steady state oxidation of aromatics. Water vapor has a positive effect on the activity of the catalysts at room temperature, preventing the deactivation of catalysts. The mechanism of the oxidation of VOCs by ozone follows a heterogeneous phenomenon. Ozone is decomposed to surface oxygen atoms which are responsible for the oxidation of adsorbed VOCs. The reaction mechanism can be described by steps (2.4) to (2.9) in which, adsorbed VOC molecules react with adsorbed oxygen atoms to start the oxidation reaction.

There are also technologies developed based on catalytic oxidation by ozone [17]. Toto, Inc. (Japan) has designed units for odor removal in toilets and refrigerators working by ozone and different types of catalysts. Hitachi (Japan) also has developed a catalytic ozonation unit called Dashpure^{TM} for odor removal, disinfection, and oxidation of VOCs. UCAIR^{TM} is the name of the technology developed by Union Carbide for the removal of VOCs, CO, and aerosol microbes from indoor air at ambient pressure and temperature. Nevertheless, there are not many reports on the commercial applications of catalytic ozonation, showing the need for more research on this method.

2.4. Knowledge gaps and objectives

Even though details of the reaction of ozone with VOCs such as acetone and benzene have been investigated widely, there are not many reports on catalytic oxidation of other aromatic compounds such as toluene or xylenes. Toluene has been frequently reported as one of the VOCs in indoor air. Therefore, toluene is considered as the model compound in the present study. Chapter 4 of this thesis elucidates different aspects of the catalytic oxidation of toluene by ozone over manganese oxides. The oxidation behavior of toluene at room and higher temperatures up to 100 ^{o}C is presented in this chapter. Characterization of the catalyst active sites, identification of the reaction by-products, and carbon balance of the reactor is discussed in Chapter 4 as well.

As mentioned in section 2.3, nano-particles of manganese oxides are mostly used in the oxidation of VOCs by ozone [26, 29, 55]. Less attention has been paid to the characterization of manganese oxides by novel techniques such as X-ray absorption spectroscopy including X-ray absorption near edge structure (XANES) and especially extended X-ray absorption fine structure (EXAFS). This is mainly due to the complicated unit cell structure of Mn_3O_4 and Mn_2O_3 with two Mn sites and several sets of oxygen atoms, closely located around the Mn sites. There are also controversial reports on the effect of Mn loading and catalyst structure on the activity of supported MnO_x in the oxidation of VOCs [29, 55]. It is a matter of question whether higher or lower loadings of Mn benefit oxidation of VOCs by ozone. Therefore, Chapter 5 discusses activities of different loading of manganese oxides dispersed on alumina in the oxidation of toluene by ozone. This chapter clarifies the relationship among the structure of manganese oxides, the oxidation states of Mn atoms, and the observed catalytic activities. XANES and EXAFS are used as the main characterization techniques in Chapter 5 to justify the activity of the catalysts.

Investigation of the promotional effect of noble metals on the activity of manganese oxides is another area which has not been explored in the oxidation of VOCs by ozone. There are reports showing that the combination of transition metal oxides and noble metals such as Pt and Pd can enhance the activity of catalysts in the combustion of VOCs by oxygen [72-74]. The majority of researchers have only focused on the ozonation of VOCs over transition metal oxides. Thus, Chapter 6 of this thesis is dedicated to study the effect of addition of Pt and Pd to Mn in order to enhance the activity of supported manganese oxides in the oxidation of toluene by ozone. Atomic interactions between noble metals (Pt and Pd) and manganese oxides are studied using XANES and EXAFS. EXAFS helps to probe the atomic environment around Mn, Pt, and Pd in monometallic and bimetallic catalysts. XANES is also useful to track changes in the oxidation states of Mn, Pt, and Pd in order to explain the promotional effect of noble metals on manganese oxides.

Another issue which is not still completely clear is the mechanism of catalytic ozonation of aromatic molecules and relevant kinetic steps involved in the mechanism. It is believed that the oxidation reaction occurs between adsorbed atomic oxygen and VOC molecules according to Langmuir-Hinshelwood type of mechanism [51]. Even though this mechanism has been applied to explain the kinetics of acetone oxidation by ozone, there has not been any report to explore other possible reaction mechanisms which might better explain the oxidation of aromatic molecules such as toluene. Thus, Chapter 7 investigates the possible elementary steps involved in the catalytic oxidation of toluene by ozone over alumina supported manganese oxides. This is carried out by analysis of the effect of toluene and ozone partial pressures on the initial reaction rates and testing the applicability of the available reaction mechanisms reported in the literature

to the catalytic ozonation of toluene. Possible alternative elementary steps will also be proposed which can better describe the observed kinetic data of toluene oxidation by ozone.

CHAPTER 3
EXPERIMENTAL

This chapter presents details of the experiments performed on catalytic ozonation of toluene by manganese oxides. Experimental set-up, analytical methods, and catalyst preparation are introduced first followed by activity tests and catalyst characterization techniques. The characterization methods includes Brunauer–Emmett–Teller (BET), inductively coupled plasma mass spectrometry (ICP-MS), X-ray diffraction (XRD), laser Raman spectroscopy, hydrogen temperature programmed reduction (H_2-TPR), X-ray absorption near edge structure (XANES), and extended X-ray absorption fine structure (EXAFS). Deactivated catalysts are studied by Fourier transform infra red (FT-IR) spectroscopy and CHNS analysis.

3.1. Experimental set-up and analysis

The schematic diagram of the experimental set-up is shown in Fig. 3.1. Toluene is supplied from a mixture of toluene in nitrogen cylinder (Praxair) with concentration of 300 ppm of toluene and balance of nitrogen (accuracy of ±2%). Oxygen (Praxair, ultra high purity grade, 99.993%) flows to an ozone generator (AZCO Industries LTD, HTU-500S) to produce ozone. Two mass flow controllers (Brooks, SLA 5850) are used to adjust flow rates of toluene-nitrogen and oxygen streams at desired set points. Accuracy of the mass flow controllers are ±1% of the reading flow rate. Total flow rate entering the reactor is 1000 ml min^{-1}.

The ozone and toluene streams are combined to produce toluene and ozone concentration of 90-240 and 1050-3000 ppm, respectively. In a typical experiment, 400 ml min^{-1} of toluene/nitrogen stream is mixed with 600 ml min^{-1} of ozone/oxygen stream to yield 1050 and 120 ppm of ozone and toluene, respectively. This combination results in nitrogen and oxygen

mole fractions of 39.94% and 59.94%, respectively. The reactor operating at ambient pressure is made of a horizontal Pyrex tube (i.d. 1/2 inch). The reactor is installed inside an oven (Binder, FP 115) which accurately controls the reaction temperature between room temperature and 100 ^{o}C. Fluctuation in the reaction temperature is less than ± 0.3 ^{o}C during the reaction.

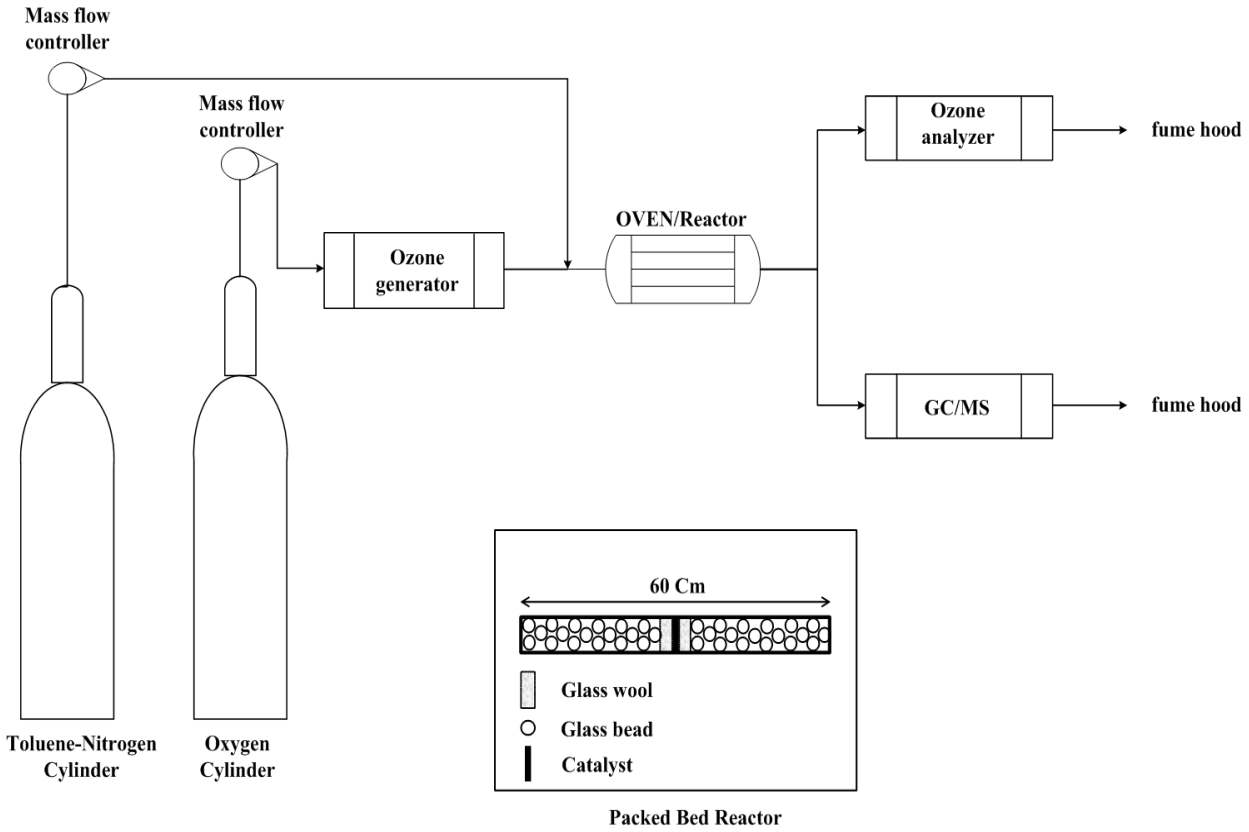

Fig. 3.1. Schematic of the experimental set-up.

Outlet stream of the reactor is passed through an ozone analyzer to measure the concentration of ozone. The ozone analyzer is an API 465M, working based on UV absorption to measure gas phase ozone concentration. The analyzer is set to measure the concentration of ozone from zero to 5000 ppm. The accuracy of the ozone analyzer is ±50 ppm.

An on-line gas chromatograph (GC) (Agilent, 7890A) coupled with a mass spectrometer (MS) (Agilent, 5975C) is employed to measure the concentration of toluene, CO, CO_2, and other reaction by-products. The MS is set to work under scan mode. A capillary column (Varian, Select Permanent Gasses/CO_2, CP7429) is utilized to measure toluene, CO, and CO_2 concentrations. This column consists of four sub-columns. The first one is a 5 meter pre-retention gap column with diameter of 0.53 mm connected to two parallel columns. The first column is a CP-PoraBond Q (length: 50 m, dia.: 0.53 mm) for the detection of CO_2 and toluene and the second column is a CP-Molsieve 5A (length: 10 m, dia.: 0.32 mm) for the detection of CO. These two columns reconnect to a 5 meter post-retention gap column with diameter of 0.25 mm. Other oxygenated by-products are identified using an Agilent standard column HP-5MS (length: 30m, dia.: 0.25mm). A standard mixture of CO, CO_2, and nitrogen is used to quantify the concentration of CO and CO_2. The concentration of CO and CO_2 in the standard gas mixture is 650 and 630 ppm, respectively. Appendix A presents the GC-MS calibration data of toluene, CO, and CO_2.

3.2. Catalyst preparation

γ-alumina (Alfa Aesar, S_{BET}=212 m^2 g^{-1}, pore volume of 0.6 cm^3 g^{-1}) is impregnated with aqueous solutions of manganese (II) nitrate tetrahydrate (Sigma-Aldrich, 97%) in order to synthesize alumina supported manganese oxides catalysts (MnO_x/γ-alumina). The catalyst preparation method is wet incipient impregnation or dry impregnation. The loading of Mn is between 1 and 20%. Mn loading is calculated based on the mass of metallic manganese per mass of the catalysts (support plus manganese oxides). For example, in order to prepare 10 g of MnO_x/γ-alumina with 10% Mn loading from the nitrate precursor, 42.3 g of manganese (II) nitrate tetrahydrate ($Mn(NO_3)_2.4H_2O$, MW=251.01) is added to 50 cm^3 of deionized water under

vigorous stirring until the precursor is dissolved. This results in a solution with $Mn(NO_3)_2.4H_2O$ concentration of 3.4 mol l^{-1}. Then 6 cm^3 of the prepared solution is taken by micropipette and added dropwise to γ-alumina which is already dispersed in a beaker. The impregnated support is dried at 100 ^oC for 10 h and calcined in the furnace under atmospheric air at 500 ^oC for 4h.

Tetraamineplatinum (II) nitrate salt (Alfa Aesar, 99.99%) and tetraaminepalladium (II) nitrate solution (Alfa Aesar, 99.9%) are used as precursors for the preparation of noble metal containing catalysts. The catalysts are labeled as Pd/γ-alumina and Pt/γ-alumina for monometallic catalysts and Pt-MnO_x/γ-alumina and Pd-MnO_x/γ-alumina for bimetallic catalysts. Pd/γ-alumina and Pt/γ-alumina are prepared by wet incipient impregnation of γ-alumina while Pt-MnO_x/γ-alumina and Pd-MnO_x/γ-alumina are synthesized by dry impregnation of the prepared MnO_x/γ-alumina catalyst. All the four catalysts are dried for 10 hours at 100 ^oC and calcined at 550 ^oC for 4 hours. Loadings of manganese and the noble metals are set at 10 % and 1 %, respectively.

In order to check the effect of particle size on the activity of the catalysts and to inhibit internal mass transfer limitations on the reaction rate, different ranges of particle size are tested for the reaction. The result of toluene conversion versus reaction time is shown in Fig. B.1 of Appendix B. It is observed that the activity of the catalyst, MnO_x/γ-alumina (10%), drops when particles larger than 208 μm are used. Thus, all experiments are conducted using catalysts with particle size less than 208 μm. The effect of external mass transfer on the reaction rate is also investigated in order to make sure that the catalytic oxidation of toluene is not controlled by the rate of external mass transfer of toluene from the gas phase. Details of the calculations are presented in Appendix C, showing that the oxidation of toluene proceeds in the absence of external mass transfer limitations.

MnO (Alfa Aesar, 99%, manganosite), MnO_2 (Alfa Aesar, 99.9%, pyrolusite), Mn_2O_3 (Sigma Aldrich, 99%, bixibyite), Mn_3O_4 (Sigma Aldrich, 97%, hausmannite), and α-PtO_2 (Alfa Aesar, 99.95%) are used as reference materials for characterization.

3.3. Catalyst activity measurements

Typically 0.2 g of fine powder catalysts is used for activity measurements. Catalysts are sandwiched between two pieces of glass wool and the empty space of the reactor is filled with glass beads in order to help mixing of the reactants before reaching the catalyst bed. The total flow rate of reactant at the inlet of the reactor is 1000 ml min^{-1}, corresponding to weight hourly space velocity (WHSV) of 300 l hr^{-1} g^{-1}. Experiments are conducted in three phases. The first phase is saturation of catalysts with toluene in the absence of ozone for almost one hour until the outlet concentration of toluene reaches the inlet value. After the saturation of the catalysts, the ozone generator is turned on and the reaction starts at room temperature. Room temperature activity of the catalyst is monitored for 150 minutes. When the catalysts become deactivated at room temperature, reactor temperature is increased to 40, 60, 80, and 100 ^oC to study the catalyst activity at higher temperatures. At each temperature, the catalyst bed is allowed to stabilize for 80 minutes. Two samples are taken and compared at each temperature step before moving forward to the higher temperatures to test whether the reactor has reached steady state operating conditions. Raw data of a typical repeated experiment is given in Appendix D. The activity of catalysts versus time is obtained in another set of experiments. These experiments also start with the saturation of the catalyst with toluene at room temperature. But catalysts are allowed to work at different temperatures for longer period of time. Catalyst activities are monitored for 6 hrs at temperature levels of 22, 40, 55, 65, 80, and 100 ^oC. These experiments are suitable to study long term activity of the catalysts and to study the deactivation behavior of the catalysts.

A homogeneous reaction contribution (maximum toluene conversion of 18%) is observed in blank runs at different temperatures inside the empty reactor. Heterogeneous catalytic activities are calculated based on the subtraction of the homogeneous reaction rate from total reaction rate. In order to incorporate ozone concentration in the homogeneous reaction, a first order reaction is assumed for calculation of the homogeneous reaction rate

3.4. Catalyst characterization

Brunauer–Emmett–Teller (BET) surface area and pore volume of the catalysts is determined by nitrogen adsorption at -196 ^{o}C using ASAP 2000 (Micromeritics). Samples are degassed at 200 ^{o}C for two hours under vacuum level of 500 μmHga. BET surface area is measured between nitrogen partial pressure ratio (P/P_{atm}) of 0.05 and 0.3. Total pore volume of the catalysts is determined by measuring the amount of nitrogen adsorbed at $P/P_{atm} = 0.95$. Loading of the catalysts is verified by inductively coupled plasma mass spectrometry (ICP-MS) on a PerkinElmer, Nexion 300D instrument. The weight percent of carbon accumulated on the catalysts is measured by CHNS analysis using Vario EL III, Elementar Americans Inc. Uncertainties of BET, ICP-MS, and CHNS analyses are presented in Appendix E.

X-ray diffraction (XRD) is performed on a Brucker diffractometer (D8 Advance) using Cu Kα in the 2θ range of 10-60^{o} with a step size of 0.04^{o}. Raman spectroscopy measurements are carried out on a Renishaw InVia Raman microscope using a 514.5 nm Ar+ laser (Spectra Physics) and a CCD detector. The instrument is operated in the line focus mode with a 10 s detector exposure time, and 32-128 spectra accumulations. Raman spectra are collected in the range of 100 to 1000 cm^{-1}. Hydrogen temperature programmed reduction (H_2-TPR) is performed with an Autosorb-iQ (Quantachrome Instruments) TPD/TPR instrument equipped with a thermal conductivity detector (TCD). Samples are dried at 100 ^{o}C for two hours before the TPR analysis.

Reduction is performed in the range of 50 to 550 ^{o}C with the temperature ramp of 10 K/min using a gas mixture of 3.1% hydrogen balanced with nitrogen. The flow rate of the feed gas is 50 ml N min^{-1}.

Fourier transform infra red (FT-IR) spectra are recorded in the range of 400 to 4000 cm^{-1} using 32 scans on a JASCO FT/IR 4100 spectrometer with DLATGS detector. The resolution of the detector is 4 cm^{-1}. Samples are diluted with potassium bromide (KBr) and pressed into disks before the analysis.

X-ray absorption near edge structure (XANES) and extended X-ray absorption fine structure (EXAFS) of catalysts are collected at HXMA beamline, Canadian Light Source (CLS) having a storage ring with 200-250 mA current at 2.9 GeV [75]. The experiments are performed in transmission mode for Mn data collection of the catalysts and the reference materials. Fluorescence mode is used for the Pt and Pd catalysts. The samples are diluted with adequate amount of boron nitride (BN), pressed to thin disks and stuck on Kapton tape in order to obtain an approximately one unit edge jump at the absorption edge. Straight ion chamber detectors are used with Si(111) monochromator crystal and Rh mirrors as collimating and focusing mirrors, respectively. The scan step-sizes are 10 eV/step, 0.25 eV/step, and 0.05 $Å^{-1}$ for the pre-edge, XANES, and EXAFS regions, respectively.

Data processing including background removal, data averaging and normalization, energy calibrations, and determination of absorption energies are performed by Athena [76]. Absorption energies are obtained based on the position of the inflection point in the rising part of the spectra. The inflection point is determined by the energy of the major first peak in the 1st derivative of the normalized absorption spectra. EXAFS fitting is performed by Artemis which is a front-end graphical interface for FEFF [77] and IFEFFIT [78]. EXAFS fitting parameters are

passive electron reduction factor (S_o^2), coordination number (CN), change in interatomic distance (ΔR), mean-square displacement of the bond length (σ^2), and change in energy scale (ΔE_o). Uncertainties in processing EXAFS data in Artemis are estimated by evaluating the root mean square value of the measured signal in the range of 15 to 25 Å assuming that no structure can be measured in this range and any signal is due to shot noise [79]. CNs are fixed based on crystallographic data in EXAFS analysis of the reference materials to obtain S_o^2 which can be used as a fixed parameter in EXAFS analysis of the catalysts. This allows obtaining oxygen and manganese CNs at the first and second shells of MnO_x clusters dispersed on γ-alumina. ΔR, ΔE_o, and σ^2 are allowed to be floating for the reference materials and the catalysts and their values are calculated by the fitting of EXAFS data.

CHAPTER 4
CATALYTIC OXIDATION OF TOLUENE BY OZONE

Chapter 4 investigates the performance of manganese oxides dispersed on γ-alumina for the oxidation of toluene by ozone. The catalyst investigated in this chapter is MnO_x/γ-alumina with manganese loading of 10%. The details of catalyst characterization, activity of the catalyst, identification of reaction by-products and reaction carbon balance are presented and discussed.

4.1. Characterization of MnO_x/γ-alumina (10%)

4.1.1. BET and ICP-MS

Manganese oxides (MnO_x) with nominal loading of 10% are impregnated on γ-alumina based on the method explained in section 3.2. The catalyst is called MnO_x/γ-alumina (10%). Table 4.1 shows the loading of Mn measured by ICP-MS. BET surface area and pore volume of γ-alumina and MnO_x/γ-alumina (10%) are also presented in Table 4.1. It can be seen that the pore volume and BET surface area of γ-alumina decrease after the impregnation of manganese oxides due to the partial pore plugging by MnO_x clusters. However, the prepared catalyst still shows high surface area (S_{BET}=177 m^2 g^{-1}) and pore volume (0.51 cm^3 g^{-1}), indicating that the porous structure of γ-alumina is preserved during the preparation procedure. The measured concentration of manganese by ICP-MS shows that the actual loading of Mn is close to the nominal value which is 10% by weight.

Table 4.1. BET surface area, pore volume, and metal loading of the catalyst

	γ-alumina	MnO_x/γ-alumina (10%)
BET surface area (m^2 g^{-1})	212	177
Pore volume (cm^3 g^{-1})	0.60	0.51
Mn Loading wt%	-	9.5

4.1.2. X-ray diffraction (XRD)

Fig. 4.1 shows the powder diffraction files (PDF) of manganese oxides (MnO, MnO_2, Mn_2O_3, and Mn_3O_4) [80] while Fig. 4.2 indicates the XRD spectra of the reference materials. The most intense peaks of MnO (manganosite) are located at 2θ of 34.9, 40.4, and 58.8 degrees as shown in Fig. 4.1 (A). PDF of Pyrolusite MnO_2 is shown in Fig. 4.1 (B) with the most intense peaks at 28.7, 37.3, 42.8, and 56.7 degrees. Mn_2O_3 (bixbyite) has the major diffraction peaks at 23.1, 32.9, 38.2, 49.3, and 55.2 degrees as it can be seen in Fig 4.1 (C). PDF of Mn_3O_4 (hausmannite) is shown in Fig. 4.1 (D) with the major peaks at 18.0, 28.9, 32.3, 36.1, and 59.9 degrees. One can identify the phases of the reference materials, shown in Fig. 4.2, by matching the diffraction pattern of the reference materials to the powder diffraction files presented in Fig. 4.1. Based on peak-matching, it can be concluded that MnO, MnO_2, Mn_2O_3, and Mn_3O_4 reference materials are manganosite, pyrolusite, bixbyite, and hausmannite phases of manganese oxides.

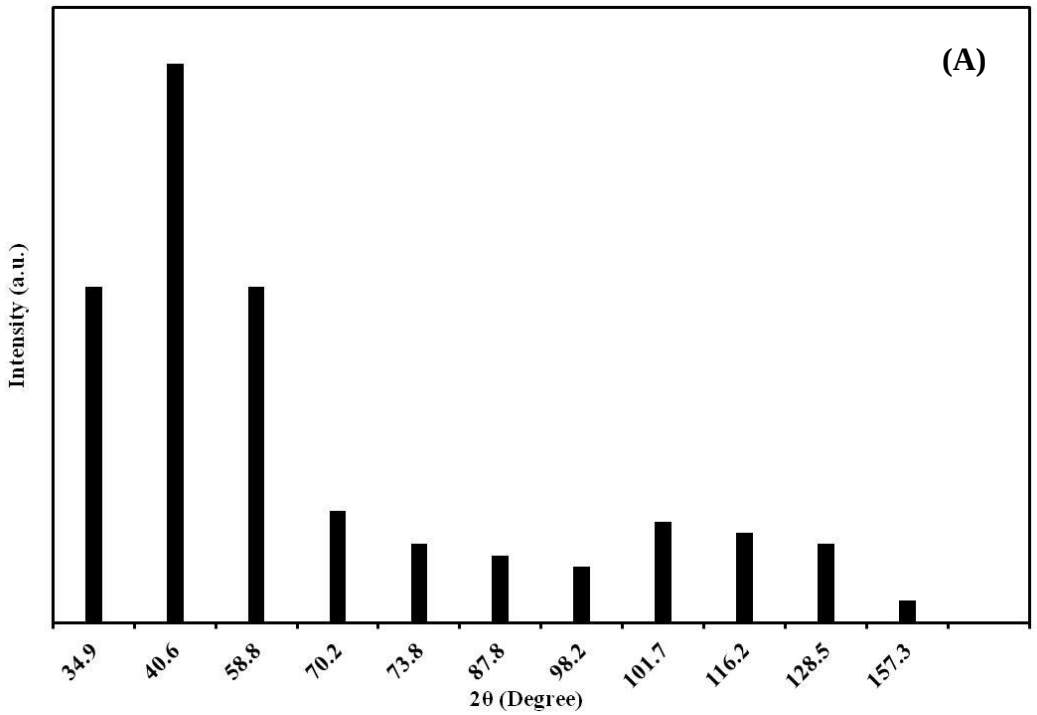
(A)
Intensity (a.u.)
34.9
40.6
58.8
70.2
73.8
87.8
98.2
101.7
116.2
128.5
157.3
2θ (Degree)

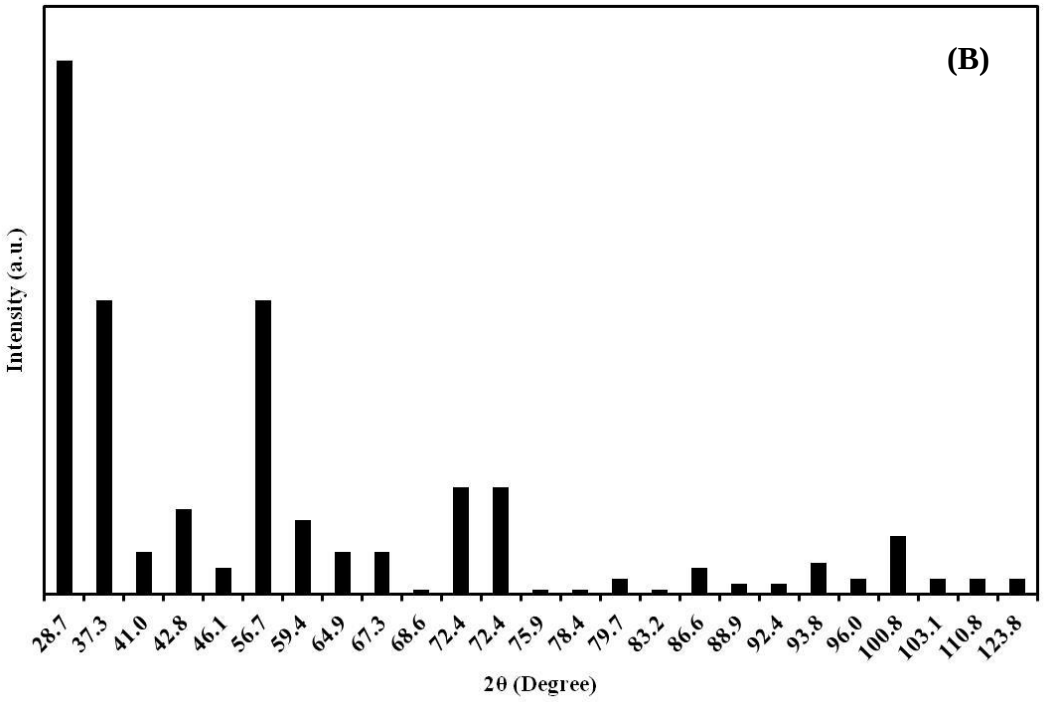
(B)
Intensity (a.u.)
28.7
37.3
41.0
42.8
46.1
56.7
59.4
64.9
67.3
68.6
72.4
72.4
75.9
78.4
79.7
83.2
86.6
88.9
92.4
93.8
96.0
100.8
103.1
110.8
123.8
2θ (Degree)

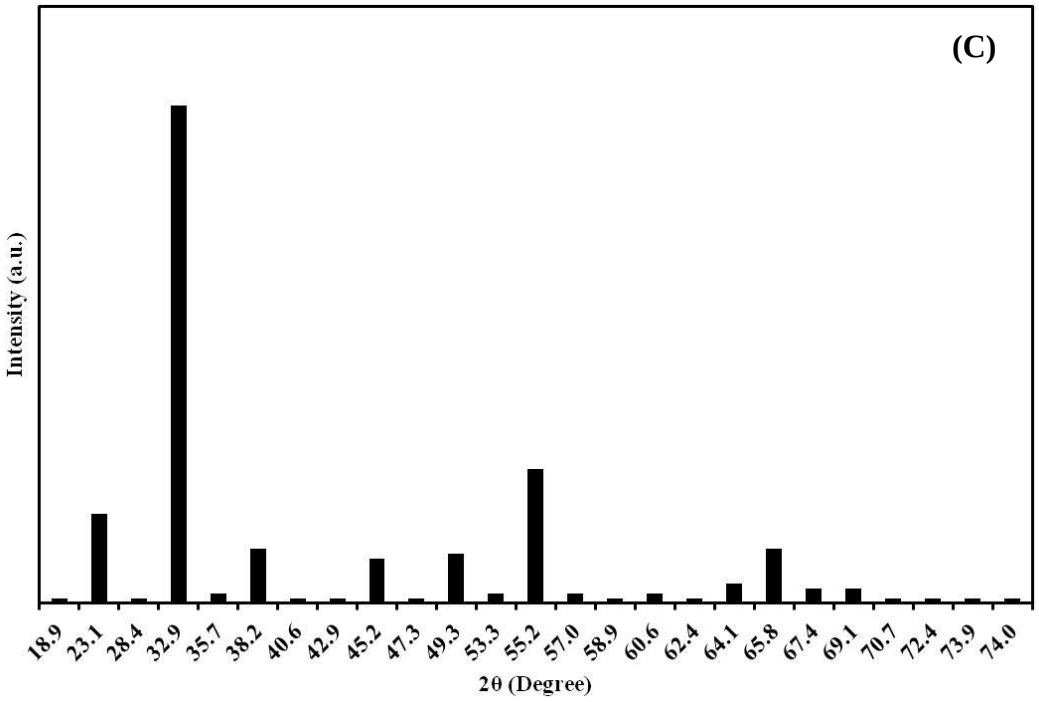

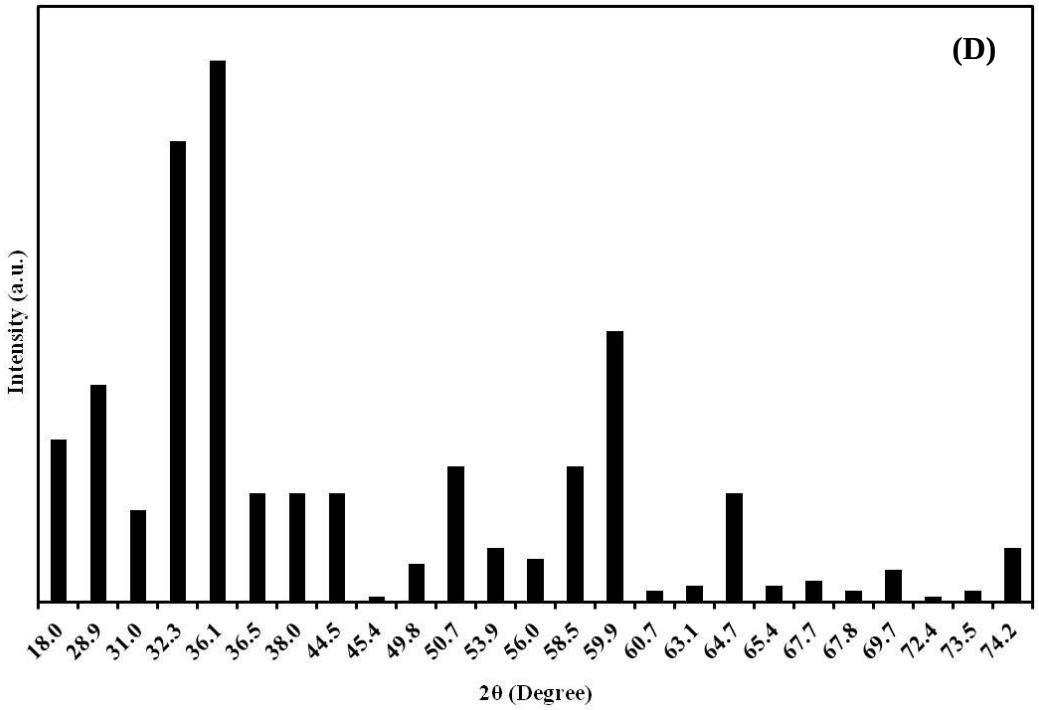

Fig. 4.1. Powder diffraction file (PDF) of reference materials, (A) MnO: manganosite, (B) MnO_2: pyrolusite, (C) Mn_2O_3: bixbyite, and (D) Mn_3O_4: hausmannite.

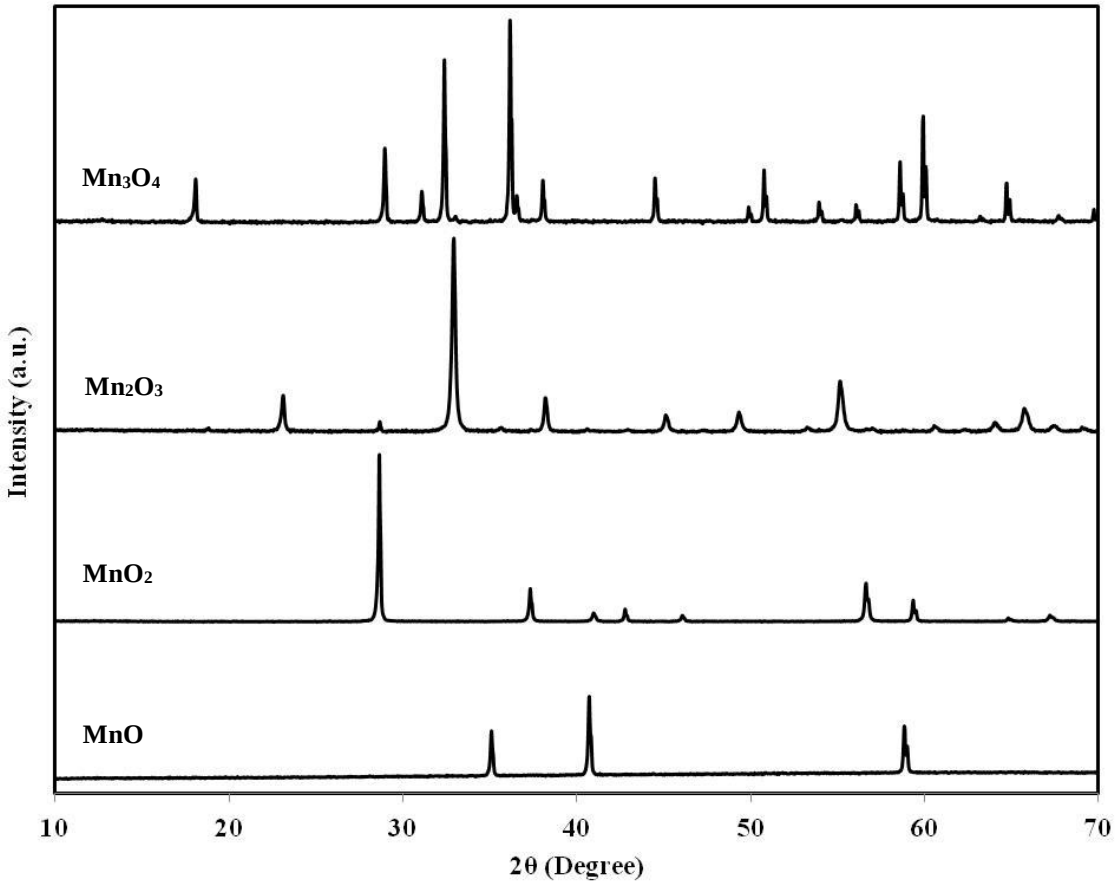

Fig. 4.2. XRD spectra of the reference materials.

The XRD of MnO_x/γ-alumina (10%) is shown in Fig. 4.3, indicating the formation of MnO_2 and Mn_2O_3 phases on γ-alumina. MnO_2 (pyrolusite) is identified with the most intense peaks at 28.7, 37.3, 42.8, and 56.7 degrees. In addition, Mn_2O_3 (bixibyite) has distinct peaks at 23.1, 32.9, 38.2, 49.3, and 55.2 degrees. Therefore, it can be concluded that MnO_2 (pyrolusite) and Mn_2O_3 (bixbyite) are formed on γ-alumina with Mn loading of 10%. Average particle sizes of MnO_2 and Mn_2O_3 on γ-alumina can be estimated by applying Scherrer's equation [81]:

$$t = \frac{K\lambda}{\beta\cos\theta} \tag{4.1}$$

In which, t is the thickness of the particle in nm, λ is the X-ray wavelength (0.154 nm), β is the peak width at half maximum in radians, K is a constant (0.9), and θ is the angle between the beam and the normal on the reflecting lattice plane in radians. For particle size analysis, the most intense XRD peaks of MnO_2 (28.7 degree) and Mn_2O_3 (32.9 degree) are selected. It is estimated by Eq. 4.1 that MnO_2 and Mn_2O_3 have average metal cluster size of 17 and 23 nm on γ-alumina, respectively.

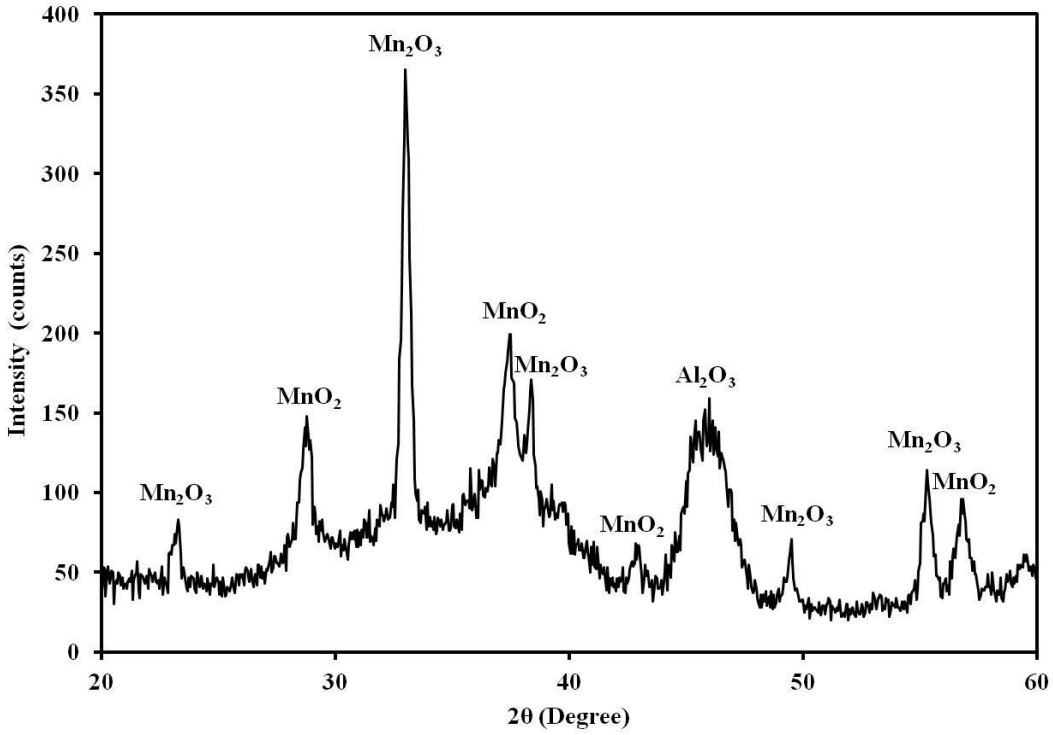

Fig. 4.3. XRD of the MnO_x/γ-alumina (10%).

Table 4.2 contains the unit cell dimensions of MnO_2 (pyrolusite) and Mn_2O_3 (bixbyite) crystals along with the calculated dispersion of MnO_2 and Mn_2O_3 based on the particle sizes obtained from XRD [82]. It is determined that there are 8 and 20 atoms of Mn on the external

surface of the unit cell structure of MnO_2 and Mn_2O_3, respectively. This results in surface Mn atom density of 1.80×10^{19} and 7.53×10^{18} atom m^{-2} for MnO_2 and Mn_2O_3, respectively. Therefore, a 17 nm cubic cluster of MnO_2 will have approximately 31130 Mn surface atoms. Similarly, a 23 nm cubic particle of Mn_2O_3 roughly contains 23910 surface Mn atoms. If one considers the density of MnO_2 and Mn_2O_3, reported in Table 4.2, and the number of Mn surface atoms in MnO_2 and Mn_2O_3 clusters, dispersion of MnO_2 and Mn_2O_3 can be estimated to be 6.1 and 3.8%, respectively.

Table 4.2. Mn dispersion in MnO_x/γ-alumina (10%)

	Lattice constants (nm)	Density ($cm^3\ g^{-1}$)	Dispersion (%)
MnO_2 (pyrolusite)	a=b=0.4396 c= 0.2871	5.03	6.1
Mn_2O_3 (bixibyite)	a=b=c= 0.9408	4.50	3.8

4.1.3. Laser Raman spectroscopy

Raman spectra of the reference materials (MnO, MnO_2, Mn_2O_3, and Mn_3O_4), γ-alumina, and MnO_x/γ-alumina (10%) are depicted in Fig. 4.4. Mn_3O_4 is the most Raman sensitive phase of manganese oxides with a strong peak at 658 cm^{-1}. There are also two other peaks at 318 and 372 cm^{-1} in the spectra of Mn_3O_4. These peaks have also been reported by Buciuman and coworkers as fingerprints of Mn_3O_4 [83] . MnO is the second Raman active phase of manganese. Raman spectra of MnO show two peaks at 552 and 652 cm^{-1} which is in agreement with MnO Raman spectra reported by Kapteijn et al. [84]. MnO_2 and Mn_2O_3 are less Raman active oxides of manganese with small signal to noise ratios. MnO_2 generates two peaks at 531 and 662 cm^{-1}. Buciuman et al. have observed three peaks at 510, 580, and 640 cm^{-1} for MnO_2 [83] whereas,

Kapteijn et al. did not identify any peaks in Raman spectra of this oxide [84]. In another work, Ferrandon et al. have obtained a signal at 532 cm^{-1} [85] which is the same as MnO_2 peak at 531 cm^{-1} reported in our work. Mn_2O_3 has four peaks at 198, 311, 644, and 699 cm^{-1}, respectively. Peak locations of Mn_2O_3 are in agreement with the work of Kapteijn et al. except the one at 198 cm^{-1} which cannot be observed in their results [84]. The reason that they have not detected this peak might be due to the fact that they collected the spectra from 200 to 1200 cm^{-1}, leading to the absence of the peak at 198 cm^{-1}.

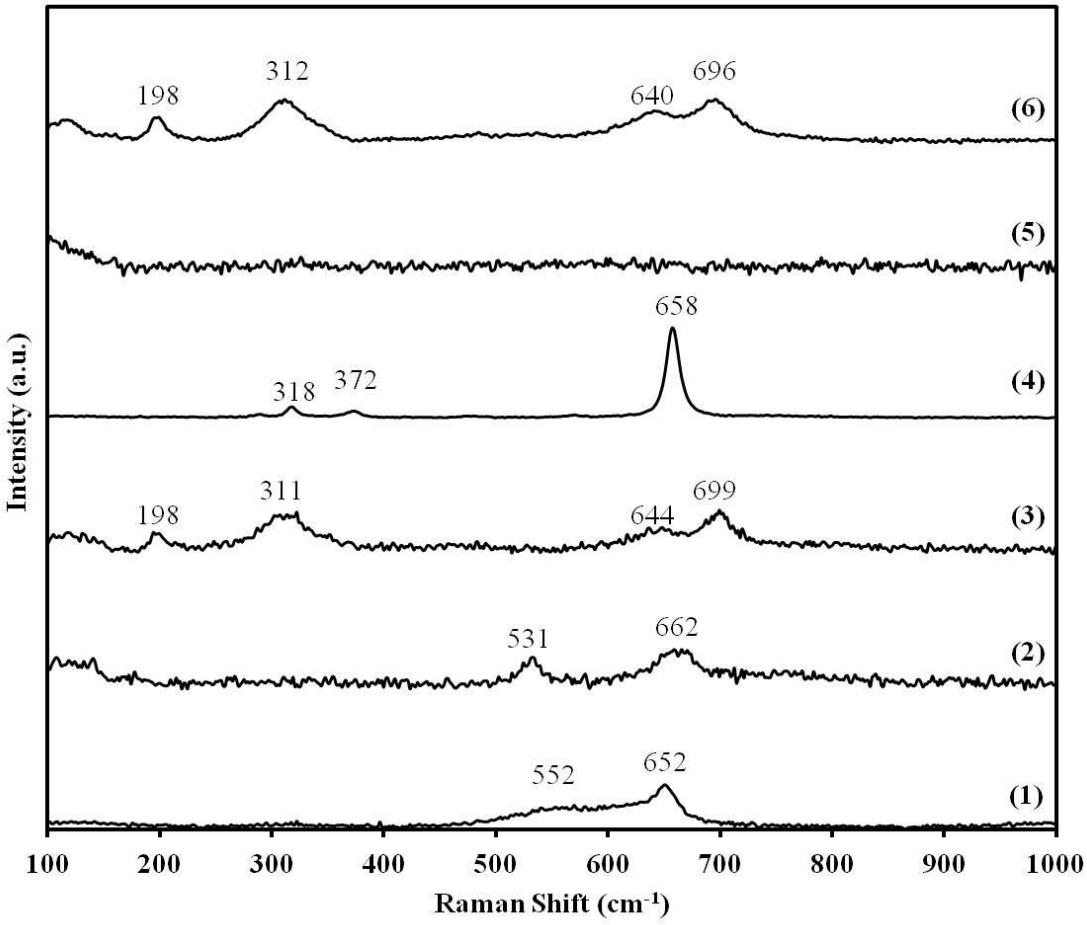

Fig. 4.4. Raman spectra of the samples, (1) MnO, (2) MnO_2, (3) Mn_2O_3, (4) Mn_3O_4, (5) γ-alumina, and (6) MnO_x/γ-alumina (10%).

As emphasized by Buciuman et al., there is a high potential for the formation of Mn_3O_4 during data collection of Raman spectra due to the local heating of samples [83]. Therefore, peaks at 311 and 644 cm^{-1} might be assigned to *in-situ* formation of Mn_3O_4 during the analysis of Mn_2O_3 sample. The same point also applies to MnO_2, suggesting that the peak at 662 cm^{-1} should not be mistaken as characteristic of MnO_2. Thus we consider the peak at 531 cm^{-1} for the identification of MnO_2 and two peaks at 198 and 699 cm^{-1} as characteristic of Mn_2O_3.

Raman spectra of γ-alumina and MnO_x/γ-alumina (10%) are also shown in Fig. 4.4. γ-alumina does not show any Raman signal, showing that γ-alumina is a Raman inactive material. On the other hand, there are two distinct peaks of Mn_2O_3 at 198 and 696 cm^{-1} on the spectra of MnO_x/γ-alumina (10%), implying the presence of Mn_2O_3 in this catalyst. No MnO_2 peak is detected in MnO_x/γ-alumina (10%) which might be expected to be detected at around 531 cm^{-1}. It is noteworthy to mention that the peak at 640 cm^{-1} is due to the *in-situ* formation of Mn_3O_4 and it is not considered as an indication of Mn_3O_4 on MnO_x/γ-alumina (10%). The reason for the absence of MnO_2 Raman signal in the spectra of MnO_x/γ-alumina (10%) is likely due to the low fraction of MnO_2 in comparison to the fraction of Mn_2O_3 on the surface of the catalyst.

4.1.4. X-ray absorption near edge structure (XANES)

Fig. 4.5 contains the normalized absorption XANES spectra of Mn *K-edge* for manganese oxide reference materials and MnO_x/γ-alumina (10%). XANES spectra of manganese oxides contain a weak pre-edge feature due to the quadruple (dipole-forbidden) transition of electrons from 1s to 3d orbital. The main absorption happens due to the dipole-allowed transition of electrons from 1s to 4p orbital of Mn giving the rising part of the spectra. It can be seen that the spectra of MnO_x/γ-alumina (10%) is located between that of Mn_2O_3 and MnO_2, suggesting that

manganese has an average oxidation state between +4 and +3. Linear combination fitting (LCF) of MnO_x/γ-alumina (10%) with MnO_2 and Mn_2O_3 reference materials shows that 91.0% of Mn is in +3 and 9.0% of Mn is in +4 oxidation states.

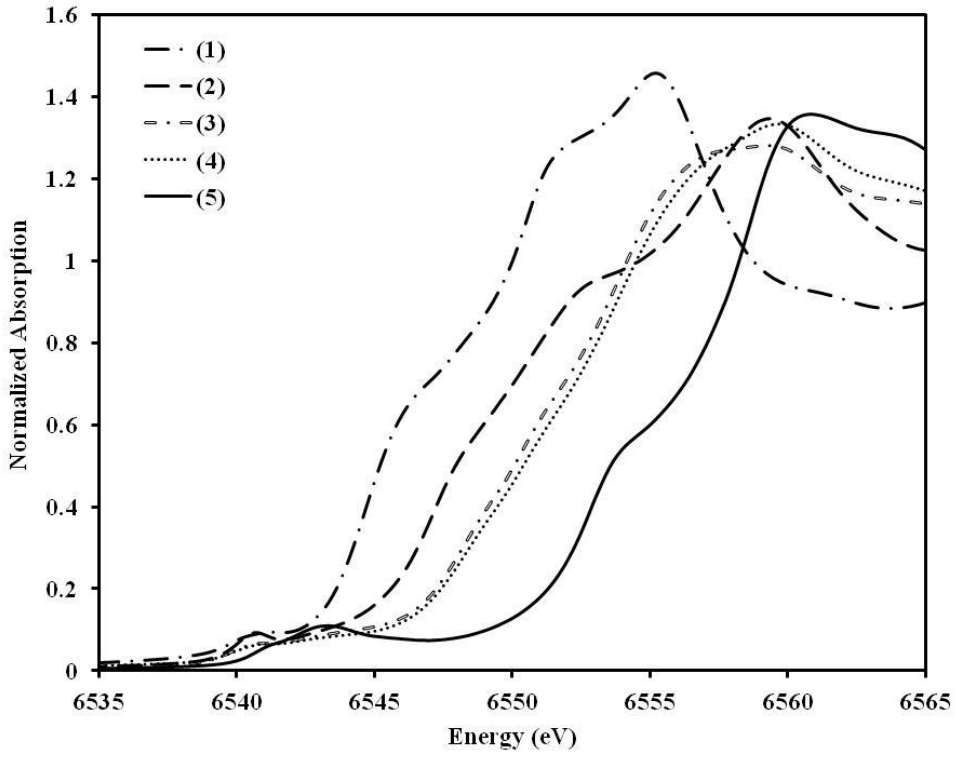

Fig. 4.5. Mn *K-edge* XANES spectra, (1) MnO, (2) Mn_3O_4, (3) Mn_2O_3, (4) MnO_x/γ-alumina (10%), and (5) MnO_2.

It can be concluded from the result of XRD, laser Raman spectroscopy, and XANES that MnO_2 and Mn_2O_3 are the two phases of manganese oxides which are generated by using the nitrate precursor of Mn for the catalyst preparation. XANES analysis reveals that Mn_2O_3 is the dominant phase of manganese oxides on MnO_x/γ-alumina (10%) with weight fraction of 91.0%.

4.2. Activity of MnO_x/γ-alumina (10%)

4.2.1. Oxidation of toluene by MnO_x/γ-alumina (10%)

Fig. 4.6 and 4.7 show the activity of MnO_x/γ-alumina (10%) in terms of toluene and ozone conversions, respectively. Concentration of ozone and toluene are 1050 and 120 ppm, respectively. The conversions are obtained at 22, 40, 55, 65, 80, and 100 ^oC for 6 hours at each temperature level using 0.2 g of MnO_x/γ-alumina (10%). The flow rate of toluene/nitrogen and ozone/oxygen streams are 400 and 600 ml min^{-1}, respectively. It can be observed in Fig. 4.6 that the catalyst shows high initial activity at all temperatures. But the activity of catalysts decreases at temperatures below 65 ^oC, implying the deactivation of the catalyst.

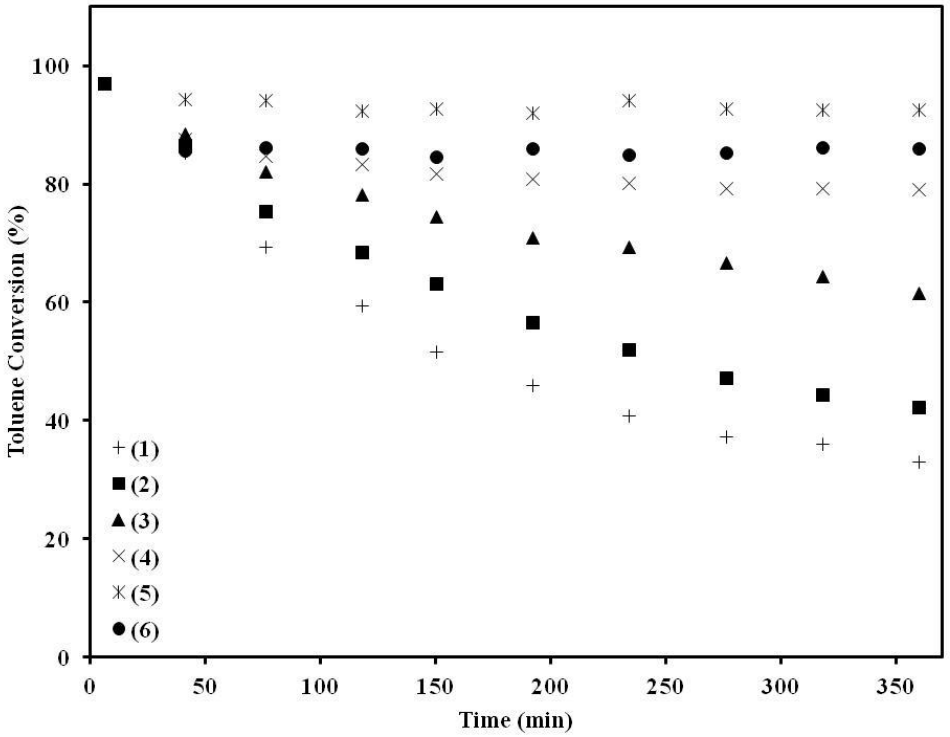

Fig. 4.6. Toluene conversion versus time over MnOx/γ-alumina (10%), (1) 22 ^oC, (2) 40 ^oC, (3) 55 ^oC, (4) 65 ^oC, (5) 80 ^oC, and (6) 100 ^oC.

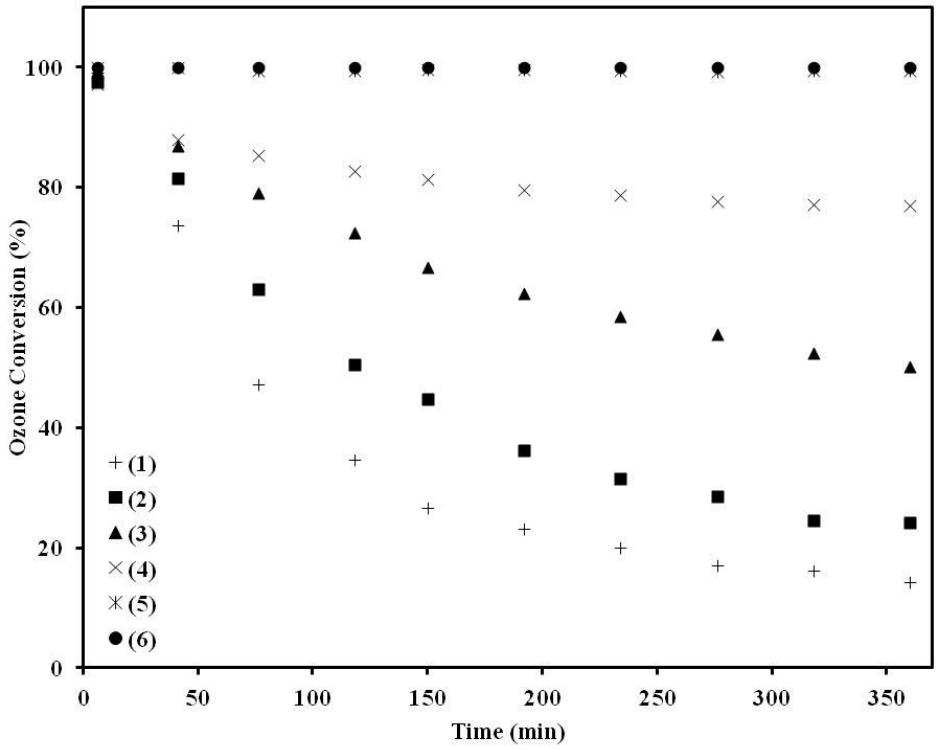

Fig. 4.7. Ozone conversion versus time over MnOx/γ-alumina (10%), (1) 22 ºC, (2) 40 ºC, (3) 55 ºC, (4) 65 ºC, (5) 80 ºC, and (6) 100 ºC.

MnO_x/γ-alumina (10%) shows stable activity in the oxidation of toluene at 65, 80, and 100 ºC after almost 150 minutes reaction. Maximum toluene conversion is around 95% which is obtained at 80 ºC. A decrease in toluene conversion can be seen by increasing the temperature from 80 to 100 ºC.

Ozone conversions at different temperatures are shown in Fig. 4.7, in which the conversions increase by increasing the temperature. No steady state ozone conversion is obtained below 65 ºC. Ozone conversion reaches 100% at 80 ºC and remains constant by increasing the temperature from 80 to 100 ºC. In fact, the 80 ºC is the temperature, at which ozone is completely consumed under the given reaction condition. Therefore, the increase of temperature from 80 to 100 ºC does not improve the ozone conversion. This can be considered as the reason

for the small decrease in toluene conversion above 80 ^{o}C, since all ozone is already decomposed at 80 ^{o}C. The same behavior has been reported in catalytic ozonation of acetone by MnO_x/γ-alumina and MnO_x/SiO_2, in which a fluctuating plateau occurs above 80 ^{o}C due to complete conversion of ozone, keeping acetone conversion more or less constant [20].

Carbon content of the deactivated catalyst, MnO_x/γ-alumina (10%), is determined by CHNS analysis. Data is obtained after the catalyst becomes deactivated at room temperature after 150 minutes. Bare support, γ-alumina, is also tested without exposure to the reaction medium to determine a baseline for the initial carbon content of the support. The fresh support contains negligible carbon (0.20%), whereas the deactivated catalyst showed 10.25% carbon content after the deactivation. Thus, it can be inferred that the accumulation of carbon containing species on the catalyst blocks active sites and reduces the catalyst activity at room temperature. Einaga and coworkers studied the deactivated alumina supported manganese oxides in the oxidation of benzene by ozone [53, 56]. They reported that two types of by-products were formed on the surface of the catalysts. The first type is weakly bonded molecules such as carboxylic acids (formic acid, acetic acid, and oxalic acid) and the second type is strongly attached species such as formate and carboxilates. Thus, it can be assumed that oxygenated by-products formed as the result of incomplete oxidation of toluene are responsible for the deactivation of the catalysts at room temperature. By increase of the reaction temperature, oxidation of these by-products is promoted and the catalyst regains its activity at temperatures higher than 65 ^{o}C.

In order to clarify the contribution of γ-alumina in the activity of MnO_x/γ-alumina (10%), 0.2 g of bare γ-alumina (not impregnated by manganese oxides) was tested for the oxidation of toluene by ozone. It was observed that γ-alumina resulted in constant conversions of 20 and 10% for toluene and ozone in the range of 20-100 ^{o}C, respectively. By comparing the low activity of

γ-alumina (not more than 20% in terms of toluene conversion) with the activity of manganese oxides impregnated γ-alumina (Fig. 4.6 and 4.7), one can conclude that the active phase of the catalyst is manganese oxides. As it was revealed in section 4.1, Mn_2O_3 is the dominant phase of manganese oxides in MnO_x/γ-alumina (10%) which can be considered as the active component of the catalyst in this work.

The oxidation mechanism of VOCs by ozone is considered to be based on the decomposition of ozone to atomic oxygen and peroxide species on manganese oxide clusters which can be expressed by the following steps [20]:

$$O_3 + * \rightarrow O_2 + O* \quad (4.2)$$

$$O_3 + O* \rightarrow O_2 + O_2* \quad (4.3)$$

$$O_2* \rightarrow O_2 + * \quad (4.4)$$

In equations 1 to 3, * corresponds to Mn sites. It is believed that the generated atomic oxygen is responsible for the oxidation of VOCs [20, 56].

In another study, the conversion of toluene is monitored over 0.2 g of MnO_x/γ-alumina (10%) in the absence of ozone. 120 ppm of toluene in nitrogen and oxygen (toluene/nitrogen flow rate of 400 ml min^{-1} and oxygen flow rate of 600 ml min^{-1}) is passed over the catalyst bed while the ozone generator is kept off. The reaction performance of toluene conversion versus temperature is shown in Fig. 4.8 (a). No toluene conversion is observed in the temperature range of 22-100 ^oC, indicating the crucial role of ozone in low temperature oxidation of toluene over the catalyst. In order to explore the applicability of this method to actual air composition, the flow rates of toluene/nitrogen and ozone/oxygen streams are changed to 800 and 200 ml/min, respectively. These flow rates set the concentration of N_2 and O_2 at 80 and 20%, respectively. This arrangement results in toluene concentration of 240 ppm. Accordingly, the power of ozone

generator is set to produce 2500 ppm ozone at the inlet of the reactor in order to have enough ozone to react with toluene. Activity of the catalyst with actual air composition (toluene/nitrogen = 800 ml min^{-1} and ozone/oxygen = 200 ml min^{-1}) is shown in Fig. 4.8 (b). Fig. 4.8 (c) shows the activity of the catalyst with 120 ppm toluene and 1050 ppm ozone obtained by mixing 400 ml $min^{-1}$of toluene/nitrogen mixture with 600 ml min^{-1} of ozone/oxygen mixture for comparison. It has to be noted that 0.2 g of MnO_x/γ-alumina is used to obtain all activities in Fig. 4.8.

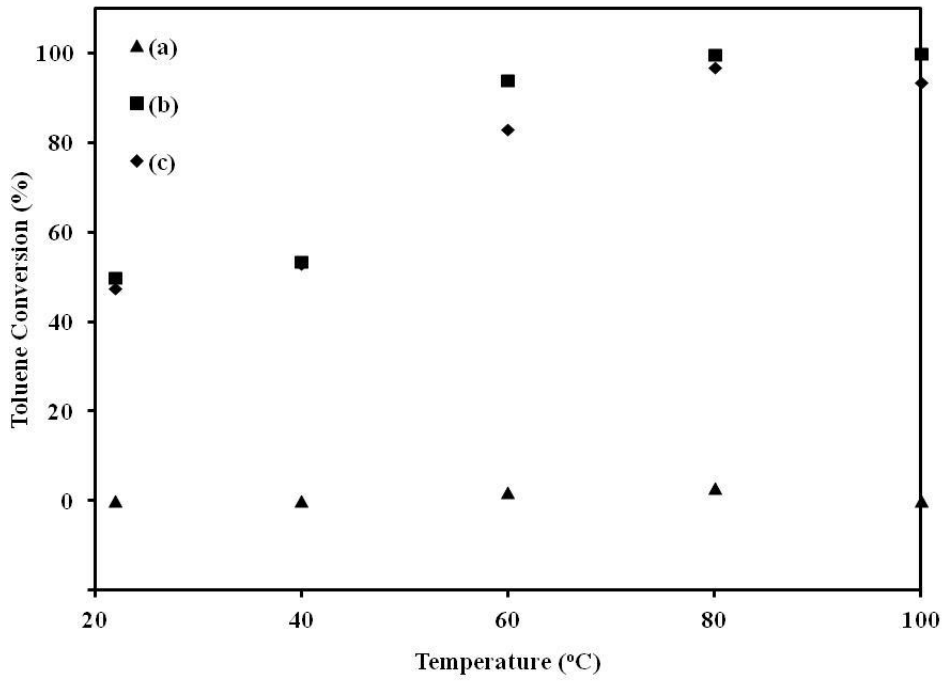

Fig. 4.8. Toluene conversion versus temperature, (a) in the absence of ozone, N_2 mole fraction ≈ 40%, O_2 mole fraction ≈ 60% (b) actual air composition with N_2 mole fraction ≈ 80% and O_2 mole fraction = 20%, and (c) N_2 mole fraction ≈ 40%, O_2 mole fraction ≈ 60%.

The same trend of activity is observed when toluene was oxidized in actual air composition. However, slightly higher activities are obtained in actual air composition due to higher ratio of ozone to toluene. This shows that the oxidation of toluene is not very sensitive to

the composition of air and it is mostly related to the concentration of ozone which is assumed to be the main oxidant in this system.

4.2.2. Reaction by-products

CO and CO_2, (CO_x), are the main products of the catalytic ozonation of toluene over 0.2 g of MnO_x/γ-alumina (10%). Fig. 4.9 presents the concentration of CO and CO_2 measured in the temperature range of 22-100 ^oC. It can be seen that CO and CO_2 concentrations are very low at room temperature due to the low conversion of toluene and the accumulation of carbon species on the catalysts. As the reaction temperature increases, the yield of the reaction to CO_x increases and reaches a maximum (≈ 90%) at 80 ^oC.

The carbon balance of the reactor is shown in Fig. 4.10. The carbon balance is around 90% at temperatures that the catalyst, MnO_x/γ-alumina (10%), works steadily (above 65 ^oC) and around 80% at room temperature. The difference in the carbon balance is attributed to the production of by-products other than CO and CO_2 and the accumulation of carbon species on the catalysts below 65 ^oC.

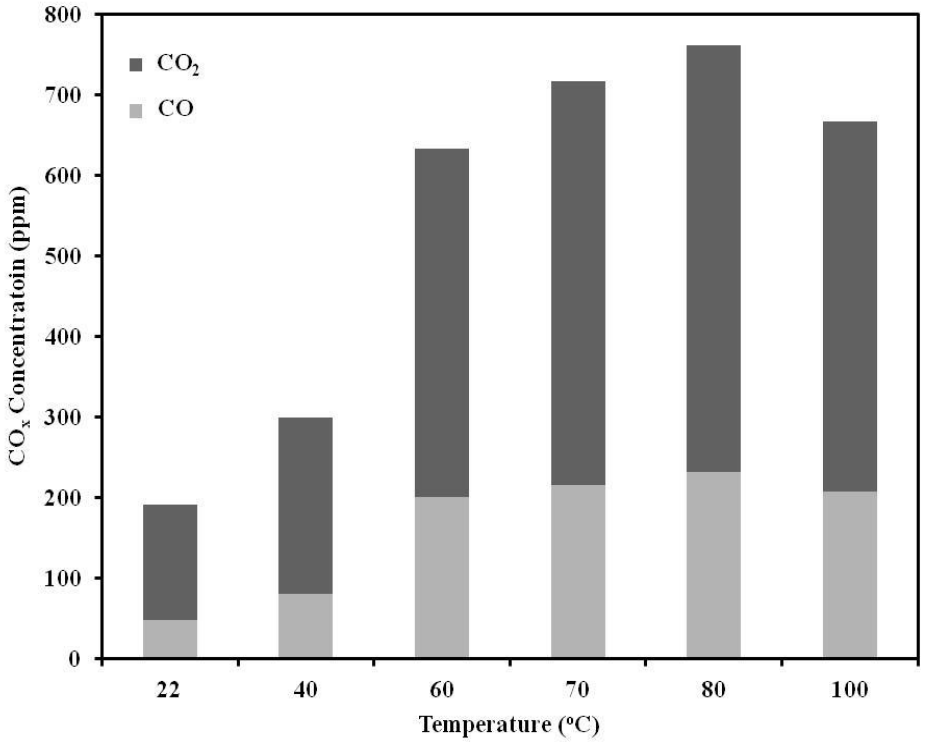

Fig. 4.9. Concentration of CO and CO_2 at different temperatures.

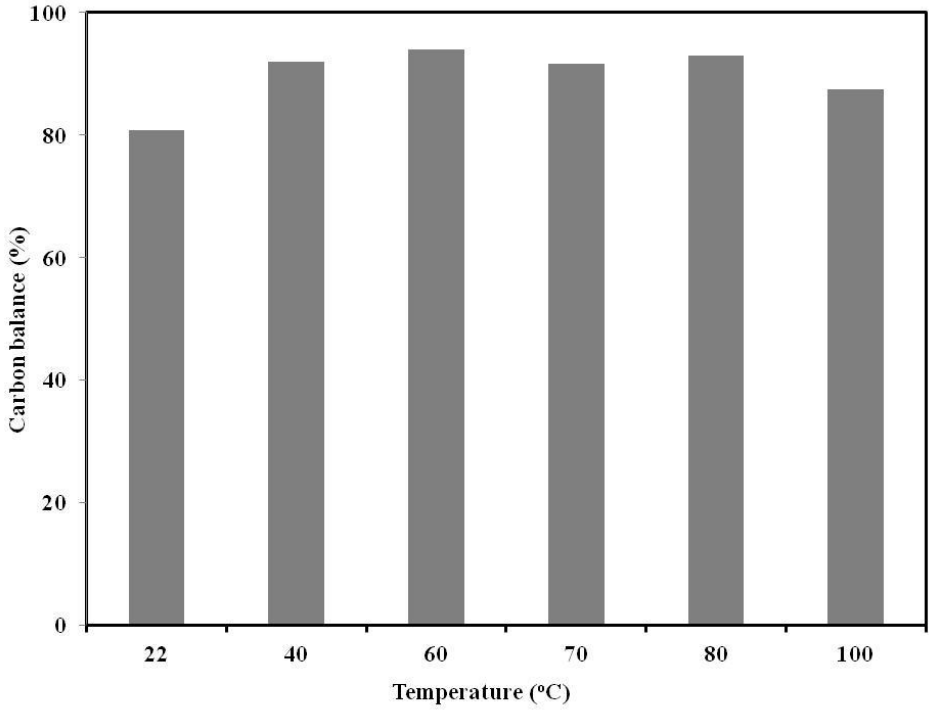

Fig. 4.10. Carbon balance of the reactor.

Fig. 4.11 shows a total ion chromatograph (TIC) of reaction products of catalytic ozonation of toluene on MnO_x/γ-alumina (10%) at 80 ^oC, collected by the mass spectrometer. Oxalic acid, acetic acid, benzene, and maleic anhydride are detected as the minor reaction by-products. The difference in the carbon balance (10% carbon loss during the steady state operation of the catalyst) is due to the formation of these by-products produced as the result of incomplete oxidation of toluene. Monneyron et al. have studied a combined adsorption-ozonation process for the removal of toluene by zeolites [65].Using GC-MS, they showed that CO_2, water, formic acid, oxalic acid, acetic acid, and acetaldehyde are the main reaction byproducts of the ozonation of adsorbed toluene on Fau Y zeolite. Although they have not used any metal oxides impregnated on Fau Y and their process is based on saturation of zeolites followed by the ozonation of the adsorption bed, oxalic acid and acetic acid are two common by-products found in the present work and the work by Monneyron et al.

If one assumes that only atomic oxygen is involved in the oxidation of toluene and the only reaction byproduct is CO_2, the following equation can describe the maximum ozone to toluene ratio required for complete oxidation of toluene:

$$C_7H_8 + 18O_3 \rightarrow 18O_2 + 7CO_2 + 4H_2O \quad (4.5)$$

In this work ozone to toluene ratio is 8.75 which is almost half of the theoretical reaction stoichiometry. In fact, ozone is the limiting reactant in our work and the limitation of oxygen species can explain the formation of byproducts indicated in Fig. 4.11. Einaga and Futamura hypothesized that not only ozone but also oxygen can participate in the oxidation of benzene. They proposed that oxygen is involved in some form of auto-oxidation reactions to oxidize radical reaction intermediates to CO and CO_2 [56]. This hypothesis along with the production of CO besides CO_2 can explain how ozone to toluene ratio of 8.75, which seems to be far from the

reaction stoichiometry, leads to 90% carbon balance. Increase of ozone concentration to 2200 (ozone to toluene ratio of 18.3) ppm led to near 100% carbon balance at 100 ^{o}C with CO and CO_2 concentrations of 205 and 633 ppm, respectively. This shows that when enough oxygen atoms are provided, CO and CO_2 are the only byproducts of reaction. However, even when ozone to toluene ratio is close to the theoretical stoichiometric value, there is still some CO formation indicating incomplete oxidation of toluene.

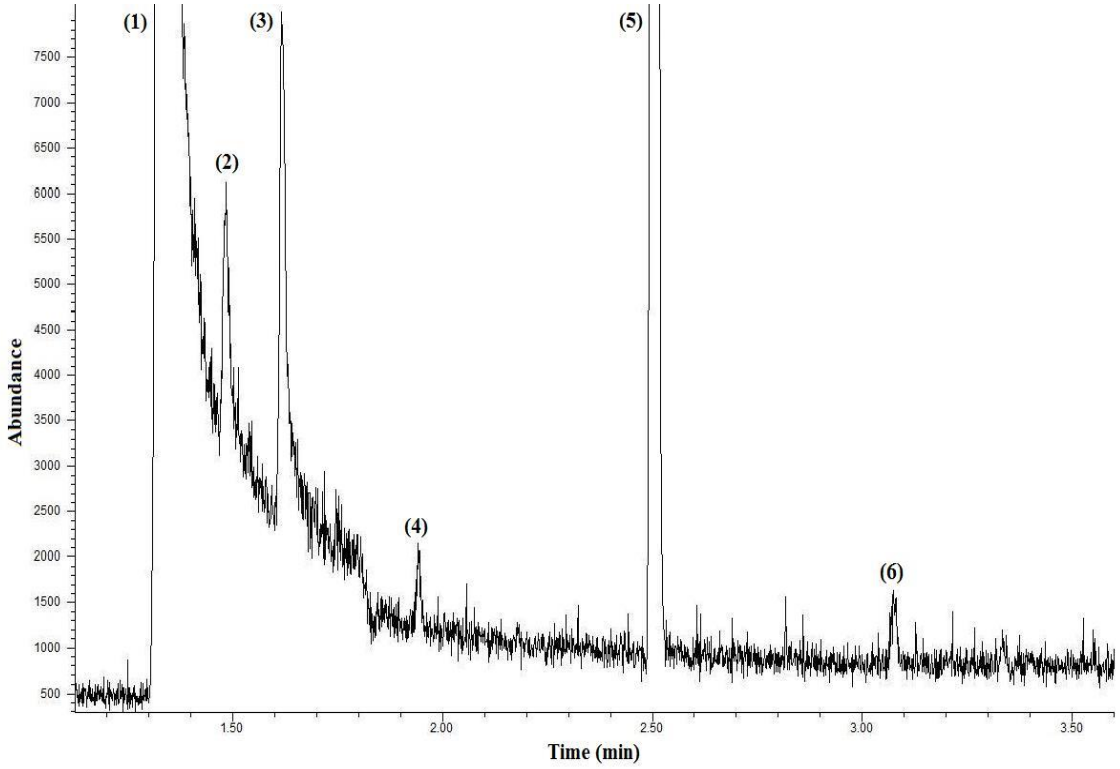

Fig. 4.11. Total ion chromatograph (TIC) of reaction byproducts at 80 ^{o}C obtained on MnO_x/γ-alumina (Nit), (1) N_2-O_2, (2) oxalic acid, (3) acetic acid, (4) benzene, (5) toluene, and (6) maleic anhydride.

4.3. Summary

Manganese oxides were impregnated on γ-alumina (S_{BET} = 212 m^2 g^{-1} and V_{pore} = 0.60 cm^3 g^{-1}) from the nitrate precursor of Mn which is manganese (II) nitrate tetrahydrate. The loading of Mn was 10% by weight. The catalyst was called MnO_x/γ-alumina (10%). The final catalyst was characterized by X-ray diffraction (XRD), laser Raman spectroscopy, and X-ray near edge structure (XANES). The results of XRD analysis showed that MnO_2 (pyrolusite) and Mn_2O_3 (bixbyite) formed on γ-alumina. Dispersion of Mn was calculated to be 6.1 and 3.8% for MnO_2 and Mn_2O_3, respectively. Laser Raman spectroscopy also confirmed the presence of Mn_2O_3 particles in the catalyst, even though no MnO_2 was detected by Raman spectroscopy. XANES analysis showed that the near edge spectra of the catalyst was located between that of MnO_2 and Mn_2O_3 reference materials, indicating that two phases of manganese oxides can be found in the catalyst. Linear combination fitting of the catalyst with MnO_2 and Mn_2O_3 reference materials revealed that 9% of manganese oxides are in the form of MnO_2 and 91% are in the form of Mn_2O_3.

Toluene oxidation was carried out in the temperature range of 22-100 ^oC using 0.2 g of the catalyst. Results show that the catalyst lost its activity below 65 ^oC due to the accumulation of carbon containing species on the catalyst surface. Almost complete conversion of toluene was achieved at 80 ^oC. Experiments with the support alone (γ-alumina) revealed that the most active part of the catalyst was manganese oxides. Considering the characterization results, Mn_2O_3 can be suggested to be the catalyst active site in MnO_x/γ-alumina (10%). CO and CO_2 were determined to be the major reaction products, leading to 90% carbon balance at 80 ^oC. Minor reaction by-products were identified by the mass spectrometer. Oxalic acid, acetic acid, benzene, and maleic anhydride were detected in addition to CO and CO_2, implying incomplete oxidation

of toluene. The mechanism of the reaction was assumed to be based on the decomposition of ozone on manganese oxides to peroxide and atomic oxygen. The produced surface oxygen atoms are highly reactive capable of oxidizing toluene molecule. It was observed that at higher ozone to toluene ratios, carbon balance approaches 100% with CO and CO_2 as the only reaction products.

CHAPTER 5
EFFECT OF CATALYST LOADING ON ACTIVITY OF ALUMINA SUPPORTED MANGANESE OXIDES

As it was observed in chapter 4, MnO_2 and Mn_2O_3 are the oxide phases of manganese found in MnO_x/γ-alumina (10%). In order to investigate the relationship between the phases of manganese oxides and the activity of alumina supported manganese oxides, four catalysts with different Mn loadings (1, 5, 10, and 20%) are studied in this chapter. The catalysts activities are presented in the temperature range of 22-80 ^oC for the oxidation of toluene. Catalyst active sites are characterized by X-ray diffraction (XRD), X-ray absorption near edge structure (XANES) and extended X-ray absorption fine structure (EXAFS). There are a few studies on the atomic structure of manganese oxides performed by EXAFS [29, 58, 86-88].The EXAFS study of MnO_2 is rather straightforward since it has only one Mn site. But difficulty arises in the EXAFS analysis of Mn_2O_3 and Mn_3O_4 due to the existence of two Mn sites and several sets of oxygen atoms located closely at the first shell around the Mn sites. These oxygen atoms are usually 0.1 to 0.3 Å apart, making it difficult for them to be distinguished by the sole EXAFS fitting procedure. Therefore, more emphasis is put on the EXAFS study of the reference materials (MnO_2 and Mn_2O_3) and the catalysts in this chapter. EXAFS of Mn_2O_3 is presented in more detail in order to build rigorous theoretical models to perform EXAFS analysis of this oxide. A brief introduction on X-ray absorption spectroscopy is also given at the beginning of Chapter 5 to provide readers with the basics of XANES and EXAFS. The goal of chapter 5 is to relate the observed catalyst activities to the electronic and structural properties of the catalysts with different Mn loadings.

5.1. X-ray absorption spectroscopy (XAS)

The atoms of elements can be excited by the absorption of the energy of X-ray photons. If the energy of the emitting X-ray is less than the binding energy of electrons, the electrons are promoted to unoccupied higher energy level orbitals, creating core holes in their original oribatals, from which they have been removed. The transition of electrons from lower energy orbitals to higher energy orbitals follows the dipole selection rule, by which only certain transitions are permitted between orbitals [89]. The excited electrons are called photoelectrons. The core hole will be filled with electrons in higher energy levels in a femto-second (10^{-15} s) [89]. The transition of electrons from higher to lower energy levels causes release of Auger electrons, fluorescence radiation, and photons. The absorption of X-ray by a material can be expressed by Beer-Lambert's law [89]:

$$I_t = I_o e^{-\mu x} \tag{5.1}$$

I is the intensity of the X-ray and subscripts t and o are used for transmitted and incident X-ray, respectively. μ is the absorption coefficient and x is the thickness of the matter. The amount of the X-ray energy absorbed by a specific element depends on the density of the sample, the atomic mass and the atomic number of the atoms within the material [90]. As an example, the normalized absorption spectrum of Mn *K-edge* of Mn_2O_3 is shown in Fig. 5.1, in which the normalized absorption is plotted as a function of the energy of X-ray. The spectrum consists of two main parts which are called X-ray absorption near edge structure (XANES) and extended X-ray absorption fine structure (EXAFS). The XANES part starts a few hundred electronvolts below the excitation energy of the electrons in Mn 1S orbital. By increasing the energy of the X-ray, electrons are excited from the 1S orbital to 4P orbitals, making the rising part (white line) of

the spectrum. XANES data can be used to determine the formal oxidation state of an atom. It may also provide information about the geometry of atoms around the absorbing atom.

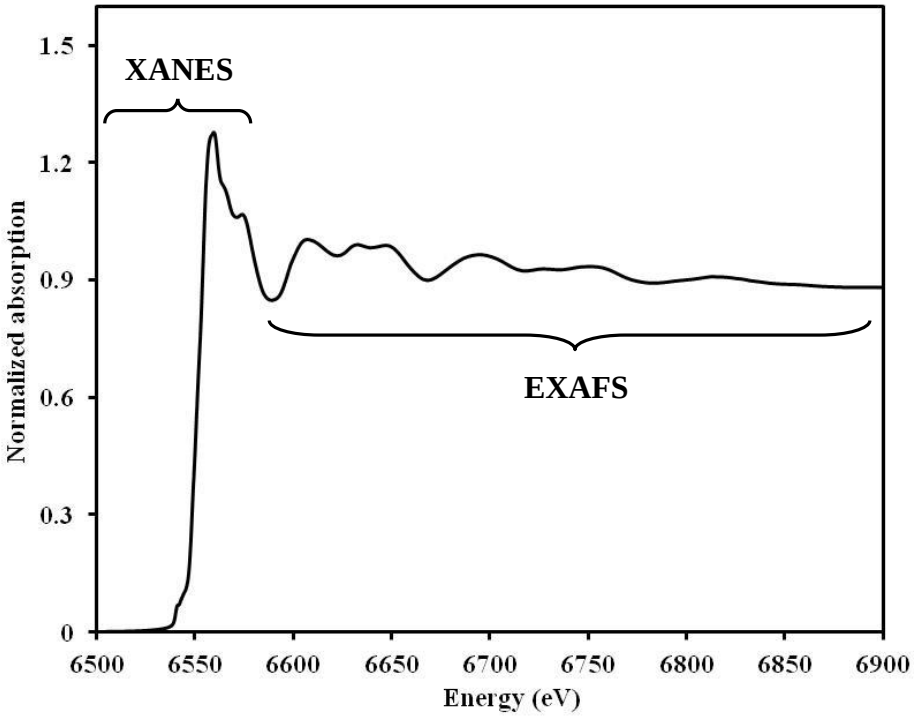

Fig. 5.1. X-ray absorption spectrum of Mn *K-edge* of Mn_2O_3.

By further increase of the X-ray energy, the photoelectrons are removed from the atom and sent to the continuum. Photoelectrons propagate as three-dimension waves among atoms and are scattered from neighboring atoms back to the absorbing atom. Therefore, interactions occur among the outgoing photoelectron waves and the backscattered waves at the absorbing atom, affecting the absorption of X-ray. If the two waves (emitted and backscattered) are in phase, a maximum can be seen in the absorption spectrum. On the other hand, if the waves are out of phase, a minimum occurs in the absorption spectrum. The oscillatory part of the spectrum above the edge is called extended X-ray absorption fine structure (EXAFS). Usually there are

several atoms at different distances around the absorbing atom which can back scatter the photoelectrons. Each set of these atoms at equal distances from the absorbing atom is called a shell. The journey of the photoelectrons from the absorbing atom to the neighboring atoms and back to the absorbing atom is identified as a path. A single scattering path contains only one neighboring atom while a multiple scattering path may consist of several neighboring atoms at different shells. This makes the EXAFS an atomic scale probe to investigate the atomic environment of an atom. The atomic range investigated by the EXAFS is about 6 Å [89]. The EXAFS oscillations are defined from the experimental data by [90]:

$$\chi(E) = \frac{\mu(E) - \mu_o(E)}{\Delta\mu_o(E)} \tag{5.2}$$

μ (E) is the absorption coefficient at X-ray energy of E and μ_o(E) is the smoothed background in the EXAFS region. $\Delta\mu_o$(E) is the absorption jump at the absorption edge. Photo-electrons' wave number (k) is usually used instead of the X-ray energy (E) to define the EXAFS function. The k dependent EXAFS function is shown by χ(k) in which, k is related to E by [90]:

$$k = \sqrt{\frac{2m(E - E_o)}{\hbar^2}} \tag{5.3}$$

m is the mass of the electron and ħ is the Plank's constant. E_o is the energy of absorption in electronvolts (eV) and k is in $Å^{-1}$.

The theory of the EXAFS phenomenon has been well developed now and it is possible to extract information such as coordination numbers, inter-atomic bond lengths and bond disorders from the EXAFS experimental data [91-93]. The theoretical EXAFS equation for the i^{th} path can be written as [89]:

$$\chi_i(k) = \frac{(CN_i S_o^2) F_{eff_i}(k)}{kR_i^2} e^{-2\sigma_i^2 k^2} e^{-2R_i/\lambda(k)} \sin\left[2kR_i + \varphi_i(k)\right] \tag{5.4}$$

k and R_i are given by:

$$k = \sqrt{\frac{2m(E - E_o + \Delta E_o)}{\hbar^2}}, \quad R_i = R_{Reff_i} + \Delta R_i \tag{5.5}$$

The total EXAFS oscillation can be obtained by considering the contributions of all paths as a sum over all $\chi_i(k)$:

$$\chi(k) = \sum_i \chi_i(k) \tag{5.6}$$

$\lambda(k)$, $\varphi_i(k)$ and F_{eff_i} in Eq. (5.4) are the photoelectrons mean free path, phase shift, and the effective amplitude of the backscattered photoelectron, respectively. The phase shift occurs since the photoelectron encounters the atomic potentials of the absorbing and the neighboring atoms as they travel in a path. These three parameters ($\lambda(k)$, $\varphi_i(k)$ and F_{eff_i}) are calculated from theoretical quantum mechanics. FEFF is a computer code which is usually used to estimate these parameters [77]. $(CN_i S_o^2)$ is multiplied to F_{eff_i} to correct the EXAFS signal amplitude. CN is the coordination number for single scattering paths or the number of similar paths in multiple scattering paths. S_o^2 is the amplitude reduction factor which is related to the relaxation of electrons after the core hole is generated. Typical values of S_o^2 are between 0.7 and 1.0. σ^2 is the mean square displacement in the inter-atomic bond distance, representing the thermal and structural disorders in a crystal structure. R_{Reff_i} is the inter-atomic distance obtained from the crystallography data and ΔR_i is the change in R_{Reff_i} which is less than 0.1 Å [89]. ΔE_o is the difference in the energy scale between the theory and data.

Since the EXAFS signal is made of the interaction of sine waves, Eq. (5.6), the Fourier transform is used to extract the frequency of each wave at distance R (Å) from the absorbing atom [89]. In fact, by taking the Fourier transform, one can move from energy space (k) to R-

space in order to find the amplitude and phase of each shell. The amplitude and the phase are related to the coordination number of atoms at each shell, the type of neighboring atoms, and the distance of atoms from the absorbing atom [89].

In order to model the experimental EXAFS signal by Eq. (5.6), one can evaluate ΔE_o, ΔR, σ^2, and $(CN_i S_o^2)$ for each path by fitting the experimental EXAFS spectrum to Eq. (5.6). This is done by fitting the real and imaginary parts of the EXAFS Fourier transformed signal in available computer programs such as Artemis [77, 94]. The fitting consists of non-linear minimization of the sum of squared errors between data and the theory in R space [79]:

$$\chi^2 = \frac{N_{idp}}{N_{pts}\varepsilon^2}\sum_{i=1}^{N_{pts}}\left\{\left[\mathrm{Re}\left(\tilde{\chi}_{data}(R_i)-\tilde{\chi}_{theory}(R_i)\right)\right]^2+\left[\mathrm{Im}\left(\tilde{\chi}_{data}(R_i)-\tilde{\chi}_{theory}(R_i)\right)\right]^2\right\} \quad (5.7)$$

χ^2 is the objective function which should not be mistaken as the EXAFS signal expressed by Eq. (5.6). Re and Im denote the real and imaginary parts of the Fourier transformed EXAFS signal. The tilde above χ shows the Fourier transformation of the EXAFS. N_{pts} and N_{idp} are the number of fitting parameters and the number of independent points, respectively. N_{idp} is determined by:

$$N_{idp} = \frac{2\Delta k \Delta R}{\pi} + 1 \quad (5.8)$$

Δk is the range used to take the Fourier transform and ΔR is the range of the fitting in R space. ε is the measurement uncertainty. It can be estimated by calculating the mean square of $\tilde{\chi}(R)$ in the range of 15-25 Å, assuming that there is no contribution from atomic shells in this range.

The goodness of EXAFS fits is usually expressed by R factor (R_f) which is the absolute misfit between the experimental data and the theory. R_f is given by [79]:

$$R_f = \sum_{i=1}^{N_{pts}}\frac{\left[\mathrm{Re}\left(\tilde{\chi}_{data}(R_i)-\tilde{\chi}_{theory}(R_i)\right)\right]^2+\left[\mathrm{Im}\left(\tilde{\chi}_{data}(R_i)-\tilde{\chi}_{theory}(R_i)\right)\right]^2}{\left[\mathrm{Re}\left(\tilde{\chi}_{data}(R_i)\right)\right]^2+\left[\mathrm{Im}\left(\tilde{\chi}_{data}(R_i)\right)\right]^2} \quad (5.9)$$

Smaller values of R_f show that fits are better performed. In order to compare the fitting of different models for the same data set, reduced χ^2 is used. It is shown by χ^2_ν and is given by:

$$\chi^2_\nu = \frac{\chi^2}{\nu} \tag{5.10}$$

ν is the degree of freedom of the data which is defined by the difference between N_{pts} and N_{idp}. χ^2 is given by Eq. (5.7). A fit can be said to be improved if χ^2_ν is reduced by a factor of $1+2\sqrt{2/\nu}$ [79]. The precision of EXAFS in the determination of bond distances is about 0.02 Å while the resolution ($\Delta R^{'}$) can be estimated by [93]:

$$\Delta R^{'} = \frac{\pi}{2\Delta k} \tag{5.11}$$

Most often, the resolution of EXAFS fittings is between 0.1 to 0.2 Å.

5.2. EXAFS study of MnO_2 and Mn_2O_3 reference materials

As it can be seen in Eq. (5.4), the coordination numbers (CN) and the amplitude reduction factor (S_o^2) are 100% correlated. Therefore, it is not possible to determine the coordination number of oxygen and manganese shells in the catalysts without having a prior knowledge of S_o^2. S_o^2 is usually obtained from the EXAFS spectra of reference materials by fixing the coordination numbers from crystallography data. The S_o^2 is assumed to be the same in the data collection period of catalysts and reference materials. Therefore, S_o^2 obtained from the reference materials can be used as a fixed parameter for the EXAFS analysis of the catalysts to find the coordination numbers. Thus, EXAFS fittings of the reference materials (MnO_2 and Mn_2O_3) are explained in this section, resulting in S_o^2 which can be used in section 5.3 to investigate the changes in coordination numbers as the result of the change in Mn loading.

5.2.1. MnO_2

Unit cell dimensions of MnO_2 are presented in Table 4.2. The space group of MnO_2 is P42/m n m. A spatial structure of MnO_2 can be observed in Fig. 5.2 generated by PowderCell 2.4. MnO_2 has originally two oxygen atoms at 1.877 Å and four oxygen atoms at 1.891 Å [29]. But due to their close atomic positions, 6 oxygen atoms at an average distance of 1.887 Å are considered for MnO_2 EXAFS analysis. Results of EXAFS study of MnO_2 are presented in Fig. 5.3 and Table 5.1. The fitting is performed using k-weight of 1 in k and R ranges of 3-13 $Å^{-1}$ and 1-4 Å, respectively. Sine windows are used for k and R windows with Δk and ΔR of 1 $Å^{-1}$ and 0 Å, respectively.

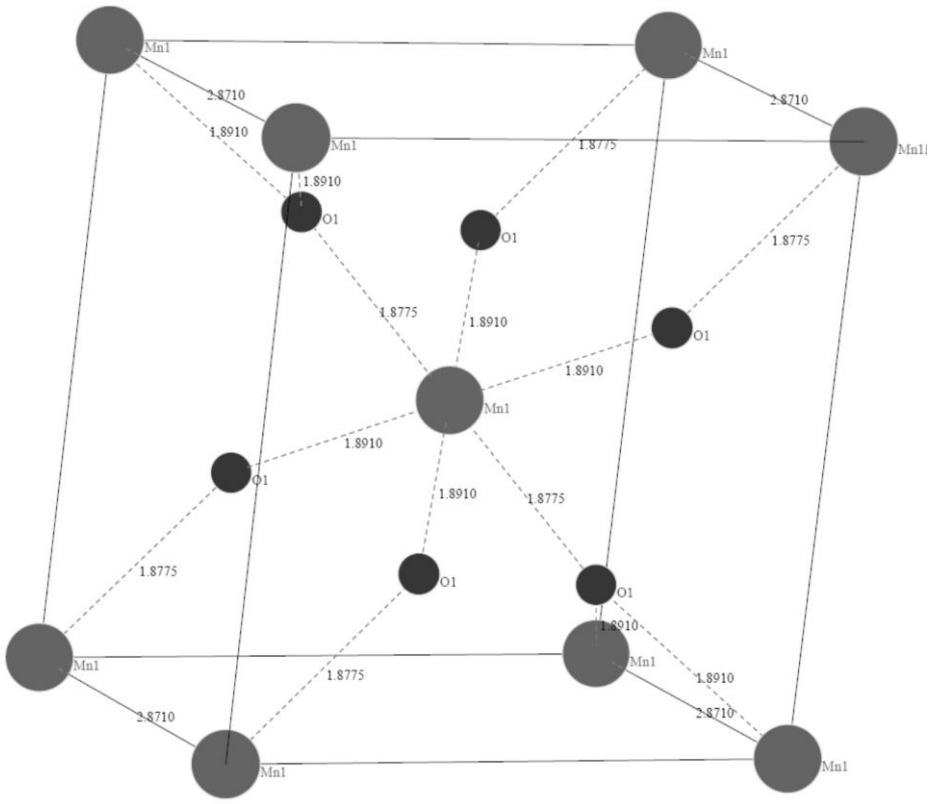

Fig. 5.2. Unit cell structure of MnO_2. Numbers are in Å.

Three paths including the first oxygen shell and the first and second Mn shells are included in the model to simulate the EXAFS signal of MnO_2. The fitting results in an amplitude reduction factor of 0.68 ± 0.06. It has to be noted that coordination numbers (CN) are fixed from the crystallography information of MnO_2.

Table 5.1. EXAFS fitting result of MnO_2

	Path	CN (fixed)	σ^2 ($\times 10^{-3}$ Å^2)	R (Å)	E_o (eV)	R_f (%)
MnO_2	Mn-O	6	1.8 ± 1.0	1.872 ± 0.007	0.15 ± 1.0	1.8
	Mn-Mn	2	1.4 ± 1.2	2.871 ± 0.013		
	Mn-Mn	8	4.0 ± 1.0	3.424 ± 0.010		

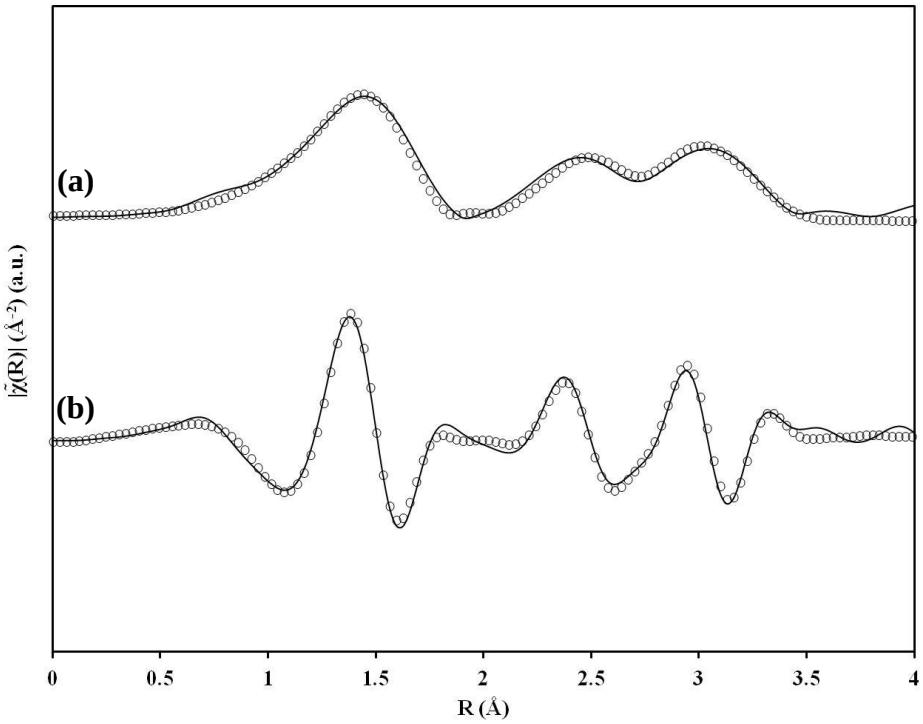

Fig. 5.3. Magnitude (a) and real part (b) of the EXAFS spectra of MnO_2 reference material. Solid lines represent the data and the symbols are the fittings.

Fig. 5.3 shows the magnitude and real part of MnO_2 EXAFS and the fitting results. The first peak in Fig. 5.3(a) is due to the first shell oxygen atoms. The second peak is due to the first Mn shell while the third peak can be related to farther atomic shells. It can be seen that the fitting curves follow closely the data, resulting in absolute percentage misfit (R_f) of 1.8%.

5.2.2. Mn_2O_3

The unit cell dimensions of Mn_2O_3 are available in Table 4.2 with the space group of Ia3. Mn_2O_3 has a more complicated unit cell structure than MnO_2. There are two Mn sites in Mn_2O_3 with occupancy of 25 and 75%. The crystal structure information of Mn_2O_3 up to ca. 3.5 Å is

given in Table 5.2. Mn site 1 (Mn1) with 25% occupancy, has 6 oxygen atoms at 1.993 Å while Mn site 2 (Mn2) has three sets of oxygen atoms at different bond lengths. There are 2 short oxygen bonds at 1.899 Å and two long oxygen bonds at 2.248 Å in Mn site 2. In addition to these 4 oxygen atoms, there are two oxygen atoms at 1.985 Å in Mn site 2 which are extremely close to the oxygen bond length in Mn site 1 at 1.993 Å. The spatial schematic of the two Mn sites can be seen in Fig. 5.4 produced by PowderCell 2.4.

Table 5.2. Crystal structure of Mn_2O_3

Mn_2O_3						Mn_2O_3 [a]		
Mn1 (25%)			Mn2 (75%)					
Bond	CN [b]	R_{reff} (Å) [b]	Bond	CN [b]	R_{reff} (Å) [b]	Bond	CN	R_{reff} (Å)
Mn-O	6	1.993	Mn-O	2	1.899	Mn-O	1.5	1.899
Mn-Mn	6	3.104	Mn-O	2	1.985	Mn-O	3	1.987
Mn-Mn	6	3.565	Mn-O	2	2.248	Mn-O	1.5	2.248
			Mn-Mn	6	3.115	Mn-Mn	6	3.112
			Mn-Mn	6	3.575	Mn-Mn	6	3.572

[a] Averaged based on Mn site occupancies.

[b] Obtained from crystallography data.

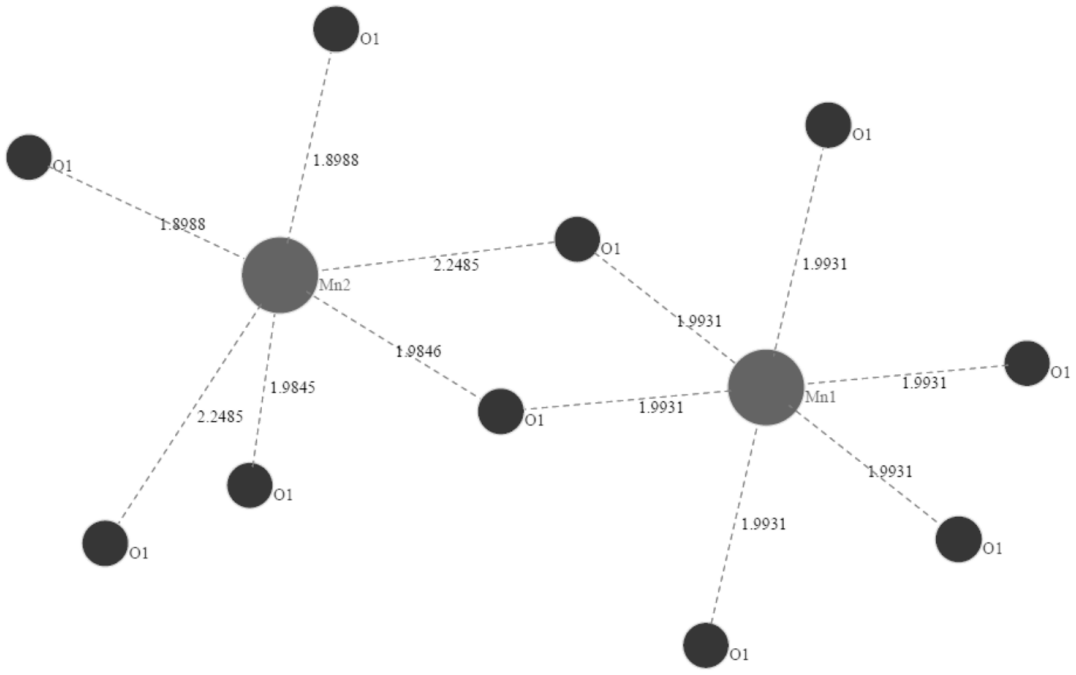

Fig. 5.4. Spatial structure of Mn site 1 (Mn1) and Mn site 2 (Mn2) in Mn_2O_3, numbers are in Å.

The presence of two Mn sites in Mn_2O_3 makes the EXAFS analysis complicated due to the close atomic coordinates of oxygen in the two sites. There are two methods which can be used to model the EXAFS signal of Mn_2O_3. The first method simplifies the structure of Mn_2O_3 by averaging the two Mn sites based on their site occupancies. This integrates the Mn sites into one single site which can be used for EXAFS analysis. The second method is Bond Valence Model which is based on Pauling's 2nd rule of electrostatic valence [95]. The Bond Valence Model relates the oxidation state of Mn atoms to the CN of oxygen atoms, adding constrains on the EXAFS fitting procedure. This allows modeling the structure of Mn_2O_3 in a more general way with no simplifying assumption. The remaining of this section represents and compares the results of EXAFS fitting of Mn_2O_3 reference material by the two mentioned methods in order to

model complicated crystals such as Mn_2O_3. EXAFS fitting are carried out with k-weight of 1 for the Mn_2O_3 reference material. Sine window function with Δk and ΔR of 1 $Å^{-1}$ and 0 Å is used, respectively. The Fourier transforms are taken between 3-13 $Å^{-1}$. EXAFS Fittings are performed in R space from 1 to 3.7 Å.

Averaging method:

The simplified structure of Mn_2O_3 by averaging Mn site 1 (Mn1) and Mn site 2 (Mn2) is shown in the right column of Table 5.2. The averaging method results virtually in 1.5, 3, and 1.5 oxygen atoms at ca. 1.90, 1.99, and 2.25 Å, respectively. First and second shells of Mn atoms are located at ca. 3.11 and 3.57 Å, respectively. Table 5.3 contains the result of EXAFS fitting of Mn_2O_3 based on the averaging method and Fig. 5.5 shows the magnitude and the real part of the Fourier transform of the data and the fitting.

Table 5.3. EXAFS fitting result of Mn_2O_3 based on the averaging method

$S_o^2 = 0.83 \pm 0.12$, $E_o = 3.48 \pm 1.31$, $R_f = 1.9\%$, $\chi_v^2 = 3416$			
Path	CN	σ^2 ($\times 10^{-3}$ $Å^2$)	R (Å)
Mn-O	1.5	6.8 ± 2.1	1.883 ± 0.012
Mn-O	3	6.8 ± 2.1	1.969 ± 0.012
Mn-O	1.5	6.8 ± 2.1	2.233 ± 0.012
Mn-Mn	6	7.7 ± 1.5	3.113 ± 0.011
Mn-Mn	6	18.9 ± 4.9	3.617 ± 0.036

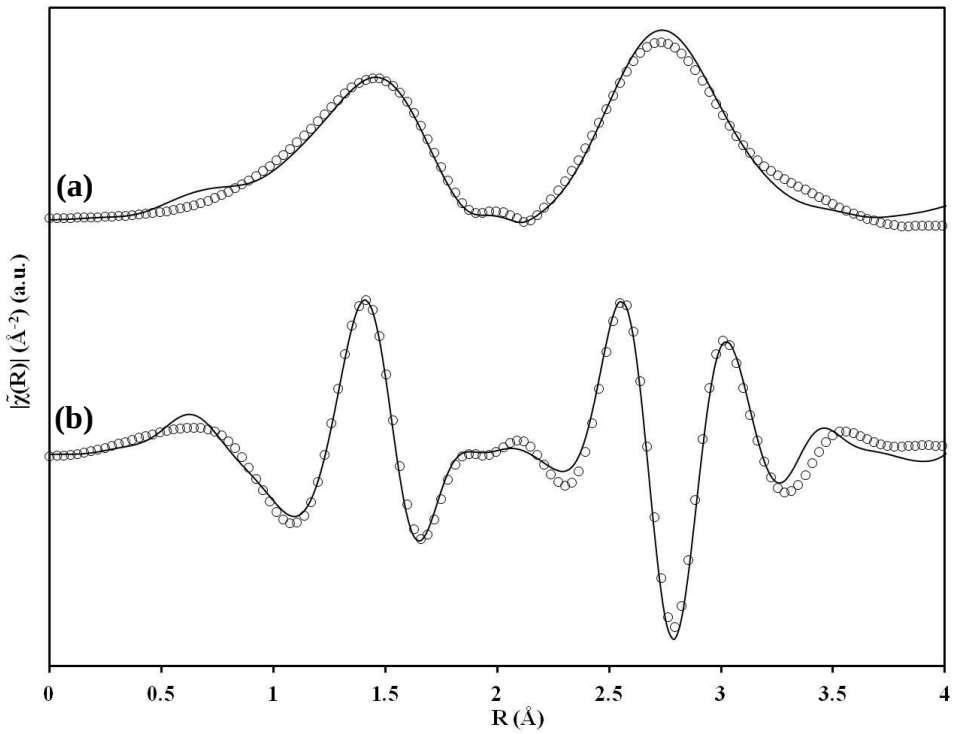

Fig. 5.5. Magnitude (a) and real part (b) of the EXAFS spectra of Mn_2O_3 reference material based on the averaging method. Solid lines represent the data and the symbols are the fittings.

Referring to Table 5.3, it can be seen that the averaging method results in an amplitude reduction factor (S_o^2) of 0.83 ± 0.12 and locates the first shell oxygen atoms at ca. 1.88, 1.97, and 2.33 Å with CN of 1.5, 3, and 1.5, respectively. Two Mn atoms are also resolved at the second and third shells at ca. 3.11 and 3.62 Å, respectively. There are almost 17 independent points in the fitting range and 8 fitting parameters in the averaging method, resulting in 9 degree of freedom.

Bond Valence Model:

In order to construct a more general model and also to check the validity of the averaging method, the Bond Valence Model is used to model the EXAFS of Mn_2O_3 [95]. According to this

model which is based on Pauling's 2nd rule of electrostatic valence, formal oxidation state of the cation i is equal to the sum of valence of the bond between the cation i and surrounding anions j:

$$V_i = \sum_j s_{ij} \tag{5.12}$$

in which the bond valence (s_{ij}) is defined by:

$$s_{ij} = \exp\left[\frac{R'_{ij} - R_{ij}}{b}\right] \tag{5.13}$$

R'_{ij} and b are empirical parameters and R_{ij} is the inter-atomic distance between the cation i and the anion j which can be coupled to EXAFS models. It has been shown that b has a universal value of 0.37 [95]. If there is only one type of anions around the cation, R_{ij} can be extracted from Eq. (5.13) and expressed as:

$$R_{ij} = R'_{ij} + 0.37\ln\left(\frac{CN_{ij}}{V_i}\right) \tag{5.14}$$

Where CN_{ij} is the coordination number of the anion j around the cation i at distance R_{ij}. Eq. (5.14) correlates the inter-atomic bond length to the coordination number of anions and oxidation state of the cation. This allows using a prior knowledge of the cation oxidation state, available from XANES analysis, in the EXAFS fitting which results in the reduction of the number of fitting parameters. Even though it is possible to directly use Eq. (5.14) in the EXAFS analysis to remove ΔR or CN from the fitting parameters, it is recommended to use Eq. (5.12) as a restraint to model EXFAS signals [95]. The reason relies on the inaccuracy of Eq. (5.12) and (5.13), leading to unreliable fitting parameters in EXAFS, when their exact definitions are used as constraints. Therefore, it is suggested to use the Bond Valence Model as a restraint in the EXAFS fitting of Mn_2O_3. This adds a penalty term on the EXAFS minimization objective function to keep the oxidation state of Mn cations close to their formal valence which is +3.

Considering the value of R'_{ij} (1.760) for Mn^{3+} in Mn_2O_3 [96], application of Eq. (5.12) and (5.13) results in the following equations for the two Mn sites:

$$V_{Mn,site1} = CN_O \exp\left(\frac{1.76 - R_{O,site1}}{0.37}\right) \tag{5.15}$$

$$V_{Mn,site2} = \left(\frac{CN_O}{3}\right)\exp\left(\frac{1.76 - R_{O1,site2}}{0.37}\right) + \left(\frac{CN_O}{3}\right)\exp\left(\frac{1.76 - R_{O,site1}}{0.37}\right) + \left(\frac{CN_O}{3}\right)\exp\left(\frac{1.76 - R_{O2,site2}}{0.37}\right) \tag{5.16}$$

Where CN_O represents the total number of oxygen atoms at the first shell of Mn_2O_3 which can be set at 6. $R_{O,site\ 1}$is used to represent the inter-atomic distance of the oxygen atoms at 1.993 and 1.985 Å in the first and second Mn sites, respectively. The distances of the other two oxygen atoms at 1.899 and 2.248 Å in Mn site 2 (Mn2) are denoted by $R_{O1,site\ 2}$ and $R_{O2,site\ 2}$, respectively. Eq. (5.15) and (5.16) are defined as restraints in Artemis with restricted values between 0 and 3 using a moderate penalty coefficient. It has to be noted that no simplification is performed in EXAFS fitting of Mn_2O_3 by the Bond Valence Model, allowing incorporation of both Mn sites in the model. The amplitude reduction factor is multiplied by Mn site occupancies in order to consider paths in each Mn sites.

Results of the fitting of Mn_2O_3 using the Bond Valence Model are shown in Table 5.4 and Fig. 5.6. The Bond Valence Model gives an amplitude reduction factor of 0.88 ± 0.16 with roughly 17 independent points, 10 fitting variables and 7 degree of freedom. There are 6 oxygen atoms at ca. 1.99 Å from Mn atom in site one whereas three sets of two oxygen atoms are located at ca. 1.87, 1.98, and 2.25 Å around the second Mn site. The first Mn shell is found around the first and second Mn sites at ca. 3.11 and 3.12 Å, respectively with CN of 6. The second Mn shell also has 6 Mn atoms which are located at ca. 3.61 and 3.62 Å away from Mn site 1 and site 2,

respectively. CNs reported in Table 5.4 are fixed parameters obtained from crystallography data of Mn_2O_3.

Table 5.4. EXAFS fitting result of Mn_2O_3 based on the Bond Valence Model

$S_o^2 = 0.88 \pm 0.16$, $E_o = 2.71 \pm 1.43$, $R_f = 1.7\%$, $\chi_v^2 = 4573$							
Mn site 1 (Mn1)				Mn site 2 (Mn2)			
Path	CN	σ^2 ($\times 10^{-3}$ Å^2)	R (Å)	Path	CN	σ^2 ($\times 10^{-3}$ Å^2)	R (Å)
Mn-O	6	6.5 ± 2.6	1.986 ± 0.031	Mn-O	2	6.5 ± 2.6	1.870 ± 0.064
Mn-Mn	6	8.3 ± 1.9	3.110 ± 0.012	Mn-O	2	6.5 ± 2.6	1.977 ± 0.031
Mn-Mn	6	21.0 ± 6.1	3.606 ± 0.041	Mn-O	2	6.5 ± 2.6	2.251 ± 0.035
				Mn-Mn	6	8.3 ± 1.9	3.118 ± 0.012
				Mn-Mn	6	21.0 ± 6.1	3.616 ± 0.041

By comparing the results of the two methods in Table 5.3 and 5.4, it can be seen that the obtained parameters are very close to each other. For example, σ^2 of the first shell of oxygen atoms obtained by the averaging method is 6.8×10^{-3} Å^2 while the one from the Bond Valence Model is 6.5×10^{-3} Å^2. The same similarities can also be seen in σ^2 of the Mn shells, the amplitude reduction factor (0.83 versus 0.88) and inter-atomic distances. The R_f (percentage of absolute misfit between the data and theory) of the averaging method and the Bond Valence Model are 1.9 and 1.7%, respectively. The reduced chi-square values, 3416 for the averaging method and 4573 for the Bond Valence Model, are also close to each other, showing that the two methods have almost the same statistical significance. This shows that both models can be used for EXAFS analysis of Mn_2O_3 containing catalysts. However, the Bond Valence Model can be

considered as a general model for the EXAFS fitting of complicated crystal structures such as Mn_2O_3 since it does not impose any simplification on the unit cell structure. Nevertheless, the Bond Valence Model proves that the averaging method results in feasible and valid solutions and can be used to model the EXAFS signal of oxides of manganese such as Mn_2O_3 and Mn_3O_4. An average value of 0.85 is assumed for the amplitude reduction factor of Mn_2O_3 from the result of this section. The averaging method will be used in order to study the EXAFS of alumina supported manganese oxides due to less complexity of this method.

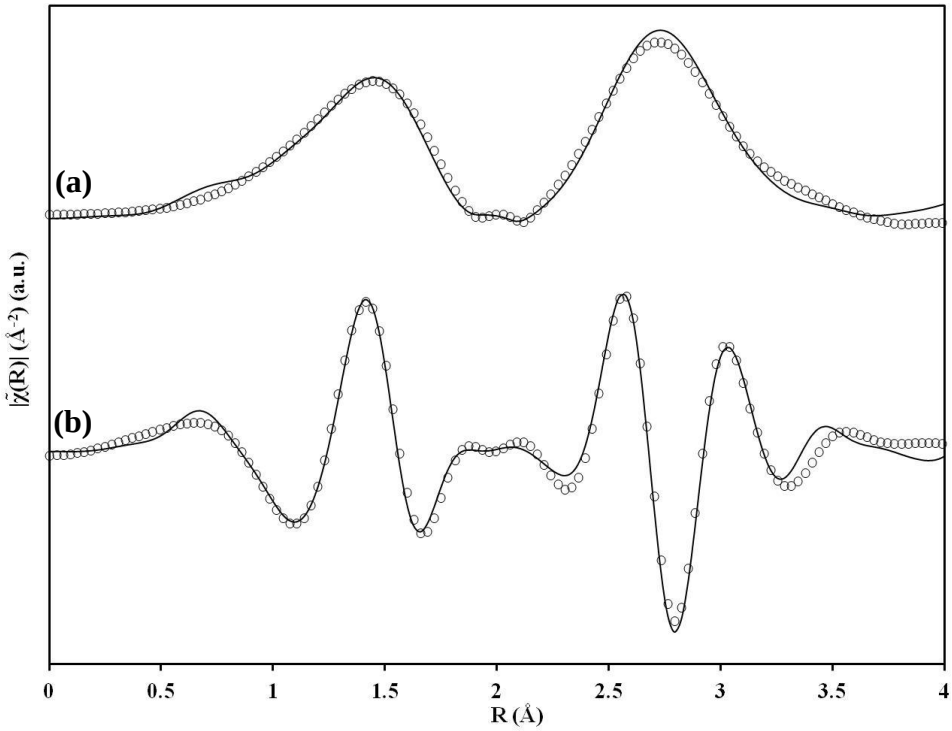

Fig. 5.6. Magnitude (a) and real part (b) of the EXAFS spectra of Mn_2O_3 reference material based on the Bond Valence Model. Solid lines represent the data and the symbols are the fittings.

It has to mentioned that the results of EXAFS studies reported in Table 5.3 and 5.4, are comparable with the EXAFS study of Mn_2O_3 (bixbyite) performed by Longo et al. [86].

Basically, the authors have modeled the theoretical EXAFS signal of Mn_2O_3 by considering 6 oxygen atoms at ca. 1.88 Å, 6 manganese atoms at ca. 3.12 Å and 6 manganese atoms at ca. 3.60 Å. They have fixed the oxygen and manganese coordination numbers along with a predetermined value of 0.74 for S_o^2. Their model has resulted in σ^2 of 7 $\times 10^{-3}$ Å^2 for the first oxygen shell which is very close to σ^2 reported in this work for Mn_2O_3 reference material, i.e. 6.8 $\times 10^{-3}$ Å^2 and 6.5 $\times 10^{-3}$ Å^2 for the averaging method and the Bond Valence Model, respectively.

5.3. Characterization of MnO_x/γ-alumina (1, 5, 10 and 20%)

Four loadings of Mn (1, 5, 10, and 20%) are used to prepare MnO_x/γ-alumina with different manganese loadings. Catalysts are characterized with X-ray diffraction (XRD) and X-ray absorption spectroscopy (XAS). More emphasis is put on XAS including XANES and EXAFS in order to find the relationship among the electronic and structural properties of manganese oxides and Mn loading.

5.3.1. X-ray diffraction (XRD)

Fig. 5.7 shows XRD of the catalysts and the reference materials including Mn_2O_3 and MnO_2. Peaks corresponding to the reference materials are marked with two dashed lines in order to track the peak locations on XRD of the catalysts. The catalyst with Mn loading of 1% does not show any diffraction peaks due to high dispersion of manganese oxides on alumina. But MnO_x/γ-alumina (5%) shows peaks, matching the spectra of Mn_2O_3. More strong peaks of Mn_2O_3 can be seen in XRD of MnO_x/γ-alumina (10%) along with weak peaks of MnO_2 showing that MnO_2 is coexisting with Mn_2O_3 in this catalyst. With the increase of Mn loading to 20%, more intense peaks of MnO_2 are observed while Mn_2O_3 peaks become smaller in XRD spectra of MnO_x/γ-

alumina (20%). This shows that by increasing Mn loading, different phases of manganese oxides are formed. At lower loading up to 10%, the dominant phase is Mn_2O_3 while at higher loadings, both MnO_2 and Mn_2O_3 phases coexist.

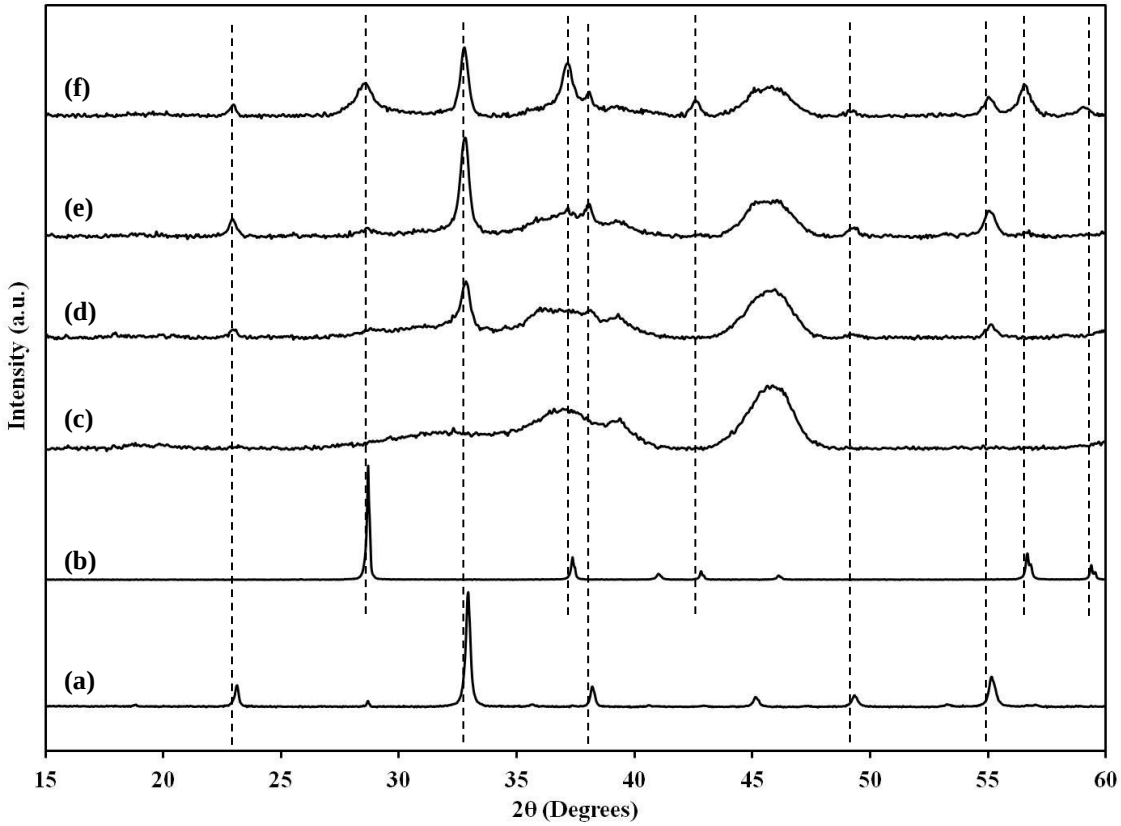

Fig. 5.7. XRD of reference materials and catalysts, (a) Mn_2O_3, (b) MnO_2, (C), MnO_x/γ-alumina (1%), (d) MnO_x/γ-alumina (5%), (e) MnO_x/γ-alumina (10%), and (f) MnO_x/γ-alumina (20%).

5.3.2. X-ray absorption near structure (XANES)

Mn *K-edge* XANES spectra of the reference materials (MnO_2 and Mn_2O_3) and the catalysts are shown in Fig. 5.8. It can be seen that the rising part of the spectra of the catalysts with 1 and 5% Mn loading are located at the left side of Mn_2O_3. XANES Spectrum of MnO_x/γ-alumina (10%) is closely located at the right side of Mn_2O_3, suggesting that this catalyst is

mainly composed of Mn_2O_3. The XANES spectra of the catalyst with 20% are well located between that of Mn_2O_3 and MnO_2, indicating that MnO_x/γ-alumina (20%) has considerable amount of MnO_2 in addition to Mn_2O_3.

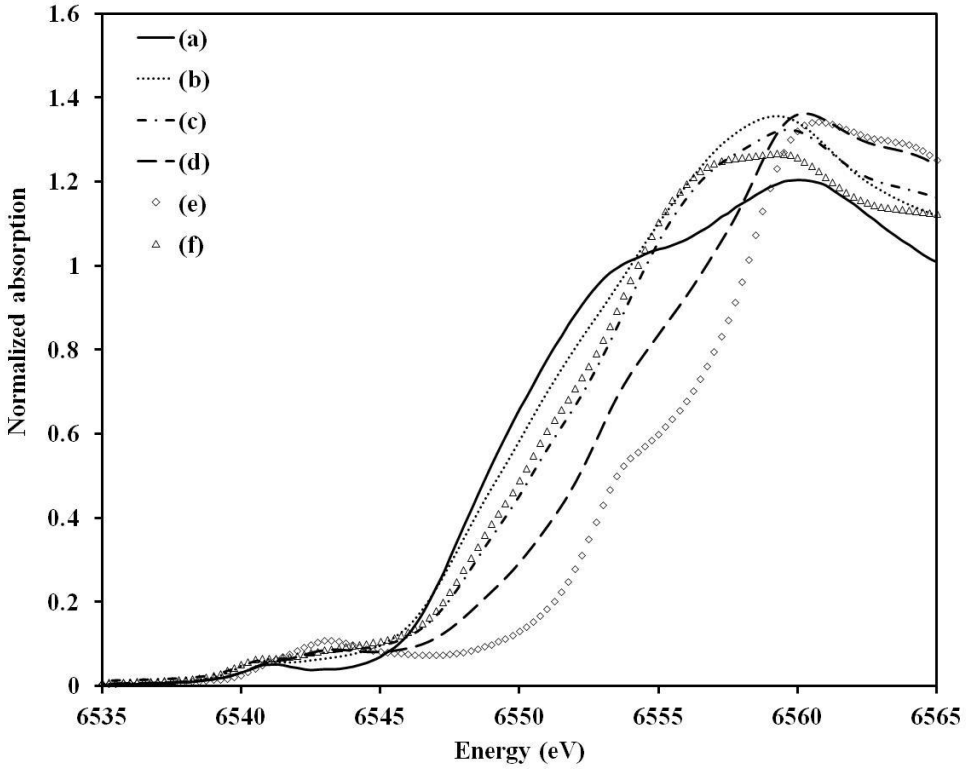

Fig. 5.8. Mn *K-edge* XANES spectra of the samples,(a) MnO_x/γ-alumina (1%), (b) MnO_x/γ-alumina (5%), (c) MnO_x/γ-alumina (10%), (d) MnO_x/γ-alumina (20%), (e) MnO_2, and (f) Mn_2O_3.

Mn *K-edge* absorption energy (E_o) of the reference materials are 6548.1 and 6552.7 eV for Mn_2O_3 and MnO_2, respectively. Absorption energies of the catalysts are presented in Table 5.5. MnO_x/γ-alumina (1 and 5%) catalysts have absorption energies less than that of Mn_2O_3 most probably due to the presence of highly dispersed manganese atoms and incomplete growth of Mn_2O_3 unit cells. On the other hand, catalysts with Mn loadings of 10 and 20% have absorption

energies higher than that of Mn_2O_3. The absorption energy of MnO_x/γ-alumina (10%) is 0.3 eV higher than E_o of Mn_2O_3 while the sample with 20% Mn has an absorption energy at 6552.7 eV which is the same as MnO_2 absorption energy.

Table 5.5. Mn *K-edge* absorption energies of the catalysts

	MnO_x/ γ-alumina (1%)	MnO_x/ γ-alumina (5%)	MnO_x/ γ-alumina (10%)	MnO_x/ γ-alumina (20%)
Mn *K-edge* E_o (eV)	6547.4	6547.8	6548.4	6552.7

Linear combination fitting of the catalysts (10 and 20% Mn loading) with the reference materials (MnO_2 and Mn_2O_3) shows that the weight percent of MnO_2 increases from 9.0 to 55.3% by increasing Mn loading from 10 to 20%. Meanwhile, the fraction of Mn_2O_3 drops from 91.0 to 44.7% from MnO_x/γ-alumina (10%) to MnO_x/γ-alumina (20%).This is in agreement with the XRD results, showing that more MnO_2 is formed in MnO_x/γ-alumina by increasing the loading from 10 to 20%.

5.3.3. Extended X-ray absorption fine structure (EXAFS)

Fig. 5.9 shows Mn *K-edge* EXAFS oscillation of the samples. The EXAFS spectra of the catalysts with 5 and 10% loading matches the spectra of Mn_2O_3 reference material. On the other hand, EXAFS oscillation of 1% Mn loaded catalyst is different from the spectra of MnO_2 and Mn_2O_3 due to the high dispersion of Mn. EXAFS of the catalyst with 20% Mn is similar to the spectra of MnO_2 since the major fraction of manganese oxides in this catalyst is composed of MnO_2.

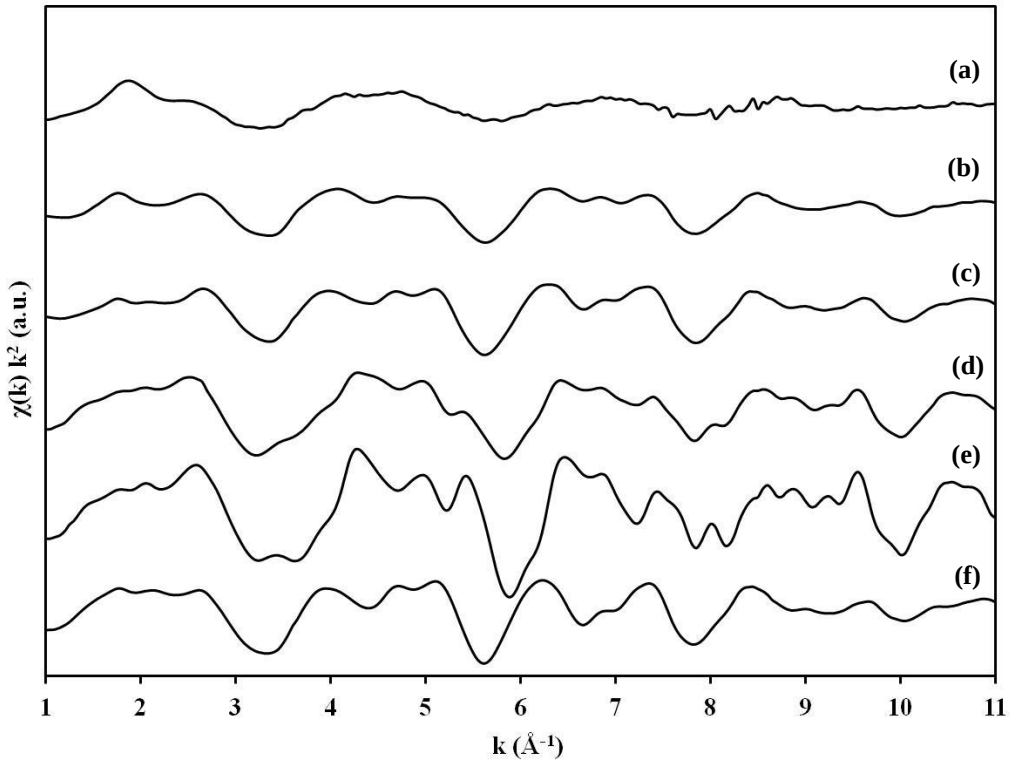

Fig. 5.9. Mn *K-edge* EXAFS spectra of the samples, (a) MnO_x/γ-alumina (1%), (b) MnO_x/γ-alumina (5%), (c), MnO_x/γ-alumina (10%), (d) MnO_x/γ-alumina (20%), (e) MnO_2, and (f) Mn_2O_3.

Using the model explained in section 5.2, S_o^2 of MnO_2 and Mn_2O_3 were estimated to be 0.68 and 0.85, respectively. The results of the EXAFS fitting of the catalysts are summarized in Table 5.6 by the averaging method. Fig. 5.10 and 5.11 depict the magnitude and the real part of the Fourier transform (FT) of Mn *K-edge* spectra of the catalysts, respectively. Fig. 5.10 and 5.11 also contain the magnitude and the real part of the FT of MnO_2 and Mn_2O_3 reference materials in order to provide a guideline for comparison between the catalysts and the reference materials.

Table 5.6. EXAFS fitting results of the catalysts by the averaging method

	Path	CN	σ^2 ($\times 10^{-3}$ Å^2)	R (Å)	E_o (eV)	R_f (%)
MnO_x/γ-alumina (1%)	Mn-O	1.7 ± 0.5	7.0 ± 1.6	1.886 ± 0.017	0.2 ± 1.6	0.9
	Mn-O	1.2 ± 0.2		1.985 ± 0.017		
	Mn-O	1.4 ± 0.3		2.236 ± 0.017		
	Mn-Mn	1.0 ± 0.5	17.4 ± 9.3	3.105 ± 0.026		
MnO_x/γ-alumina (5%)	Mn-O	1.7 ± 0.6	5.4 ± 1.8	1.904 ± 0.018	4.5 ± 1.1	2.4
	Mn-O	2.1 ± 0.5		1.990 ± 0.018		
	Mn-O	1.4 ± 0.1		2.254 ± 0.018		
	Mn-Mn	4.2 ± 1.2	10.5 ± 3.0	3.117 ± 0.014		
MnO_x/γ-alumina (10%)	Mn-O	1.7 ± 0.4	4.6 ± 1.6	1.894 ± 0.015	5.0 ± 0.9	1.6
	Mn-O	2.5 ± 0.5		1.985 ± 0.015		
	Mn-O	1.4 ± 0.1		2.249 ± 0.015		
	Mn-Mn	5.9 ± 1.1	9.6 ± 1.9	3.127 ± 0.011		
MnO_x/γ-alumina (20%)	Mn-O	3.5 ± 0.5	3.3 ± 1.3	1.884 ± 0.009	0.17 ± 1.4	1.5
	Mn-O	1.1 ± 0.1		1.970 ± 0.009		
	Mn-O	0.9 ± 0.1		2.234 ± 0.009		
	Mn-Mn	1.4 ± 0.2		2.882 ± 0.012		
	Mn-Mn	2.1 ± 0.1	4.7 ± 1.2	3.115 ± 0.012		
	Mn-Mn	4.0 ± 0.3		3.435 ± 0.012		

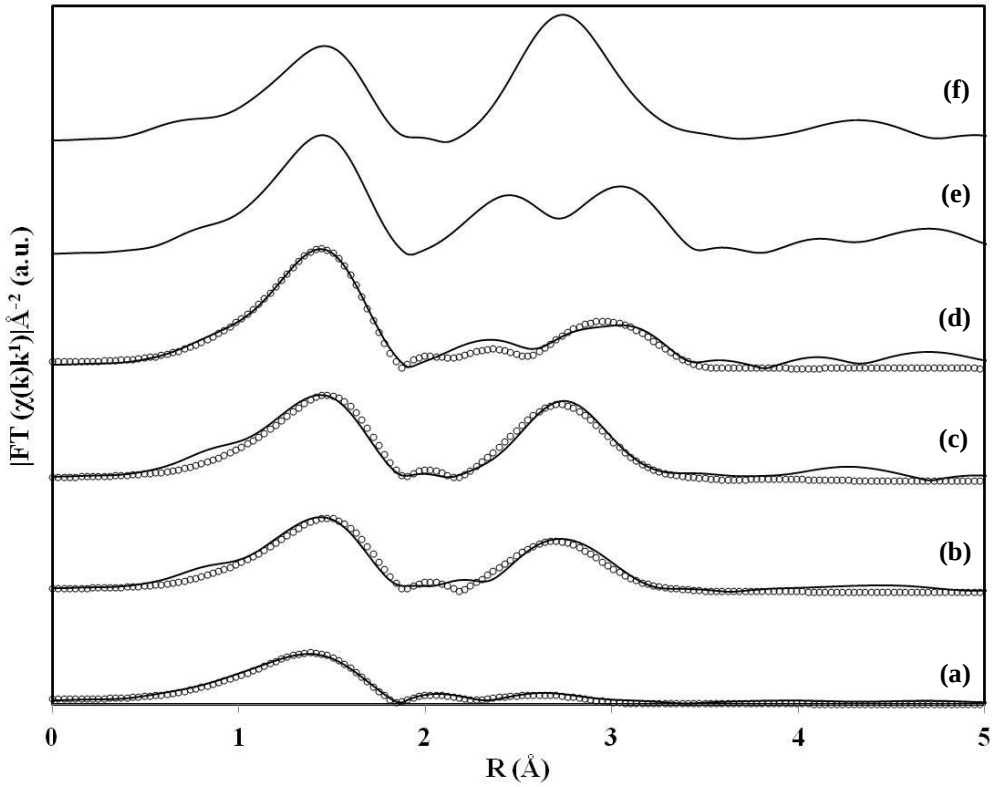

Fig. 5.10. Magnitude of the Fourier transform of Mn *K-edge* data (solid lines) and fitting (symbols), (a) MnO_x/γ-alumina (1%), (b) MnO_x/γ-alumina (5%), (c), MnO_x/γ-alumina (10%), (d) MnO_x/γ-alumina (20%), (e) MnO_2, and (f) Mn_2O_3.

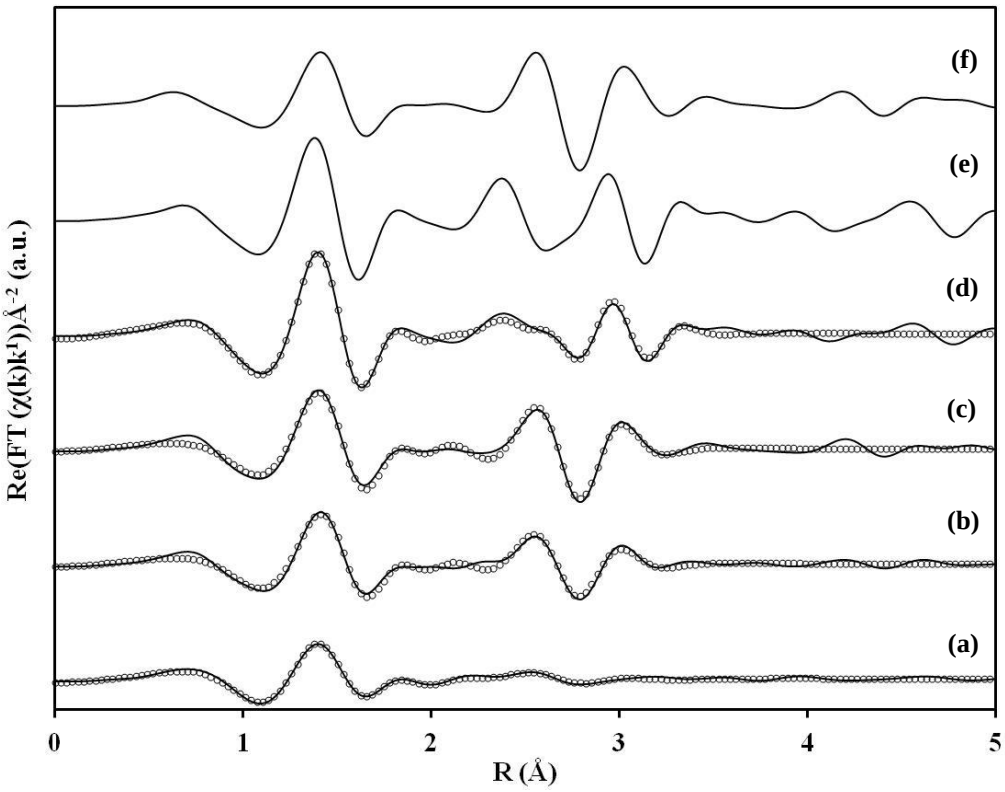

Fig. 5.11. Real part of the Fourier transform of Mn *K-edge* data (solid lines) and fitting (symbols), (a) MnO_x/γ-alumina (1%), (b) MnO_x/γ-alumina (5%), (c), MnO_x/γ-alumina (10%), (d) MnO_x/γ-alumina (20%), (e) MnO_2, and (f) Mn_2O_3.

Starting with MnO_x/γ-alumina (1%) in Table 5.6, it can be seen that CN of oxygen and manganese atoms at the first and second shells are smaller than the proposed model for Mn_2O_3 with one single site in Table 5.2. Low oxygen and manganese CNs can be observed by considering the magnitude and the real part of the FT of MnO_x/γ-alumina (1%) shown in Fig. 5.10 and Fig. 5.11, respectively. The FT magnitude and the real part of the first shell oxygen atoms are smaller than that of the catalysts with higher loadings. Mn also shows a very broad weak peak at the second shell of this catalyst, confirming the low CN of manganese.

By increasing the loading to 5%, oxygen CN at ca. 1.99 Å and manganese CN at ca. 3.11 Å increase to 2.1 and 4.2, respectively. Oxygen CNs are basically close to the values considered for Mn_2O_3 in Table 5.2 (1.5 at 1.899 Å, 3 at 1.987 Å and 1.5 at 2.248 Å) while Mn CN is smaller than 6 which is the expected CN of Mn at the second shell of Mn_2O_3 crystal.

Increasing loading to 10% does not significantly change oxygen CNs while it results in Mn CN of 5.9 which is very close to Mn CN in the second shell of Mn_2O_3. Fig. 5.10 (b) and 5.10 (c) also qualitatively show that the intensity of oxygen at the first shell remains unchanged by increasing the loading from 5% to 10%. However, Mn signal intensity increases at the second shell, implying higher CN of Mn in MnO_x/γ-alumina (10%) than MnO_x/γ-alumina (5%). It should be noted that the EXAFS of MnO_x/γ-alumina (10%) was modeled based on the structure of Mn_2O_3 and no contribution from MnO_2 is considered in the fitting of this catalyst. This is mainly because of the fact that only 9.0% of MnO_x is in the form of MnO_2 in MnO_x/γ-alumina (10%). This results in the EXAFS oscillation of this catalyst to be similar to that of Mn_2O_3 shown in Fig. 5.9, allowing fitting EXAFS of MnOx/γ-alumina (10%) by Mn_2O_3 structure.

In order to model the EXAFS spectra of the catalyst with 20% Mn loading which mostly contains MnO_2 (55.3%), two Mn backscattering atoms from MnO_2 at ca. 2.87 and 3.42 Å are added to the model in order to accommodate MnO_2 contributions. Comparing the common paths (Mn-O at ca. 1.90, 1.99, and 2.25 Å and Mn-Mn at ca. 3.11 Å) in MnO_x/γ-alumina (10%) and MnO_x/γ-alumina (20%), some changes can be seen in coordination numbers due to the coexistence of MnO_2 and Mn_2O_3. By increase of Mn loading from 10 to 20%, Oxygen CN at ca. 1.90 Å increases from 1.7 to 3.5. On the other hand, oxygen CNs of MnO_x/γ-alumina (20%) at ca. 1.99 and 2.25 Å are 1.1 and 0.9, respectively which are smaller than their corresponding values in MnO_x/γ-alumina (10%), i.e. 2.5 and 1.4 at ca. 1.99 and 2.25 Å, respectively. CN of Mn

at ca. 3.11 decreases from 5.9 in MnO_x/γ-alumina (10%) to 2.1 in MnO_x/γ-alumina (20%). In addition to these changes, two new manganese atoms were resolved at ca. 2.88 Å and 3.44 Å with CN of 1.4 and 4.0 which are the coordinates of manganese atoms in the structure of MnO_2.

If one makes an average over oxygen and manganese CNs based on the weight percent of MnO_2 (55.3%) and Mn_2O_3 (44.7%) in MnO_x/γ-alumina (20%) and uses CNs available in Table 5.1 and Table 5.2 for MnO_2 and Mn_2O_3 (with one single Mn site), a simplified model can be obtained for the catalysts with 20% Mn loading which is shown in Table 5.7. Based on this approach, one would expect 4.0, 1.4, and 0.7 oxygen atoms at ca. 1.90, 1.99, and 2.25 Å, respectively. In addition, this method results in 1.1, 2.7 and 4.4 of manganese atoms at ca. 2.87, 3.1,1 and 3.42 Å, respectively. It can be seen that the result of EXAFS fitting of MnO_x/γ-alumina (20%) reported in Table 5.6, follows the trend of CN changes shown in Table 5.7, implying that EXAFS fitting results are fairly reasonable.

Table. 5.7. Averaged coordination numbers of MnO_x/γ-alumina (20%)

Path	R_{reff} (Å)	Coordination number (CN)
Mn-O	1.892	4.0
Mn-O	1.987	1.4
Mn-O	2.248	0.7
Mn-Mn	2.871	1.1
Mn-Mn	3.112	2.7
Mn-Mn	3.424	4.4

R factors (R_f) reported in Table 5.6 represent the absolute percentage misfit between the data and theory. All fittings show low R_f values around 2% which shows that the models have been fitted closely to the EXAFS data.

5.4. Relationship between the structure and the activity of the catalysts

Four loadings of Mn (1, 5, 10, and 20%) are used for the oxidation of toluene by ozone at room temperature and higher temperatures up to 80 ^{o}C. 0.2 g of the catalysts is used to obtain the activities. Concentrations of toluene and ozone are 120 and 1050 ppm, respectively. The flow rates of toluene/nitrogen and ozone/oxygen streams are 400 and 600 ml min^{-1}, respectively. Toluene and ozone conversion at room temperature are shown in Fig. 5.12 and Fig. 5.13, respectively. It can be seen that the activity of the catalysts decreases with the increases of Mn loading. MnO_x/γ-alumina (1%) shows the highest activity followed by the catalysts with 5, 10 and 20% loadings. CO_x (CO and CO_2) are the major by-product of the reaction. All catalysts lose their activity during the reaction course in terms of toluene and ozone conversions in accordance with the activity of MnO_x/γ-alumina (10%) reported in Chapter 4. CHNS analysis is performed on the catalysts after running the reaction for 150 minutes at room temperature. The results, shown in Table 5.8, indicate that all the four catalysts gain considerable amount of carbon which can be considered as the reason for the catalyst deactivation. Table 5.8 also shows that the most active catalyst, MnO_x/γ-alumina (1%), gains higher carbon content than the other catalysts. The amount of accumulated carbon decreases with the increase of Mn loading in all catalysts. This trend can be explained with respect to the fact that the nature of the ongoing reaction at room temperature is mostly partial oxidation of toluene to carbonaceous compounds. Therefore, the catalysts with lower loading and higher activity produce more accumulated carbon species at room temperature.

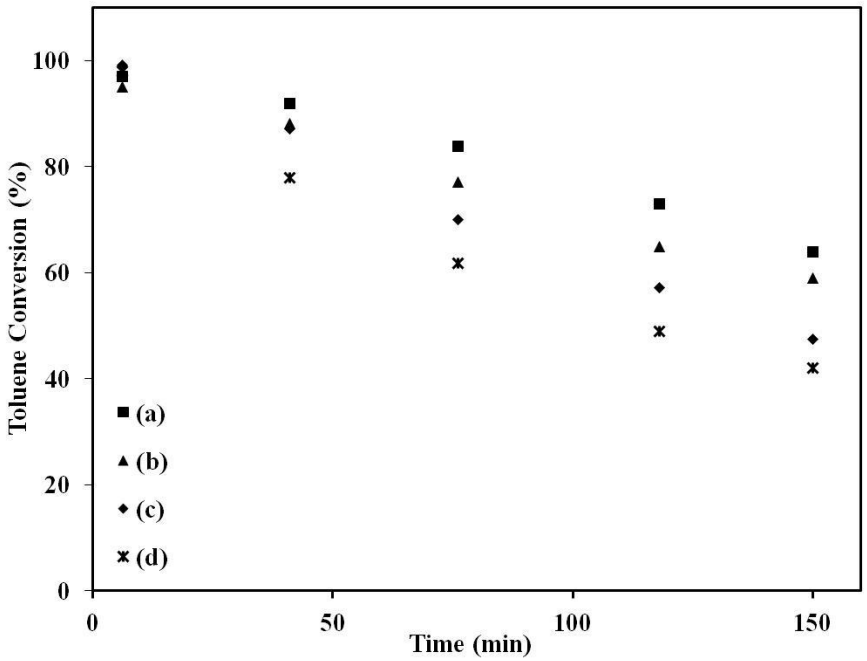

Fig. 5.12. Toluene conversion at room temperature, (a) MnO_x/γ-alumina (1%), (b) MnO_x/γ-alumina (5%), (c) MnO_x/γ-alumina (10%), and (d) MnO_x/γ-alumina (20%).

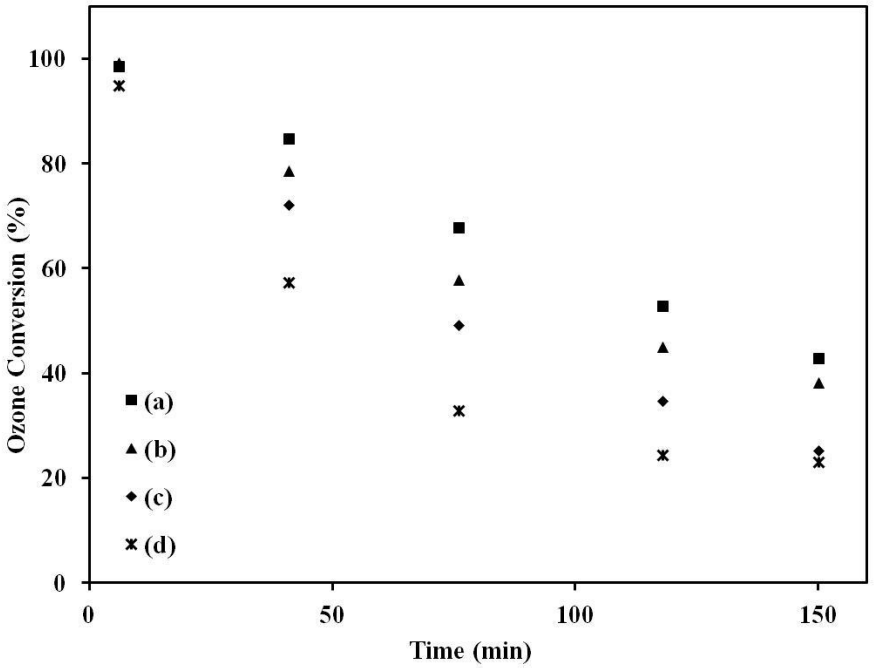

Fig. 5.13. Ozone conversion at room temperature, (a) MnO_x/γ-alumina (1%), (b) MnO_x/γ-alumina (5%), (c) MnO_x/γ-alumina (10%), and (d) MnO_x/γ-alumina (20%).

Table 5.8. Accumulated carbon content on the catalysts after 150 minutes reaction at room temperature

	MnO_x/γ-alumina (1%)	MnO_x/γ-alumina (5%)	MnO_x/γ-alumina (10%)	MnO_x/γ-alumina (20%)
Carbon content (wt%)	11.16	11.01	10.25	9.00

Fourier transform infer red (FT-IR) is used to study the surface of the deactivated catalysts. FT-IR spectra of fresh γ-alumina and the catalysts after 150 minutes of the reaction at room temperature are shown in Fig. 5.14.

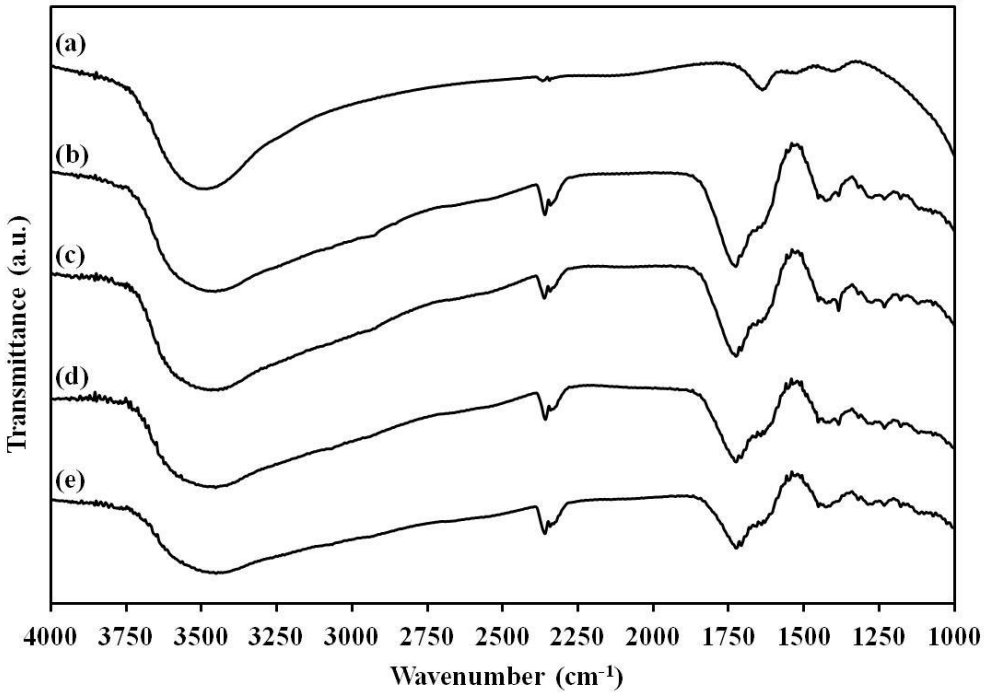

Fig. 5.14. FT-IR spectra of the deactivated catalysts, (a) fresh γ-alumina, (b) MnO_x/γ-alumina (1%), (c) MnO_x/γ-alumina (5%), (d) MnO_x/γ-alumina (10%), and (e) MnO_x/γ-alumina (20%).

Spectra of fresh γ-alumina not used in the reactor, Fig. 5.14 (a), show peaks at 1622, 2350 cm^{-1} and a broad signal between 2500 and 3800 cm^{-1} which are due to adsorbed water, CO_2, and hydroxyl groups on alumina, respectively. All the four catalysts show new bands at 1410 and 1718 cm^{-1} which are indicative of C-O-H bending of alcohols and carbonyl group (C=O) stretch of carboxylic acids, respectively [97]. In addition, a broad peak in the range 2500 to 3800 cm^{-1} is observed on all catalysts which can be due to the overlapping of OH stretching of carboxylic acids and alcohols with that of adsorbed water [6]. The intensity of these new peaks (1410, 1718, and 2500-3800 cm^{-1}) becomes smaller with the increase of Mn loading, implying that the amount of deposited alcohols and carboxylic acids has a reverse relationship with the manganese loading. This is also qualitatively in agreement with the result of CHNS analysis suggesting that the order of carbon content of the used catalysts has reverse relationship with the Mn loading. Acetic acid and oxalic acid, benzene, and maleic anhydride were identified as the minor by-products of the reaction in Chapter 3 [98]. The presence of acetic acid and oxalic acid also supports the identification of carboxylic acids on the catalysts at room temperature due to the incomplete oxidation of toluene.

Results (toluene and ozone conversion versus temperature) of high temperature activity of the catalysts up to 80 ^oC are shown in Fig. 5.15 and Fig. 5.16. Activity orders are similar to the room temperature activities, indicating that lower Mn loadings result in higher conversion of toluene and ozone. It can be seen that increasing the temperature from room temperature (22 ^oC) enhances toluene and ozone conversions up to 80 ^oC. All the four catalysts show the same activity at 80 ^oC, at which maximum conversion of toluene occurs. Increasing the temperature from 80 to 100 ^oC, data not shown, decreases toluene conversion to some extent while the conversion of ozone remains constant at 100%.

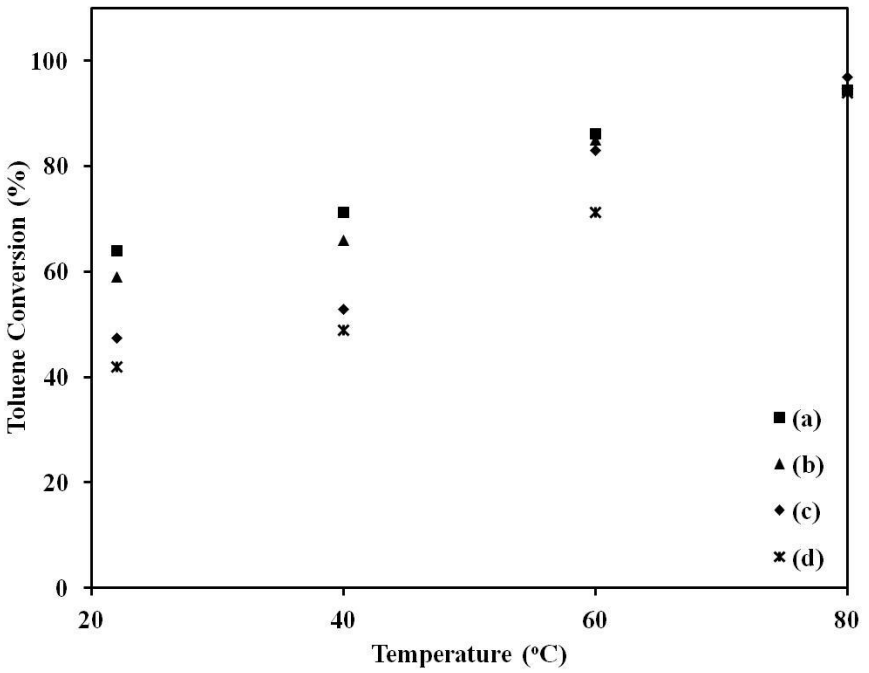

Fig. 5.15. Toluene conversion versus temperature, (a) MnO_x/γ-alumina (1%), (b) MnO_x/γ-alumina (5%), (c) MnO_x/γ-alumina (10%), and (d) MnO_x/γ-alumina (20%).

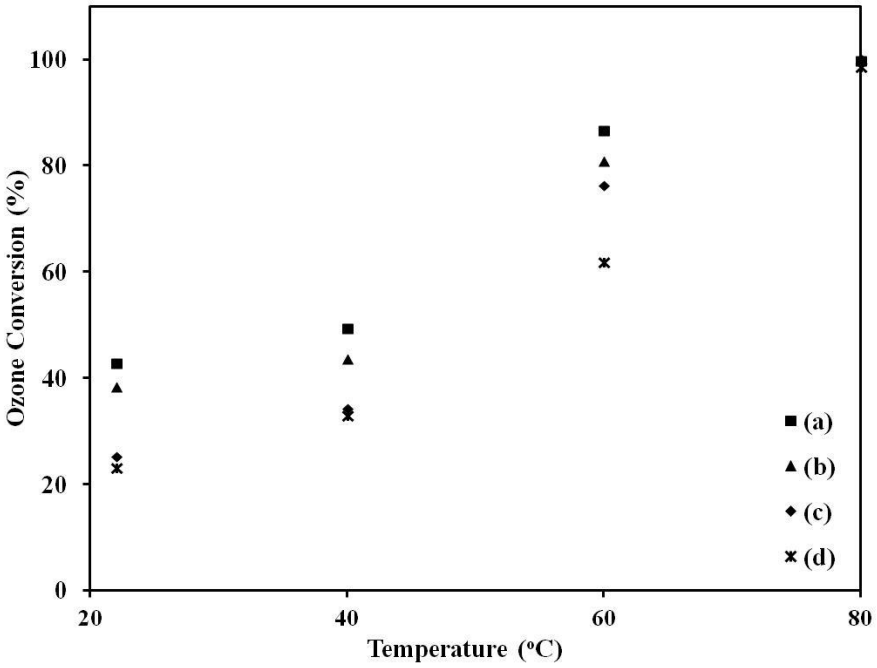

Fig. 5.16. Ozone conversion versus temperature, (a) MnO_x/γ-alumina (1%), (b) MnO_x/γ-alumina (5%), (c) MnO_x/γ-alumina (10%), and (d) MnO_x/γ-alumina (20%).

The overall observation of the activities at room and higher temperatures suggests that catalysts with lower Mn loadings are more active for the oxidation of toluene by ozone. Einaga et al. have studied the effect of Mn loading in the oxidation of benzene by ozone at room temperature over MnO_x/γ-alumina [55]. They reported that catalysts with lower loadings (1 to 7.5%) have slightly higher activities and isolated Mn atoms in lower loadings and aggregated Mn_3O_4 clusters in higher loadings (10 to 15%) show almost similar activities. On the other hand, Reed et al. have showed that higher loadings of Mn on silica result in higher oxidation rate of acetone by ozone [29]. They proposed that lower oxidation states of Mn and more adjacent Mn sites in catalysts with higher Mn loadings are two factors, controlling the rate of acetone oxidation by ozone. They have also mentioned that the rate controlling step of acetone ozonation is the oxidation of the catalyst by ozone and not the oxidation of acetone by the catalyst.

As it was mentioned in Chapter 2, the mechanism of oxidation of VOCs by ozone is based on ozone decomposition expressed by Eq. (5.17) to Eq. (5.19), generating atomic oxygen to react with adsorbed VOCs:

$$O_3 + Mn \rightarrow O_2 + O\text{-}Mn \quad (5.17)$$

$$O_3 + O\text{-}Mn \rightarrow O_2 + O_2\text{-}Mn \quad (5.18)$$

$$O_2\text{-}Mn \rightarrow O_2 + Mn \quad (5.19)$$

It is believed that higher dispersion of Mn atoms in catalysts with lower loading levels decreases the oxidation state of Mn. As the oxidation state of Mn decreases, the ability of Mn atoms in transferring electrons to ozone in Eq. (5.17) ($O_3 + Mn^{n+} \rightarrow O_2 + O^{2-} + Mn^{(n+2)+}$) increases, leading to faster decomposition rate of ozone to atomic oxygen and consequently higher rate of toluene oxidation. In fact, activity orders of the catalysts can be related to the

reverse of Mn *K-edge* absorption energy orders reported in Table 5.5. Einaga and Ogata also found that higher dispersion of Mn is more effective in benzene ozonation at room temperature [56] but it seems that changes in Mn oxidation state as the result of variation in Mn dispersion is controlling the rate of aromatics oxidation such as benzene and toluene by ozone.

5.5. Summary

The effect of manganese loading on the activity of MnO_x/γ-alumina was studied in this chapter. Four loadings of Mn (1, 5, 10, and 20%) were used to obtain the activity of the catalysts in the oxidation of toluene in the range of 22-100 ^oC. Characterization of the catalysts was performed by XRD, XANES, and EXAFS analysis in order to elucidate the relationship between the structure of manganese oxides and Mn loading. XRD analysis showed that Mn_2O_3 was the dominant phase at Mn loading up to 5%, whereas a mixture of MnO_2 and Mn_2O_3 was observed at higher catalyst loadings. The fraction of MnO_2 and the absorption energy of the catalysts increased with the increase of Mn loading. The catalyst with 10% Mn loading had 91.0% of Mn_2O_3 and 9.0% of MnO_2. On the other hand, the catalyst with 20% Mn loading contained 55.7% of MnO_2 and 44.7% of Mn_2O_3. The formal oxidation state of Mn in the catalysts with 1 and 5% Mn loading was less than that of Mn_2O_3 reference material due to the incomplete growth of Mn_2O_3 clusters. The oxidation state of MnO_x/γ-alumina (10%) was slightly higher than Mn_2O_3, showing the presence of MnO_2 in addition to Mn_2O_3 nano-particles. The catalyst with 20% loading of manganese had the same absorption energy as that of MnO_2, suggesting that the major component of this catalyst is MnO_2. EXAFS fitting was in agreement with the result of XRD and XANES, showing the growth of Mn_2O_3 particles by increasing the loading from 1 to 10%. EXAFS signals and coordination numbers were changed by further increase of the loading from 10 to 20% due to the formation of more MnO_2 phase.

Activity tests of the catalysts indicated that lower Mn loadings were more favorable in the oxidation of toluene up to 80^{o}C, at which the catalysts showed the same activity under the reaction conditions. All the catalysts became deactivated at room temperature due to the accumulation of alcohols and carboxylic acids on their surface indicated by CHNS and FT-IR analyses. It was suggested that activity orders of the catalysts could be related to the oxidation state of Mn on the catalyst. Catalysts with lower Mn loadings had higher activity in transferring electrons to ozone to initiate the ozone decomposition reaction due to their lower oxidation state. This increased the decomposition rate of ozone to atomic oxygen which consequently enhanced the oxidation rate of toluene.

CHAPTER 6
PROMOTIONAL EFFECT OF NOBLE METALS ON ACTIVITY OF MANGANESE OXIDES

It was discussed in Chapters 4 and 5 that manganese oxides are effective catalysts for low temperature oxidation of toluene. Toluene can be completely oxidized at around 80 ^{o}C in the presence of ozone and MnO_x dispersed on γ-alumina. One possible approach to increase the catalyst activity is to add promoters to manganese oxides. There are reports in the literature, showing that combination of transition metal oxides with noble metals can lead to a synergy in the activity of catalysts in the combustion of VOCs by oxygen. Andreeva et al. have shown that addition of gold improves the catalytic activity of vanadium oxides in the oxidation of benzene [99]. The activity of vanadium oxides was also promoted by palladium for benzene combustion by Garcia et al. [73]. Galvan and co-workers added palladium to alumina-supported manganese oxides to reduce the oxidation temperature of formaldehyde-methanol mixture [100-102]. Incorporation of small amounts of palladium improved the activity of manganese oxides, causing the oxidation of formaldehyde and methanol to occur at room temperature. Similar synergy was also observed between manganese and platinum in catalytic oxidation of toluene, n-hexane, and ethanol [72, 74, 103].

Even though the combination of transition metal oxides with noble metals has been studied in the oxidation of VOCs by oxygen, this issue has not been explored in catalytic oxidation of VOCs by ozone. The majority of researchers have focused on the ozonation of VOCs over transition metal oxides. Chapter 6 explores the effect of addition of Pt and Pd to Mn in order to enhance the activity of alumina-supported manganese oxides in catalytic ozonation of toluene. This chapter also aims to elaborate atomic interactions between the noble metals and

manganese oxides in order to relate the structure of the monometallic and bimetallic catalysts to the observed catalytic activities.

6.1. Characterization of monometallic and bimetallic catalysts

Platinum and palladium are the two noble metals studied in this chapter. The monometallic catalysts are called Pt/γ-alumina, Pd/γ-alumina, and MnO_x/γ-alumina for the catalysts containing Pt, Pd, and Mn, respectively. The bimetallic catalysts are prepared by the impregnation of the prepared MnO_x/γ-alumina with Pt and Pd. They are called Pt-MnO_x/γ-alumina and Pd-MnO_x/γ-alumina for Pt-Mn and Pd-Mn bimetallic catalysts, respectively. Loadings of Pt, Pd, and Mn are 1%, 1%, and 10%, respectively. Catalysts are characterized by X-ray diffraction (XRD), hydrogen temperature programmed reduction (H_2-TPR), and X-ray absorption spectroscopy (XAS) including XANES and EXAFS. XAS will be mainly used to clarify the atomic interactions between the noble metals and manganese oxides.

6.1.1. XRD and H_2-TPR

Fig. 6.1 presents the XRD spectra of different catalysts studied in this chapter. Fig. 6.1 (a) shows the diffractogram of MnO_2 (pyrolusite) and Mn_2O_3 (bixibyite) on MnO_x/γ-alumina as it was presented in Chapters 4 and 5. The addition of Pt and Pd to MnO_x/γ-alumina (Fig. 6.1 (b) and 6.1 (c)) does not change the XRD spectra of MnO_x/γ-alumina except for the appearance of a platinum peak at 2θ value of 39.8 degree in Fig. 6.1 (b). The same peak is also present in Fig 6.1 (d) which is the XRD of Pt/γ-alumina catalyst with the same loading. This suggests that Pt is likely present in metallic state in Pt-MnO_x/γ-alumina and Pt/γ-alumina catalysts. Fig. 6.1 (c) and (e) show no distinct peaks for Pd or PdO, suggesting high dispersion of palladium species on Pd-MnO_x/γ-alumina and Pd/γ-alumina.

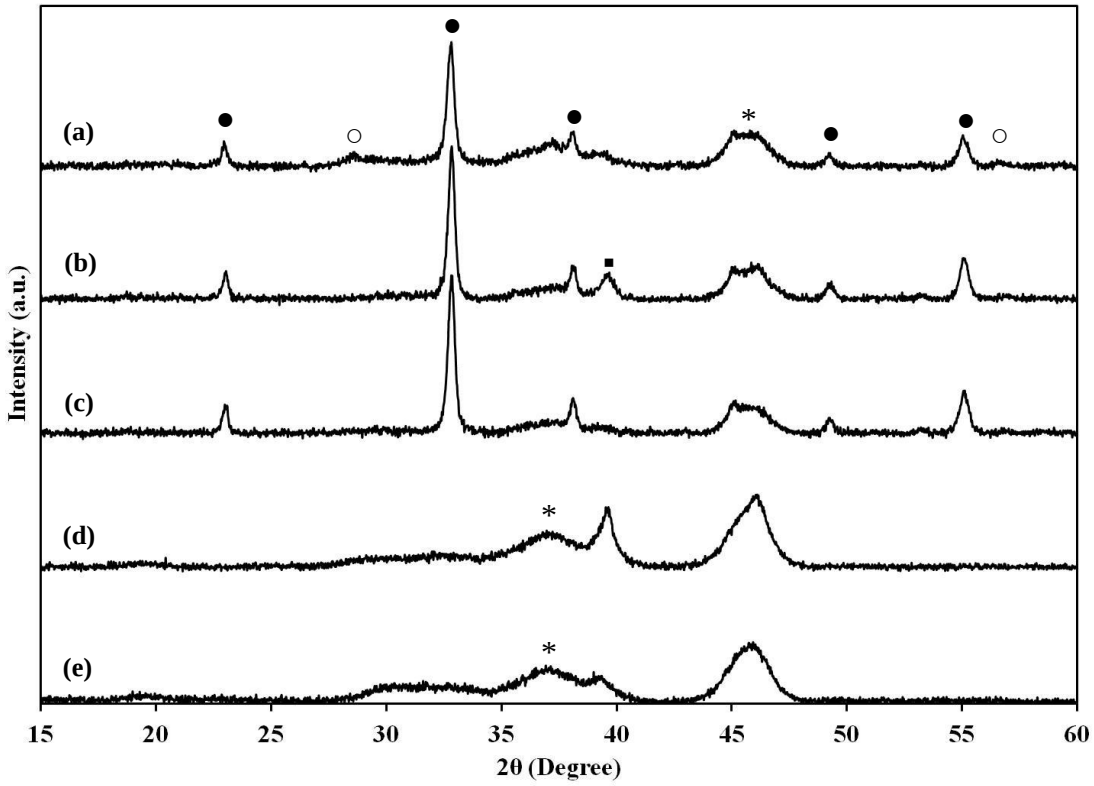

Fig. 6.1. XRD spectra of the catalysts, (a) MnO_x/γ-alumina, (b) Pt-MnO_x/γ-alumina, (c) Pd-MnO_x/γ-alumina, (d) Pt/γ-alumina, and (e) Pd/γ-alumina, *: γ-alumina, ▪: Pt, ○: MnO_2, ●: Mn_2O_3.

H_2-TPR of the catalysts is shown in Fig. 6.2. TPR Profile of Pt/γ-alumina, shown in Fig. 6.2 (a), does not show any distinct reduction peak which is likely due to the presence of metallic platinum on the catalyst surface. Fig. 6.2 (b) shows a small broad peak for the alumina-supported palladium catalyst at 121 ^oC. This implies that palladium oxide species are present on γ-alumina, resulting in a broad and weak reduction peak at 121 ^oC. TPR pattern of MnO_x/γ-alumina catalyst is indicated in Fig. 6.2 (c) with two main peaks at 394 and 508 ^oC along with a smaller one at

423 °C. The first peak at 394 °C is attributed to the reduction of MnO_2 and Mn_2O_3 to Mn_3O_4 through the sequence of $MnO_2 \rightarrow Mn_2O_3 \rightarrow Mn_3O_4$ [102, 104]. The second and third peaks at 394 and 508 °C are related to the reduction of small and large particles of Mn_3O_4 to MnO, respectively. [102].TPR of the bimetallic catalysts are depicted in Fig. 6.2 (d) and (e). Addition of platinum and palladium to MnO_x/γ-alumina greatly reduces the reduction temperature of MnO_x and causes the total reduction of MnO_x (MnO_2 and Mn_2O_3 to MnO) to take place at 134 °C in one step. This phenomenon can be explained by the spillover effect of hydrogen from noble metals to manganese oxides, facilitating the reduction reaction at low temperatures [104, 105].

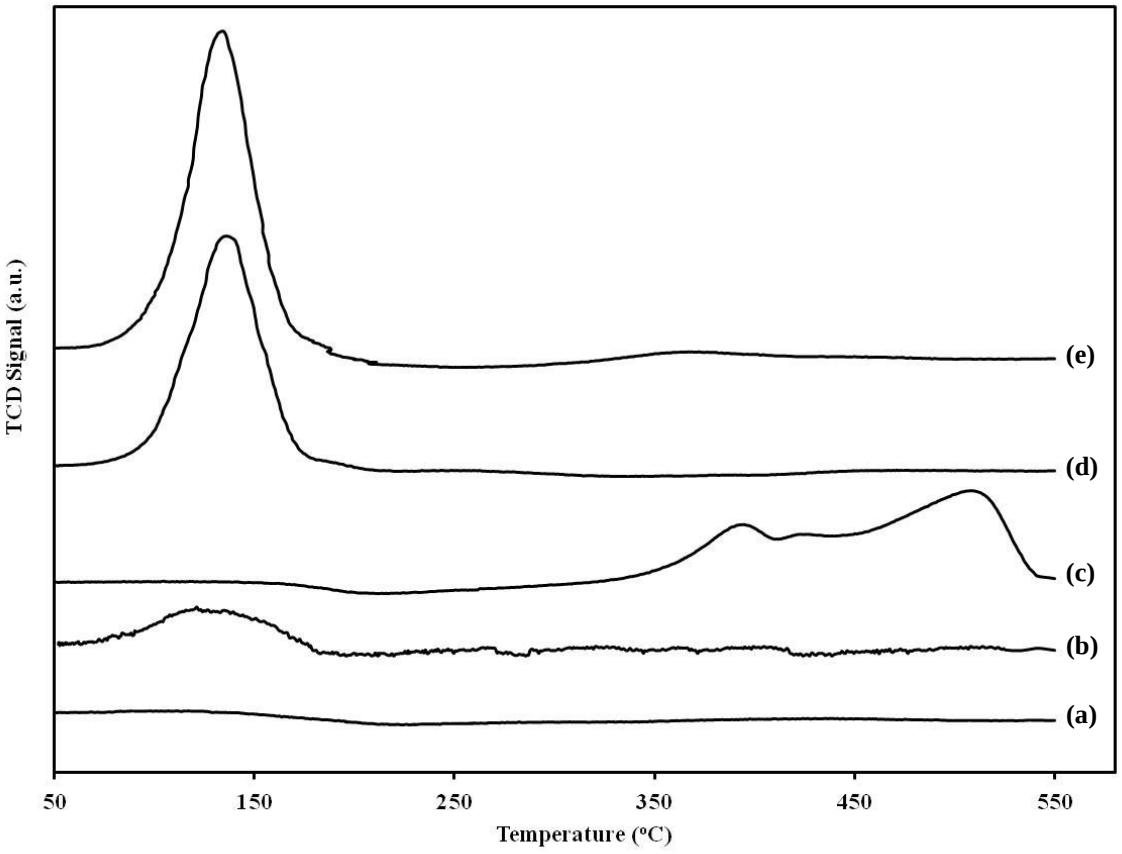

Fig. 6.2. H_2-TPR of the catalysts, (a) Pt/γ-alumina, (b) Pd/γ-alumina (4 times zoomed), (c) MnO_x/γ-alumina, (d) Pt-MnO_x/γ-alumina, and (e) Pd-MnO_x/γ-alumina.

6.1.2. XANES and EXAFS analysis

Results of X-ray absorption spectroscopy (XAS) are explained in order to develop a better understanding about atomic interactions between Mn and Pd or Pd in the bimetallic catalysts. XANES analysis is presented quantitatively while EXAFS analysis is demonstrated qualitatively as the magnitude of Fourier transforms.

Pd *K-edge* normalized XANES spectra are shown in Fig. 6.3, in which an absorption edge occurs due to 1s to 5p dipole-allowed excitation. Pd/γ-alumina and Pd-MnO_x/γ-alumina catalysts have the same edge shape with the absorption edge of 24354.0 eV, which is 4.0 eV higher than the edge energy of Pd foil at 24350.0 eV. This value is the same as the absorption energy reported for PdO [106], suggesting that Pd exists in the form of PdO. Fourier transformed EXAFS spectra of Pd/γ-alumina and Pd-MnO_x/γ-alumina are included in Fig. 6.4. The Fourier transform is taken in the range of 2-14 $Å^{-1}$. The first peak at ca. 1.55 Å corresponds to Pd-O backscattering in Pd/γ-alumina and Pd-MnO_x/γ-alumina [106, 107]. No Pd-Pd peak was observed for either of the catalysts. This is due to the high dispersion of Pd on these catalysts, implying that Pd is most likely in amorphous form. The Pd-O peak in Pd/γ-alumina and Pd-MnO_x/ γ-alumina is the same in terms of shape and intensity, showing that the oxidation state and the first shell nearest neighbor coordination of Pd do not change in the presence of manganese oxides.

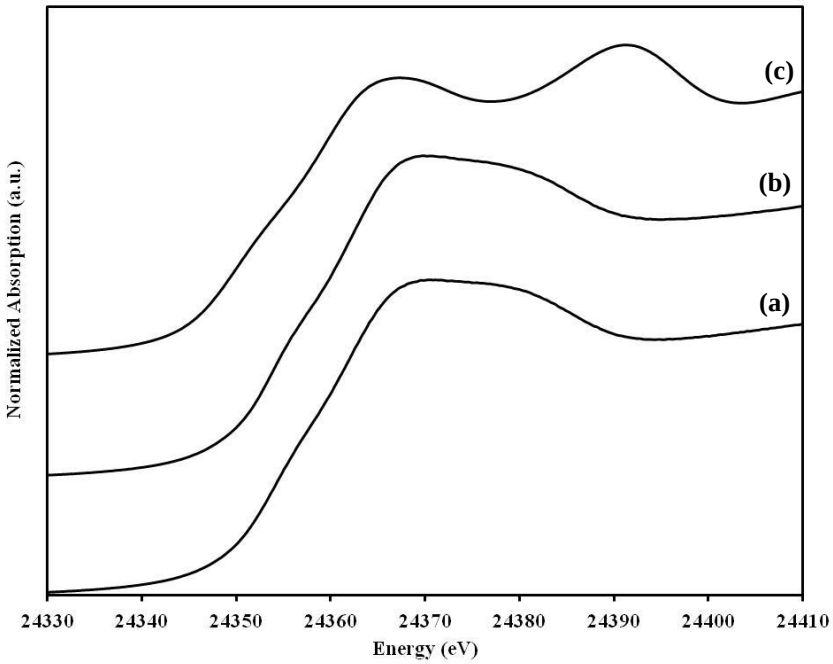

Fig. 6.3. Pd *K-edge* XANES spectra, (a) Pd/γ-alumina, (b) Pd-MnO_x/γ-alumina, and (c) Pd foil.

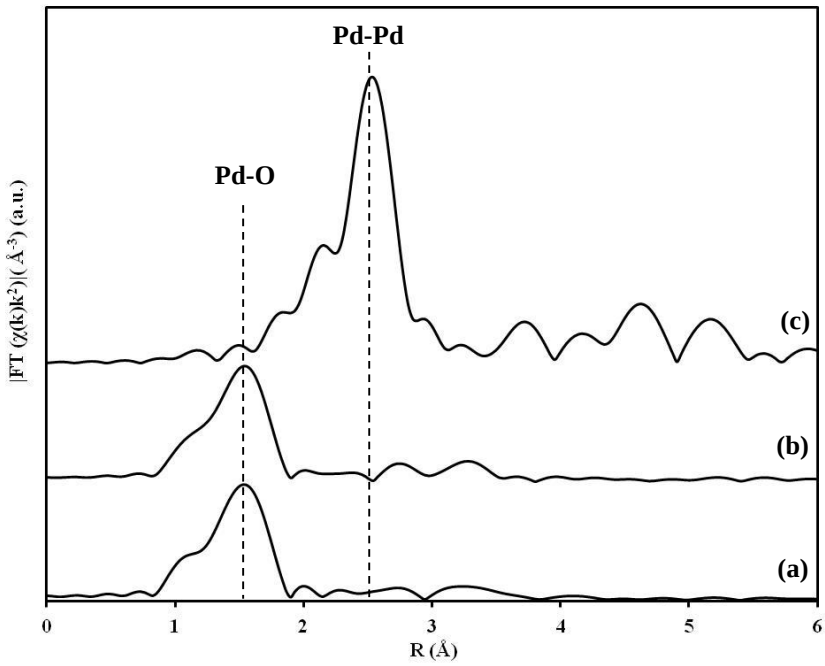

Fig. 6.4. Magnitude of the Fourier transform of Pd *K-edge*, (a) Pd/γ-alumina, (b) Pd-MnO_x/γ-alumina, and (c) Pd foil.

Fig. 6.5 shows XANES spectra of Pt *L_{III}-edge* of the reference materials (Pt foil and α-PtO_2) and Pt containing catalysts. Pt foil does not show an intense white line due to filled d orbital of Pt ($5d^9\ 6s^1$). On the other hand, α-PtO_2 with vacancies in the d orbital ($5d^6\ 6s^0$) has a sharp white line due to $2p_{3/2}$ to $5d_{3/2}$ and $5d_{5/2}$ excitations. It can be seen that the white line intensity of Pt/γ-alumina is higher than that of Pt foil, indicating the presence of platinum oxide species on alumina. The white line intensity of Pt *L_{III}-edge* is even higher in the presence of manganese oxide, indicating the presence of more Pt oxide species in Pt-MnO_x/γ-alumina than Pt/γ-alumina. Pt *L_{III}-edge* absorption energy is 11564.5 and 11565.1 eV for Pt/γ-alumina and Pt-MnO_x/γ-alumina, respectively. These absorption energies are 0.5 and 1.1 eV higher than the absorption energy of Pt foil at 11564.0 eV.

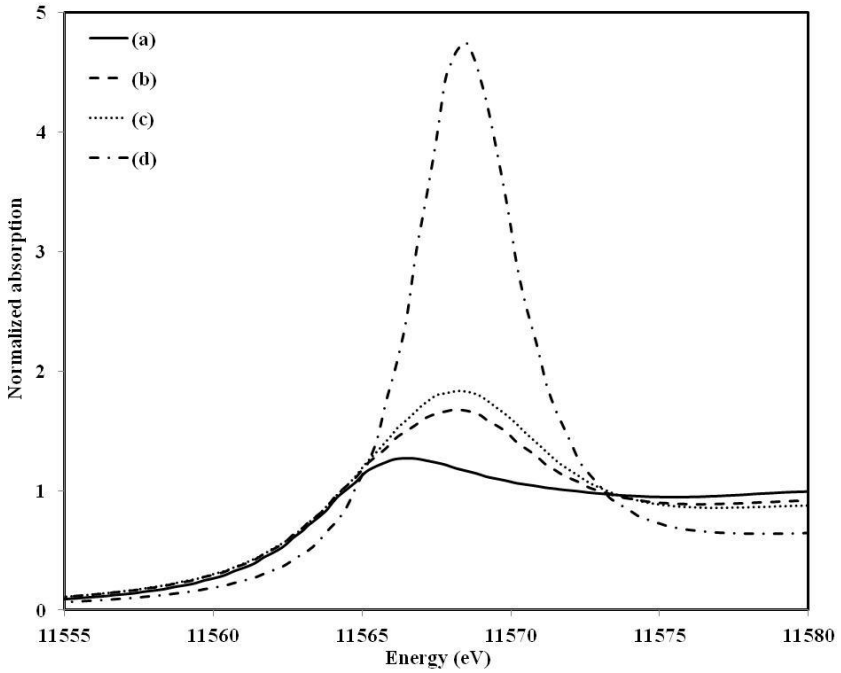

Fig. 6.5. Pt *L_{III}-edge* XANES spectra, (a) Pt foil, (b) Pt/γ-alumina, (c) Pt-MnO_x/γ-alumina, and (d) α-PtO_2.

Using linear combination fitting with Pt foil and α-PtO_2 reference materials, it can be found that 84.4% of Pt exists in metallic form and 15.6% of Pt is in +4 oxidation state on Pt/γ-alumina. Addition of Pt to manganese causes the fraction of metallic Pt to drop to 78.7% while the fraction of Pt^{4+} increases to 21.3%. This shows that the presence of manganese oxides increases the portion of Pt oxide species when Pt is added to MnO_x/γ-alumina instead of γ-alumina. Fig. 6.6 shows the magnitude of Fourier transforms of Pt L_{III}-*edge* EXAFS of Pt containing catalysts and the Pt reference materials. The Fourier transform is taken in the range of 2-14 $Å^{-1}$. Basically, the results of XANES study are in agreement with the EXAFS of Pt. It can be seen that the addition of platinum to MnOx/γ-alumina reduces the intensity of Pt-Pt peak at ca. 2.70 Å, which mostly corresponds to lower Pt-Pt coordination number (CN). But Pt-O signal at ca. 1.62 Å increases, implying higher Pt-O CN in Pt-MnO_x/γ-alumina. Decrease in Pt CN and increase in the first shell oxygen CN after the addition of Pt to MnO_x/γ-alumina indicate higher dispersion of Pt in the presence of Mn, leading to the attachment of some portion of Pt to manganese oxide clusters. The percent of the attached platinum to MnO_x is estimated to be at least 5.7% which is the difference between the percent of platinum oxides in Pt/γ-alumina (15.6%) and Pt-MnO_x/γ-alumina (21.3%) quantified by XANES.

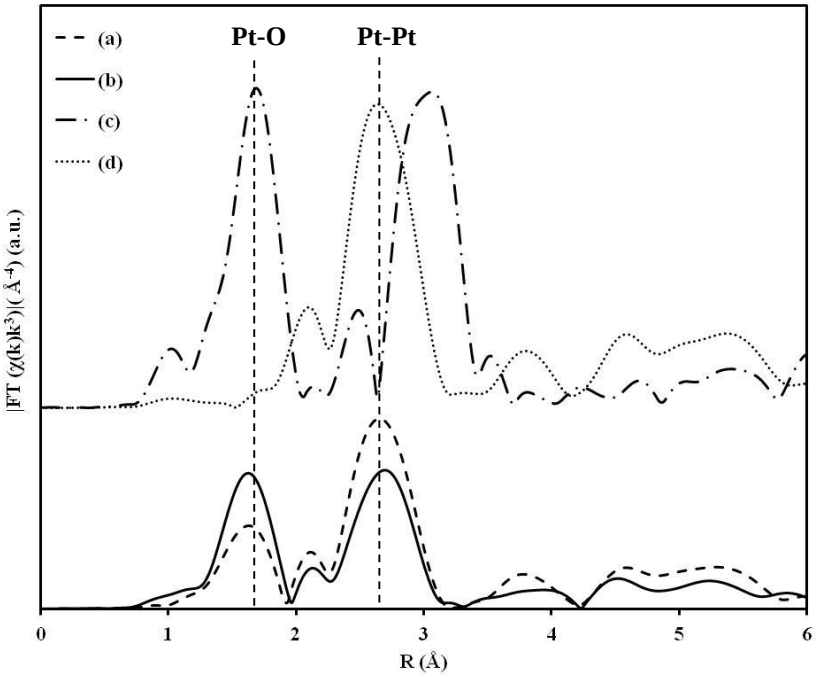

Fig. 6.6. Magnitude of the Fourier transform of Pt *L_{III}-edge*, (a) Pt/γ-alumina, (b) Pt-MnO_x/γ-alumina, (c) α-PtO_2, and (d) Pt foil.

It is clear in Fig. 6.5 and 6.6 that platinum oxide species are present on alumina while they are not detectable by H_2-TPR and XRD techniques. This indicates that in addition to metallic platinum particles on alumina, platinum oxide species are most likely present as small particles with size of less than 5 nm since there is no platinum oxide peaks in XRD of Pt/γ-alumina and Pt-MnO_x/γ-alumina. It also suggests that these small platinum species have a strong interaction with alumina, resulting in no H_2 reduction peak for Pt/γ-alumina in Fig. 6.2. This structural model for Pt on alumina is also in agreement with the work of Pan and Cowley and Schneider et al., in which they have observed the presence of separate metallic Pt and Pt oxide particles on alumina [108, 109].

Fig. 6.7 shows the near edge spectra of MnO_x/γ-alumina, Pt-MnO_x/γ-alumina, Pd-MnO_x/γ-alumina, and Mn_2O_3 reference material. Even though the addition of noble metals

causes a small increase in the white line area of MnO_x/γ-alumina, no changes are observed in the absorption energy of MnO_x/γ-alumina after the addition of noble metals. Basically, MnO_x/γ-alumina, Pt-MnO_x/γ-alumina, and Pd-MnO_x/γ-alumina have the same absorption energies at 6548.4 eV which is 0.3 eV higher than that of Mn_2O_3 at 6548.1 eV.

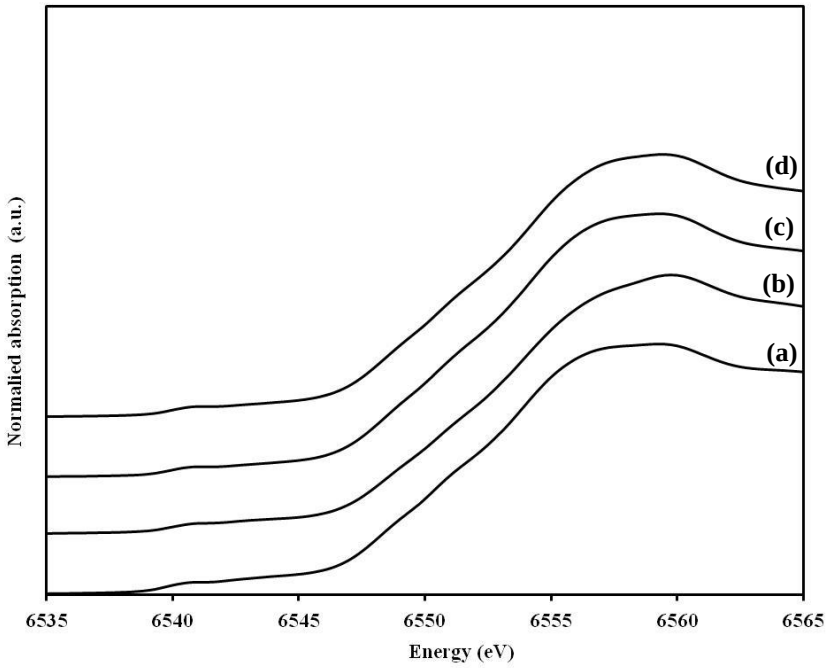

Fig. 6.7. Mn *K-edge* XANES spectra, (a) Mn_2O_3, (b) MnO_x/γ-alumina, (c) Pd-MnO_x/γ-alumina, and (d) Pt-MnO_x/γ-alumina.

Fig 6.8 shows the magnitude of Fourier transforms of Mn *K-edge*. The Fourier transform is taken in the range of 2-14 $Å^{-1}$. EXAFS peak locations of MnO_x/γ-alumina (Fig. 6.8 (b)), Pd-MnO_x/γ-alumina (Fig. 6.8 (c)), and Pt-MnO_x/γ-alumina (Fig. 6.8 (d)) are similar to that of Mn_2O_3 (Fig. 6.8 (a)) since 91.0% of manganese oxides have Mn_2O_3 structure determined in Chapter 4. It can be seen that signal intensities of Mn-O peak at ca. 1.47 Å and Mn-Mn peak at ca. 2.73 Å are similar in MnO_x/γ-alumina and Pd-MnO_x/γ-alumina, whereas an increase in Mn-Mn signal is

observed in Pt-MnO_x/γ-alumina by comparing Fig. 6.8 (b) and Fig. 6.8 (d). This shows that Mn coordination number (CN) slightly increases as the result of atomic interaction between Pt and manganese oxides clusters on alumina. On the other hand, Mn-Mn signal at 2.73 Å remains unchanged in the presence of Pd, showing that Mn and Pd do not have atomic interaction.

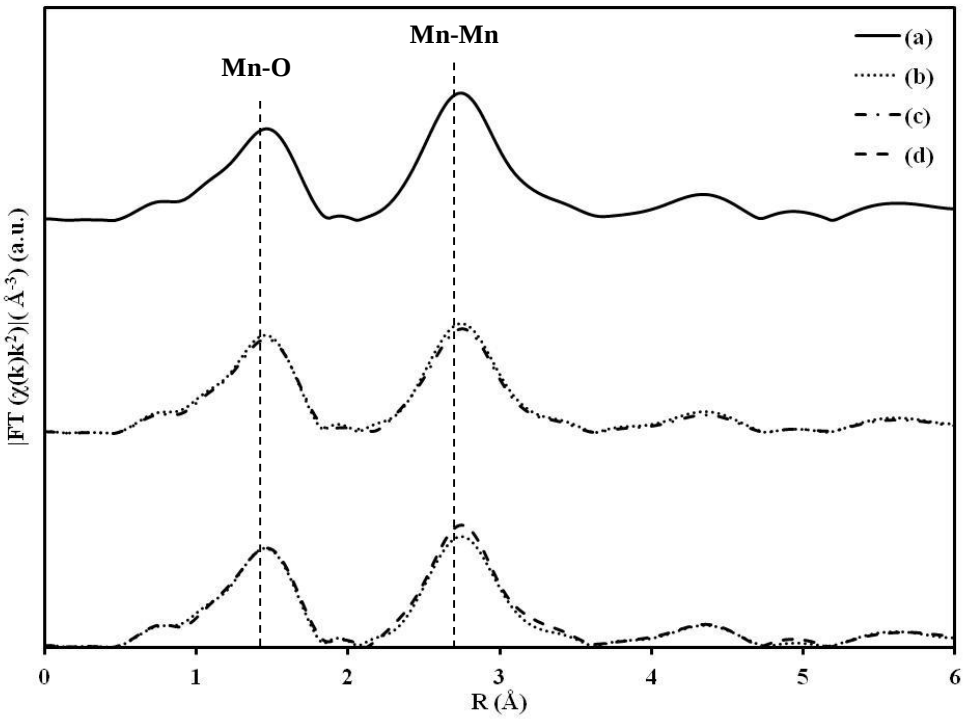

Fig. 6.8. Magnitude of the Fourier transform of Mn *K-edge*, (a) Mn_2O_3, (b) MnO_x/γ-alumina, (c) Pd-MnO_x/γ-alumina, and (d) Pt-MnO_x/γ-alumina.

Table 6.1 presents a summary of the absorption energies determined in this work by XANES analysis while Table 6.2 gives X-ray photoelectron spectroscopy (XPS) binding energies of similar bimetallic systems reported in the literature in order to compare the results obtained by XANES in this work (Table 6.1) with the other reports (Table 6.2). It can be seen in Table 6.2 that binding energies of Mn $2p_{1/2}$ and Mn $2p_{3/2}$ are more or less constant in the

presence or absence of noble metals. Pd is essentially in oxide form regardless of the fact that it is alone or it coexists with manganese on the support. Pt is slightly oxidized in Pt/γ-alumina and its degree of oxidation increases when manganese is present in the system. Therefore, by comparing the absorption energies of the monometallic and bimetallic catalysts given in Tables 6.1 and 6.2, one can conclude that electronic interactions found by XANES is consistent with those obtained by an alternative approach such as XPS.

Table 6.1. Summary of Mn, Pd and Pt absorption energies determined by XANES

Manganese samples	Mn *K-edge* E_0 (eV)	Palladium samples	Pd *K-edge* E_0 (eV)	Platinum samples	Pt L_{III}-*edge* E_0 (eV)
Mn	6539.0	Pd	24350.0	Pt	11564.0
Mn_2O_3	6548.1	PdO [106]	24354.0	PtO_2	11566.7
MnO_2	6552.7	Pd/ γ-alumina	24354.0	Pt/ γ-alumina	11564.5
MnO_x/γ-alumina	6548.4	Pd- MnO_x/γ-alumina	24354.0	Pt- MnO_x/γ-alumina	11565.1
Pd- MnO_x/γ-alumina	6548.4				
Pt- MnO_x/γ-alumina	6548.4				

Table 6.2. XPS binding energies (BE) of the similar bimetallic catalytic systems reported in literature

Catalytic system		Mn $2p_{1/2}$ (L_{II})	Mn $2p_{3/2}$ (L_{III})	Pt $4d_{5/2}$ (N_5)	Pd $3d_{5/2}$ (M_5)
		BE (eV)	BE (eV)	BE (eV)	BE (eV)
[104]	Mn/alumina		642.8	-	
	Pt/alumina		-	316.2	
	Pt-Mn/alumina		642.7	317.8	
[74]	Mn/alumina	654.0	642.4	-	
	Pt/alumina	-	-	315.4	
	Pt-Mn/alumina	654.3	642.5	317.0	
[101, 102, 110]	Mn/alumina		641.7		-
	Pd/alumina		-		336.6, 336.7
	Pd-Mn/alumina		641.7 to 641.9		336.5 to 336.8

It is also important to explain the reason why palladium tends to be in oxide form while the majority of platinum is in metallic state on γ-alumina. This relates to the decomposition temperature of palladium and platinum oxides which are as follows: PtO (325 ^{o}C), PtO_2 (450 ^{o}C), PdO (750 ^{o}C), and PdO_2 (200 ^{o}C) [111]. The calcinations temperature of the noble metal containing catalysts is 550 ^{o}C. Therefore, Pd exists as PdO while Pt is mostly in metallic state even though a small portion of Pt is in oxide form as it was revealed by XAS.

6.2. Activity of monometallic and bimetallic catalysts

Catalytic activities of monometallic and bimetallic catalysts at room temperature are shown in Fig. 6.9 and 6.10 in terms of toluene and ozone conversions, respectively. It can be seen in Fig. 6.9 that the activity of the catalysts for the oxidation of toluene by ozone is in the following order: Pt-MnO_x/γ-alumina (Fig. 6.9 (b)) > Pd-MnO_x/ γ-alumina (Fig. 6.9 (c)) ≈ MnO_x/ γ-alumina (Fig. 6.9 (a)) > Pd/ γ-alumina (Fig. 6.9 (e)) > Pt/ γ-alumina (Fig. 6.9 (d)). All catalysts lose their activity at room temperature due to the accumulation of carbonaceous species. The same trend of activity order and deactivation behavior is also seen for ozone conversion in Fig. 6.10.

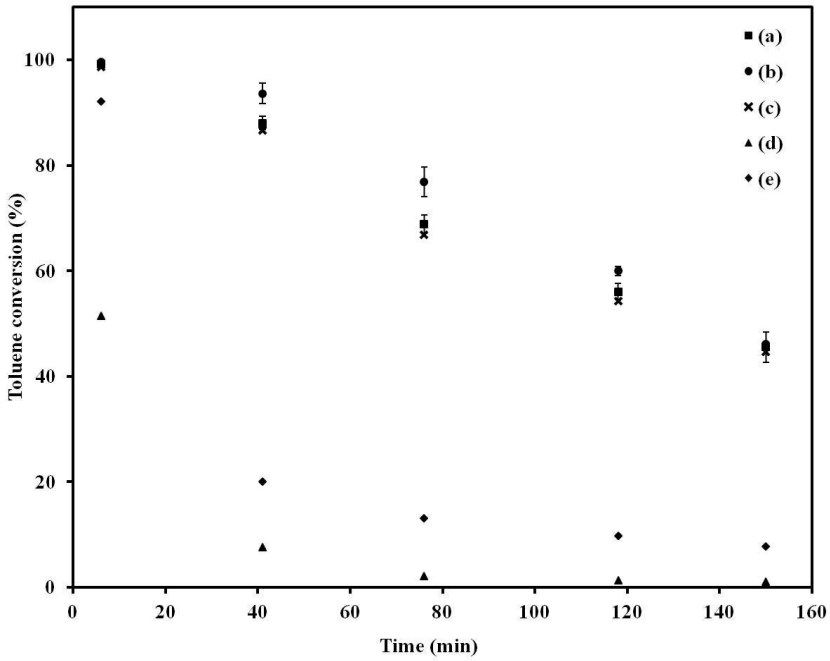

Fig. 6.9. Toluene conversion at room temperature, (a) MnO_x/γ-alumina, (b) Pt-MnO_x/γ-alumina, (c) Pd- MnO_x /γ-alumina, (d) Pt/γ-alumina, and (e) Pd/γ-alumina. Error bars are standard deviations.

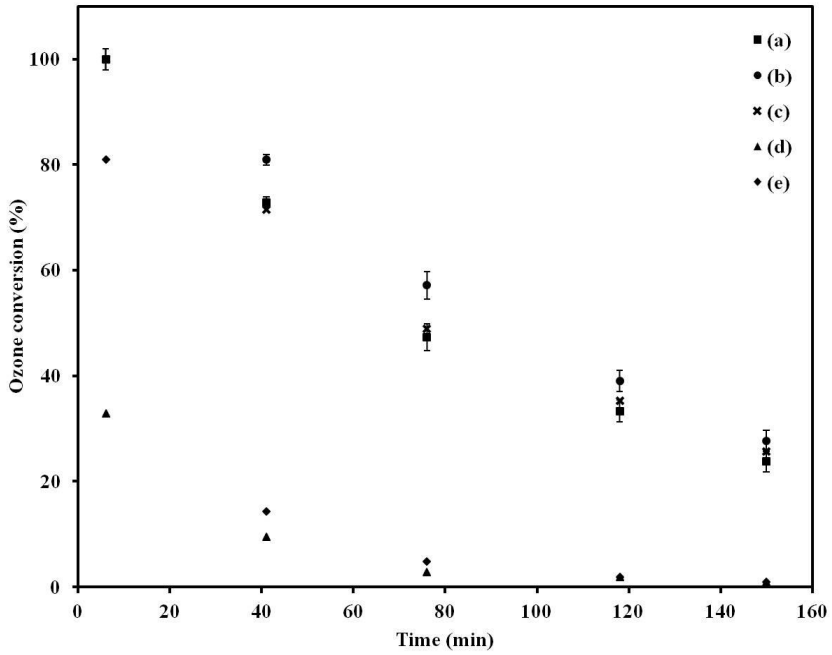

Fig. 6.10. Ozone conversion at room temperature, (a) MnO_x/γ-alumina, (b) Pt-MnO_x/γ-alumina, (c) Pd- MnO_x /γ-alumina, (d) Pt/γ-alumina, (e) Pd/γ-alumina. Error bars are standard deviations.

The activity of the catalysts at higher temperatures of 40, 60, 70, 80, and 100 ^oC is presented in Fig. 6.11 and 6.12. Increase of the reaction temperature improves toluene conversion and prevents the deactivation of the catalysts. Pt-MnO_x/γ-alumina (Fig. 6.11 (b) has the highest toluene conversion while Pd-MnO_x/γ-alumina (Fig. 6.11 (c)) and MnO_x/γ-alumina (Fig. 6.11 (a)) have almost the same activity. Pd-MnO_x/γ-alumina and MnO_x/γ-alumina catalysts result in maximum conversion of toluene at 80 ^oC, after which their activities drop slightly. But complete conversion of toluene is possible at 70 ^oC with Pt-MnO_x/γ-alumina. This temperature is 10 ^oC lower than the reaction temperature of Pd-MnO_x/γ-alumina and MnO_x/γ-alumina for the total oxidation of toluene. Pd/γ-alumina (Fig. 6.11 (e)) shows higher activity than Pt/γ-alumina (Fig. 6.11 (d)) but manganese containing catalysts are more effective than Pd/γ-alumina and Pt/γ-alumina.

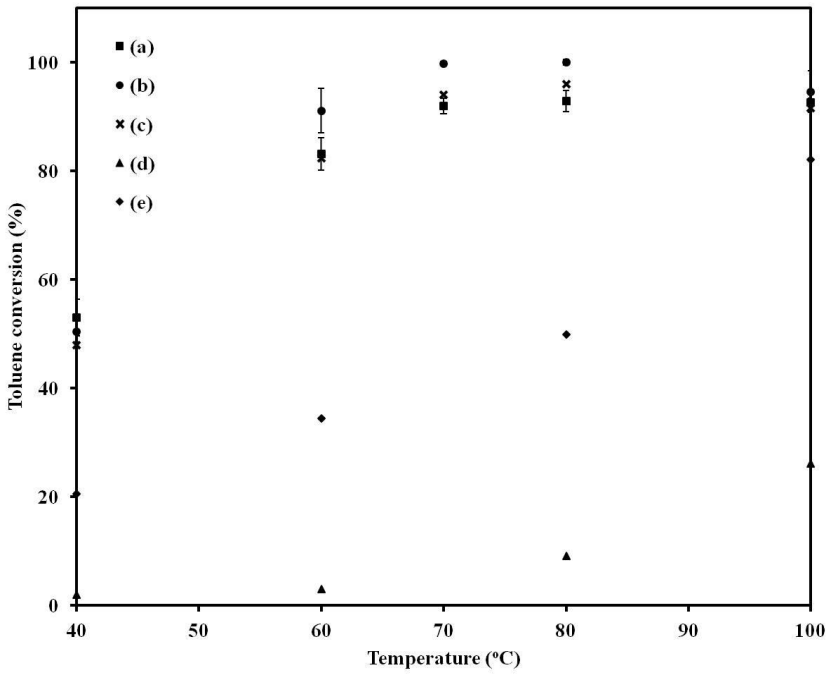

Fig. 6.11. Toluene conversion above room temperature, (a) MnO_x/γ-alumina, (b) Pt-MnO_x/γ-alumina, (c) Pd- MnO_x /γ-alumina, (d) Pt/γ-alumina, and (e) Pd/γ-alumina. Error bars are standard deviations.

Ozone conversion of the catalysts is shown in Fig. 6.12, in which the activity order of the catalysts is the same as that of toluene conversion. Ozone conversion increases in manganese containing catalysts with the increase of temperature and reaches almost 100% at 80 °C. The plateau in toluene conversion above 80 °C for Pt-MnO_x/γ-alumina, Pd-MnO_x/γ-alumina, and MnO_x/γ-alumina is related to the complete consumption of ozone at 80 °C. Increasing the reaction temperature from 80 °C to 100 °C does not increase the toluene conversion since all ozone is already consumed at 80 °C.

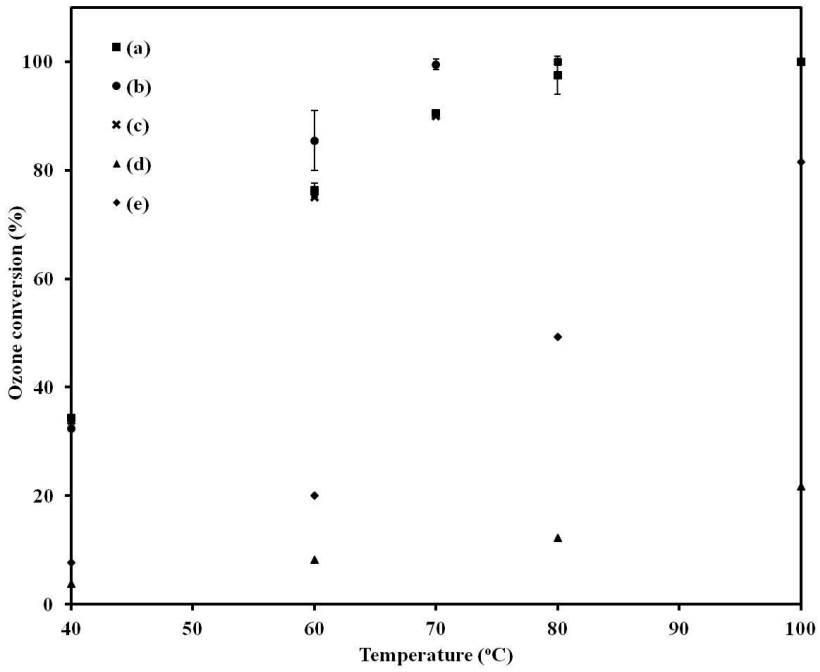

Fig. 6.12. Ozone conversion above room temperature, (a) MnO_x/γ-alumina, (b) Pt-MnO_x/γ-alumina, (c) Pd- MnO_x /γ-alumina, (d) Pt/γ-alumina, and (e) Pd/γ-alumina. Error bars are standard deviations.

From the results discussed on Fig. 6.9 to Fig. 6.12, it can be seen that the addition of platinum to manganese enhances the activity of MnO_x/γ-alumina, while Pd does not have any effect on the performance of MnO_x/γ-alumina. This result can be explained by XANES and EXAFS studies of Pt-MnO_x/γ-alumina and Pd-MnO_x/γ-alumina catalysts. Basically, the fraction of Pt oxide species and Pt atomic environment change when Pt coexists with Mn while such changes are not found in the case of Pd. This means that Pt can interact with manganese oxides to improve Mn activity while Pd does not have this capability. Most probably Pd is mainly attached to alumina surface in Pd/γ-alumina and Pd-MnO_x/γ-alumina catalysts, resulting in high dispersion of Pd on alumina without atomic interaction with manganese oxide clusters. On the other hand, as found by XANES, the fraction of oxidized Pt in Pt-MnO_x/γ-alumina is higher than

that in Pt/γ-alumina. The EXAFS study of Pt also supports the results found from XANES, indicating the decrease in platinum coordination number and the increase in oxygen CN when Pt is added to MnO_x/γ-alumina.

There are reports on the effect of noble metals on transition metal oxides for catalytic combustion of VOCs in the literature [73, 74, 99, 103]. It can be inferred that noble metals can interact with transition metal oxides via their lattice oxygen, changing electronic environment around transition metals. It is also believed that Pt is most likely attached to manganese oxide clusters via MnO_x lattice oxygen, altering Pt and Mn coordination numbers.

Higher activity of Pt-MnO_x/γ-alumina than MnO_x/γ-alumina is attributed to the possibility that the addition of Pt changes electronic properties of Mn, enhancing the activity of manganese oxides by formation of Mn-O-Pt bonds. Basically, attachment of Pt to MnO_x results in more electron occupancy of Mn 3d orbital which is considered to be more favorable in the decomposition of ozone and the oxidation of VOCs [29]. In fact, as it was shown in chapter 5, lower oxidation states of Mn can facilitate the transfer of electrons to ozone. Therefore, one can relate higher activity of Pt-MnO_x/γ-alumina to higher Mn 3d orbital electron occupancy, accelerating the rate of ozone decomposition and consequently the oxidation rate of toluene.

In order to examine the effect of manganese 3d valence electron occupancy on catalytic ozonation of toluene, Pt-MnO_x/γ-alumina and Pd-MnO_x/γ-alumina catalysts are reduced with hydrogen. The catalysts are reduced at 250 ^oC for two hours with pure H_2 at flow rate of 100 ml/min. Fig. F.1 of Appendix F shows XRD of the catalysts after the reduction. Reduced Pt-MnO_x/γ-alumina and Pd-MnO_x/γ-alumina show only MnO peaks (manganosite), corresponding to the reduction of MnO_2 and Mn_2O_3 to MnO. This is in agreement with the TPR profile of Pt-MnO_x/γ-alumina and Pd-MnO_x/γ-alumina shown in Fig.6.2, in which manganese oxides (MnO_2

and Mn_2O_3) are reduced to MnO in one step at 134 ^oC. In fact, the reduction of the bimetallic catalysts with pure hydrogen at 250 ^oC ensures that the only remaining phase of Mn is MnO after the reduction. Activities of the reduced and unreduced catalysts (Pd-MnO_x/γ-alumina, Pt-MnO_x/γ-alumina) are shown in Fig. F.2 and Fig. F.3 of Appendix F in terms of toluene and ozone conversions, respectively. It can be seen that the activity of Pd-MnO_x/γ-alumina increases after the reduction with hydrogen and reaches to a similar level as the unreduced Pt-MnO_x/γ-alumina in terms of ozone and toluene conversions. Activity of the reduced Pt-MnO_x/γ-alumina overlaps with the activity of the unreduced Pt-MnO_x/γ-alumina at room temperature and higher temperatures. Therefore, it can be concluded that lower oxidation state of manganese oxides are more favorable for catalytic ozonation of toluene in agreement with the conclusion made in Chapter 5. Thus, the effect of platinum addition to MnO_x/γ-alumina can be explained by increasing electron occupancy of 3d orbital of Mn since the reduced Pd-MnO_x/γ-alumina showed the same activity as the unreduced Pt-MnO_x/γ-alumina catalyst.

6.3. Summary

This chapter studied the promotional effect of two noble metals (Pt and Pd) on the activity of MnO_x/γ-alumina in the oxidation of toluene. Catalysts were characterized by XRD, H_2-TPR, XANES, and EXAFS. Catalysts activities were obtained in the range of 22-100 ^oC. It was observed that the addition of Pd did not improve the activity of alumina-supported manganese oxides catalysts, whereas the addition of Pt led to 10 ^oC reduction in the required temperature for the complete oxidation of toluene. XANES and EXAFS studies showed no atomic interaction between Pd and Mn while XANES and EXAFS of Pt changed in the presence of Mn. It was concluded that the interaction between Pt and Mn occurs via surface oxygen of manganese oxides, leading to the formation of Mn-O-Pt bonds. The higher activity of Pt-

MnO_x/γ-alumina can be related to the higher electron occupancy of 3d orbital in Mn, accelerating the decomposition rate of ozone and also the rate of toluene oxidation. Activity tests of the reduced catalysts confirmed that lower oxidation states of Mn enhances the activity of the catalysts. This indicated that higher 3d orbital electron occupancy of Mn in Pt-MnO_x/γ-alumina can be the reason for better activity of Pt promoted manganese oxides than the other catalysts.

CHAPTER 7
A STUDY ON KINETICS AND MECHANSIM OF CATALYTIC OXIDATION OF TOLUENE BY OZONE

As it has been mentioned in Chapter 2, one of the unclear issues about the catalytic oxidation of VOCs by ozone is the kinetics and mechanism of the reaction. It is believed that the reaction is a surface phenomenon, following a Langmuir-Hinshelwood mechanism between adsorbed VOC molecules and atomic oxygen. Ozone is decomposed to atomic oxygen and peroxide species on manganese oxides. VOC molecules are assumed to be adsorbed on the catalyst and react with atomic oxygen to start the oxidation reaction. This mechanism has been originally proposed by Oyama and co-workers in order to study the kinetics and mechanism of the oxidation of acetone by ozone over MnO_x/SiO_2 [51]. They have used *in-situ* laser Raman spectroscopy and transient kinetics techniques to determine the reactive surface species and the reaction mechanism. The elementary steps of this mechanism have been presented through Eq. (2.4) to (2.9) in Chapter 2. To the best of the author's knowledge, this is the only systematic work done on the kinetics and mechanism of catalytic ozonation of VOCs. Basically, most of the researchers have simply used Oyama's mechanism in order to explain the mechanism of ozonation of several VOCs such as toluene, benzene, and cyclohexane [21, 25, 53, 58, 69]. This has been done without any attempt to test the validity of this mechanism on VOCs other than acetone. In fact, the generality of the mechanism proposed by Oyama and co-workers has not been studied yet. Therefore, there is need to further study the kinetics of the oxidation of VOCs by ozone in order to explore possible elementary steps involved in the reaction mechanism.

This chapter investigates the kinetics of the catalytic oxidation of toluene by ozone over MnO_x/γ-alumina (10%). This is achieved by obtaining initial reaction rates at constant ozone or

toluene partial pressures. The obtained reaction rates are first fitted to a power law model in order to obtain the apparent activation energy of the reactions and the reaction orders with respect to ozone and toluene. The initial rates are also fitted to a rate equation derived based on the mechanism proposed by Oyama and co-workers in order to check the applicability of this mechanism to catalytic oxidation of toluene. A more detailed mechanism based on the evidence reported on the oxidation of VOCs (especially toluene) is presented in this chapter to show an alternative reaction mechanism for the catalytic ozonation of toluene.

7.1. Data collection and analysis

Oxidation of toluene is carried out in the same experimental set-up explained in Chapter 3. Kinetics data is obtained at four different temperature levels (70, 80, 90, and 100 ^{o}C) since catalyst deactivation occurs below 70 ^{o}C. Experiments are conducted with either constant toluene partial pressure ($P_{tol.}$) of 240 × 10^{-6} atm while ozone partial pressure ($P_{ozo.}$) is changed between 1050 to 3000 × 10^{-6} atm or constant ozone partial pressure of 1050 × 10^{-6} atm with toluene partial pressure of 90 to 180 × 10^{-6} atm. The space time of the reactor is between 0-1212 $kg_{cat.}$ $mol_{tol.}^{-1}$ s. MnO_x/γ-alumina (10%) is diluted with silica carbide, inert in the reaction, to prevent gas phase channeling and temperature gradients along the catalyst bed.

Plots of toluene conversion versus space time are used in order to obtain the initial reaction rates of toluene oxidation ($r_{tol.}$) based on the following equation:

$$r_{tol.} = \frac{dX_{tol.}}{d\left(\frac{W_{cat.}}{F_{tol.,in}}\right)} \tag{7.1}$$

in which, $X_{tol.}$, $W_{cat.}$, and $F_{tol.,in}$ represent toluene conversion, catalyst weight, and inlet molar flow rate of toluene, respectively. Two numerical methods are used to estimate the initial

reaction rates based on Eq. (7.1). The first one is fitting the conversion data by smoothing splines in MATLAB R2006a curve fitting toolbox and obtaining the initial reaction rates by differentiating the splines at zero space time. The second method is based on the fitting of the data with Eq. (7.2) and calculating the initial rates by product of A and B [112]:

$$X_{tol.} = A\left(1 - \exp\left(-B\frac{W_{cat.}}{F_{tol.,in}}\right)\right) \tag{7.2}$$

A and B are the fitting parameters evaluated by fitting Eq. (7.2) to the conversion versus space time data. The initial rates calculated from the two methods, smoothing splines and Eq. (7.2), are averaged and used for kinetics analysis.

Kinetics models are fitted to the experimental data by non-linear least squares technique in MATLAB R2006a using lsqnonlin function to minimize the sum of squared differences between experimental and calculated reaction rates:

$$\text{minimize} \sum_i \sum_j \left(r_{exp.ij} - r_{cal.ij}\right)^2 \tag{7.3}$$

$r_{exp.}$ and $r_{cal.}$ denote experimental and calculated initial rates of toluene oxidation, respectively. Index i refers to different temperature levels (70, 80, 90, and 100 ^oC) and index j refers to j^{th} reaction rate at temperature level i, corresponding to specific toluene and ozone partial pressures. In fact, model parameters including rate constants, toluene adsorption entropy, toluene adsorption enthalpy, and activation energies are simultaneously estimated by Eq. (7.3) which allows non-isothermal fitting of the data. Toluene rate constant and toluene adsorption pressure equilibrium constant are defined by Eq. (7.4) and (7.5), respectively:

$$k = k_o \exp\left(\frac{-E}{RT}\right) \tag{7.4}$$

$$K_{tol.} = \frac{K}{P^o} = \frac{\exp\left(\frac{\Delta S^o_{tol.}}{R} - \frac{\Delta H^o_{tol.}}{RT}\right)}{P^o} \tag{7.5}$$

k, k_o, and K are toluene reaction rate constant, pre-exponential factor, and dimensionless adsorption equilibrium constant respectively. $K_{tol.}$ is the toluene adsorption pressure equilibrium constant. $\Delta S^o_{tol.}$ and $\Delta H^o_{tol.}$ are standard entropy and enthalpy of toluene adsorption. R is the universal gas constant and P^o is the pressure of standard state for gases which is 1 atm. Values of k_o and E are constrained to positive values while $\Delta S^o_{tol.}$ and $\Delta H^o_{tol.}$ are allowed to float in negative and positive ranges to minimize the least square objective function expressed by Eq. (7.3).

Goodness of fits is evaluated based on the coefficient of determination (R^2) [113]:

$$R^2 = 1 - \frac{\sum_i \sum_j \left(r_{exp.ij} - r_{cal.ij}\right)^2}{\sum_i \sum_j \left(r_{exp.ij} - r_{mean}\right)^2} \tag{7.6}$$

r_{mean} is the average reaction rate over all data points. i and j are the same as Eq. (7.3). Kinetic models are compared by Fisher's F-test in order to compare different fits [114]:

$$F_c = \frac{\sum_i \sum_j \frac{\left(r_{cal.,ij}\right)^2}{P}}{\sum_i \sum_j \frac{\left(r_{exp.ij} - r_{cal.ij}\right)^2}{DF}} \tag{7.7}$$

Definitions of i and j indices are the same as Eq. (7.3). DF is the degree of freedom, defined as the difference between the number of experimental data points and the number of fitting parameters (P). The best model among the rival models can be distinguished by using Eq. (7.7), suggesting that models with higher F_c values have higher regression significant.

7.2. Effect of toluene and ozone partial pressures on toluene oxidation

The effect of toluene and ozone partial pressures on toluene conversion at different reactor space times and temperatures is shown in Fig. 7.1 and 7.2. Fig. 7.1 indicates changes in toluene conversion at constant ozone partial pressure when toluene partial pressure is increased. Four toluene partial pressures are considered at 90, 120, 180, and 240 × 10^{-6} atm while the partial pressure of ozone is kept at 1050 × 10^{-6} atm. Toluene conversions ($X_{tol.}$) versus space time ($W_{cat.}/F_{tol.}$) at each toluene partial pressure are shown in Fig. 7.1 (A), (B), (C), and (D). Conversions are obtained at four temperature levels of 70, 80, 90, and 100 ^{o}C. Space time of the reactor ranges from 0 to 1212 $kg_{cat.}$ $mol_{tol.}^{-1}$ s. Results show that at a constant reactor space time, toluene conversion decreases by the increase of toluene partial pressure while toluene conversions increase by the increasing the temperature.

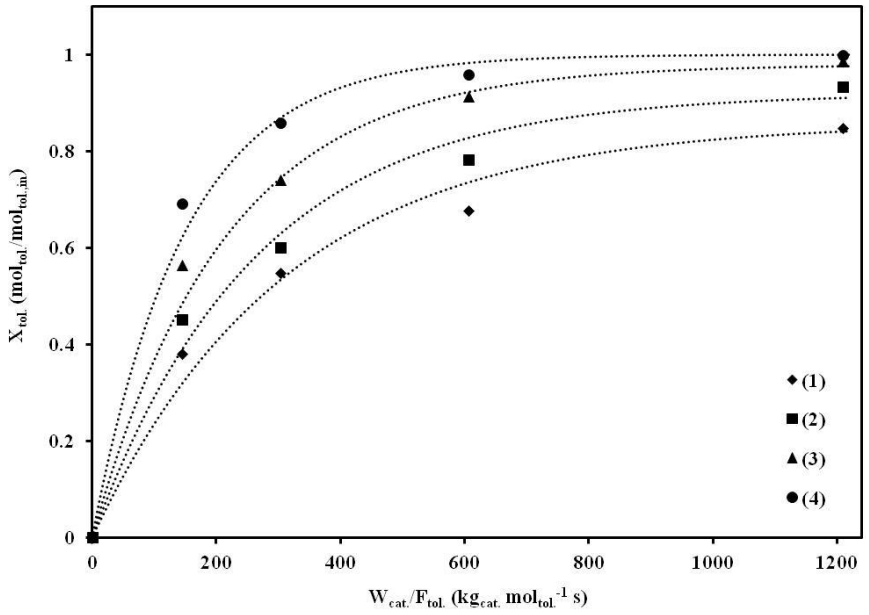

(A)

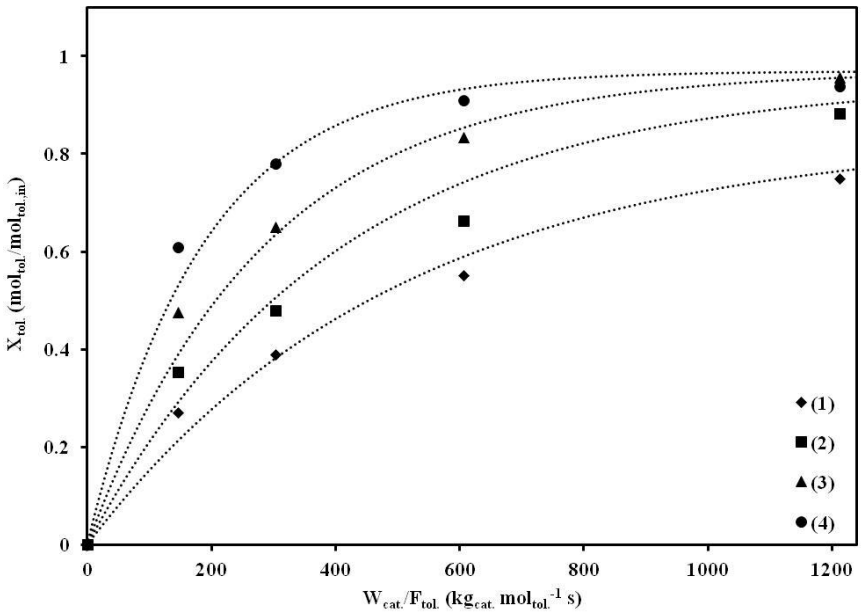
1
0.8
0.6
0.4
0.2
0
0
200
400
600
800
1000
1200
$X_{tol.}$ ($mol_{tol.}/mol_{tol.,in}$)
$W_{cat.}/F_{tol.}$ ($kg_{cat.}$ $mol_{tol.}^{-1}$ s)
(1)
(2)
(3)
(4)

(B)

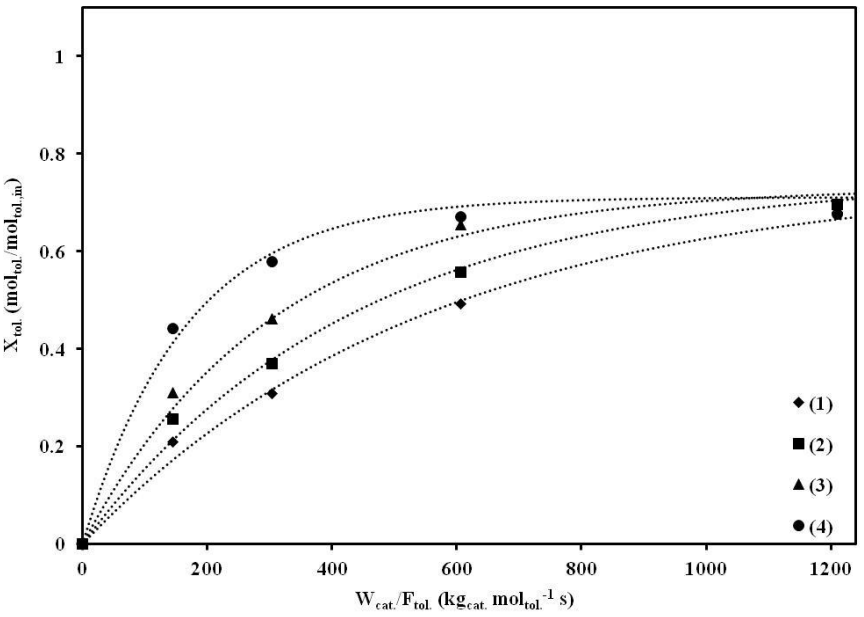
1
0.8
0.6
0.4
0.2
0
0
200
400
600
800
1000
1200
$X_{tol.}$ ($mol_{tol.}/mol_{tol.,in}$)
$W_{cat.}/F_{tol.}$ ($kg_{cat.}$ $mol_{tol.}^{-1}$ s)
(1)
(2)
(3)
(4)

(C)

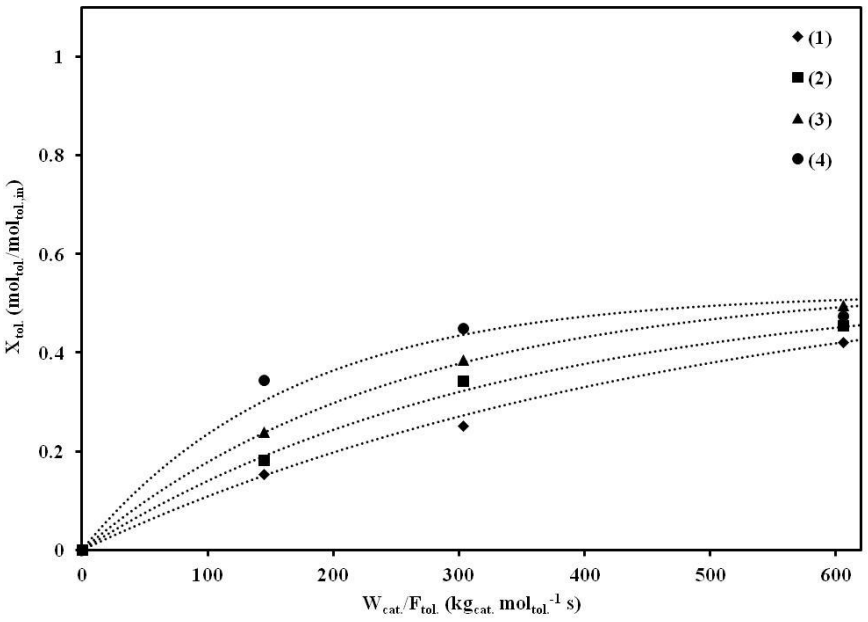

(D)

Fig. 7.1. Toluene conversion versus space time at constant ozone partial pressure ($P_{ozo.}$) of 1050 × 10^{-6} atm and variable toluene partial pressures ($P_{tol.}$) at different temperatures; (A) $P_{tol.}$=90 × 10^{-6} atm, (B) $P_{tol.}$=120 × 10^{-6} atm, (C) $P_{tol.}$=180 × 10^{-6} atm, and (D) $P_{tol.}$=240 × 10^{-6} atm; (1) 70 ^{o}C, (2) 80 ^{o}C, (3) 90 ^{o}C, and (4) 100 ^{o}C. Dotted lines show the trend of data.

By visual inspection of Fig. 7.1 (A) to Fig. 7.1 (D) at different $P_{tol.}$, it can be seen that the slope of toluene conversion versus space time decreases at zero space time by increasing toluene partial pressure. This implies that the initial rate of toluene oxidation decreases by the increase of toluene concentration. Fig. 7.2 shows the effect of $P_{ozo.}$ on toluene conversion when $P_{tol.}$ is kept constant at 240 × 10^{-6} atm.

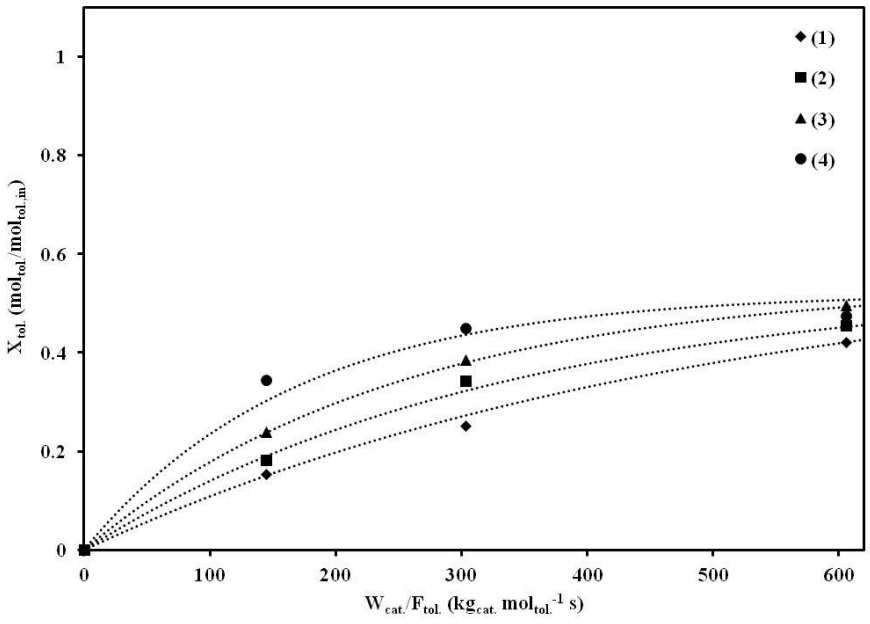
(1)
(2)
(3)
(4)
$X_{tol.}$ ($mol_{tol.}/mol_{tol.in}$)
$W_{cat.}/F_{tol.}$ ($kg_{cat.}$ $mol_{tol.}^{-1}$ s)
0
0.2
0.4
0.6
0.8
1
0
100
200
300
400
500
600

(A)

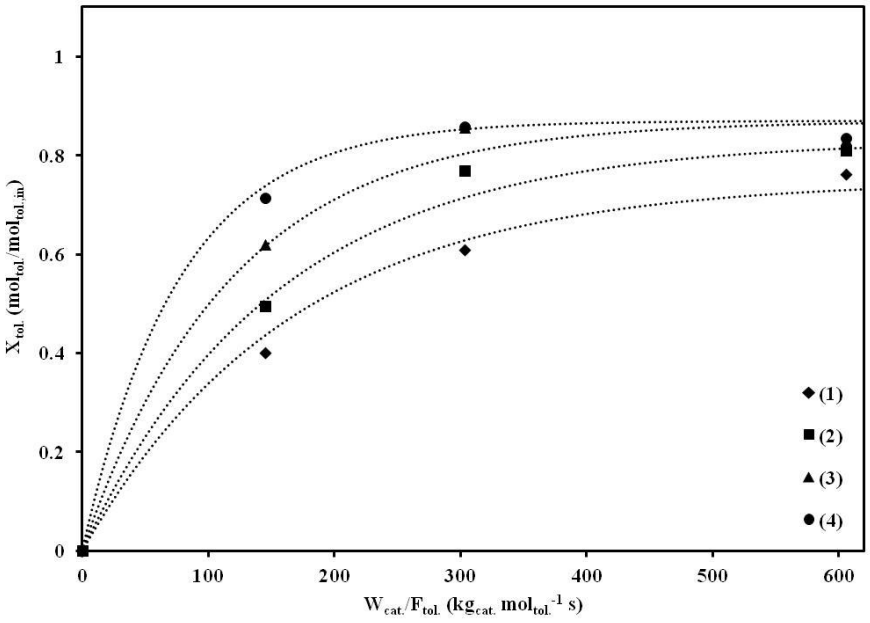
(1)
(2)
(3)
(4)
$X_{tol.}$ ($mol_{tol.}/mol_{tol.in}$)
$W_{cat.}/F_{tol.}$ ($kg_{cat.}$ $mol_{tol.}^{-1}$ s)
0
0.2
0.4
0.6
0.8
1
0
100
200
300
400
500
600

(B)

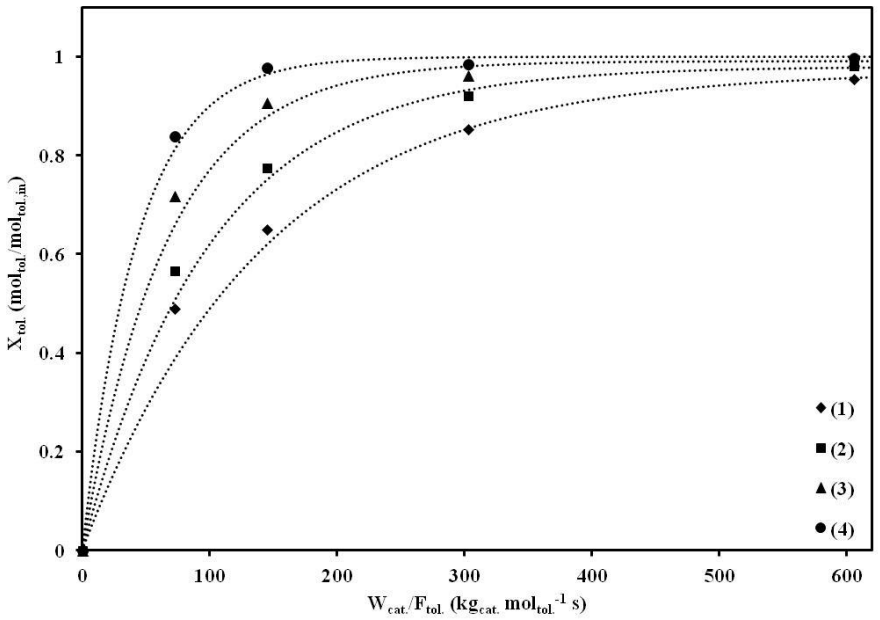

(C)

Fig. 7.2. Toluene conversion versus space time at constant toluene partial pressure ($P_{tol.}$) of 240 × 10^{-6} atm and variable ozone partial pressures ($P_{ozo.}$) at different temperatures; (A) $P_{ozo.}$=1050 × 10^{-6} atm, (B) $P_{ozo.}$=2000 × 10^{-6} atm, and (C) $P_{ozo.}$=3000 × 10^{-6} atm; (1) 70 ^{o}C, (2) 80 ^{o}C, (3) 90 ^{o}C, and (4) 100 ^{o}C. Dotted lines show the trend of data.

Toluene conversions were obtained at three ozone partial pressures of 1050, 2000, and 3000 × 10^{-6} atm, shown in Fig. 7.2 (A), (B), and (C), respectively. In contrast to the result of fixed $P_{tol.}$, toluene conversions increase by increasing $P_{ozo.}$ at a fixed reactor space time. It can also be observed that the slope of $X_{tol.}$ versus $W_{cat.}/F_{tol.}$ at zero space time and consequently the rate of toluene oxidation increases by the increase of ozone partial pressure.

7.3. Kinetics modeling

Initial reaction rates can be estimated form Fig. 7.1 and Fig. 7.2 in order to fit different kinetics models to the experimental data. Power law model is the first model used in section

7.3.1 to determine the apparent activation energy of the reaction and toluene and ozone reaction orders. The second reaction rate equation is based on the mechanism proposed by Oyama and co-workers for ozonation of acetone [51]. This model is based on a Langmuir-Hinshelwood (LH1) mechanism, in which adsorbed toluene molecules are activated by surface atomic oxygen. The result of the fitting of LH1 is presented in section 7.3.2, in which the goal is to examine the applicability of Oyama's mechanism to VOCs other than acetone. Eventually, a new mechanism is proposed in section 7.3.3 based on recently published papers on the oxidation of VOCs by atomic oxygen. This mechanism is also developed based on a Langmuir-Hinshelwood mechanism which will be referred to as LH2. LH2 mechanism helps to introduce an alternative mechanism scheme to LH1 which might better explain the catalytic oxidation of toluene by ozone.

7.3.1. Power law model

The power law model is expressed as:

$$r_{tol.} = k\, P_{tol.}^{n} P_{ozo.}^{m} \tag{7.8}$$

The result of fitting Eq. (7.8) to the initial reaction rates is included in Table 7.1 and Fig. 7.3. The reaction orders with respect to toluene and ozone are -1 and 2, respectively. Fig. 7.3 (A) indicates that $P_{tol.}$ has a negative effect on the initial reaction rate, causing the reaction rate to decrease by increasing toluene partial pressure from 90 to 240 × 10^{-6} atm. This results in a reaction order of -1 in Eq. (7.8) for toluene. On the other hand, Fig. 7.3 (B) shows that the initial rate of toluene oxidation increases by increasing ozone partial pressure from 1050 to 3000 × 10^{-6} atm which leads to an ozone reaction order of 2. The apparent activation energy (E) of the

reaction is determined to be 31.0 kJ mol^{-1} which is close to the value reported by Naydenov and Mehandjiev for the oxidation of benzene over MnO_2 by ozone, i.e. 30 kJ mol^{-1} [41].

Table 7.1. Fitting results of the power law model [a]

$$r_{tol.} = k\, P_{tol.}^{n} P_{ozo.}^{m}, k = k_o \exp\left(\frac{-E}{RT}\right)$$

n	m	k_o ($mol_{tol.}$ $kg_{cat.}$ s^{-1} atm^{-1}) × 10^{-4}	E (kJ mol^{-1})	R^2	F_c
-1.0 ± 0.2	2.0 ± 0.1	1.1 ± 0.8	31.0 ± 0.3	0.996	1705

[a] Uncertainties are based on 95% confidence intervals.

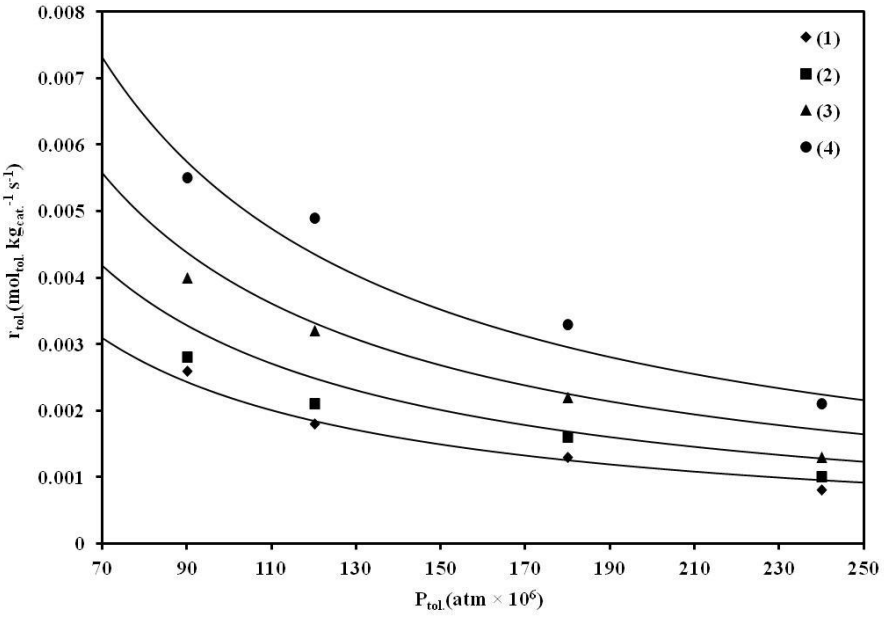

(A)

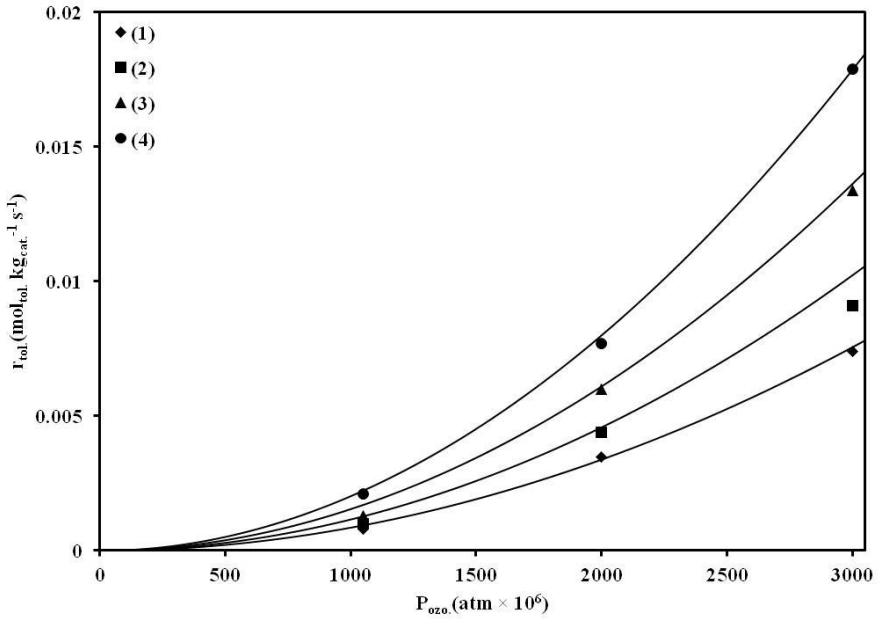

(B)

Fig. 7.3. Initial reaction rates and the power law model; (A) Constant ozone partial pressure ($P_{ozo.}$) at 1050×10^{-6} atm; (B) Constant toluene partial pressure ($P_{tol.}$) at 240×10^{-6} atm; (1) 70 ^{o}C, (2) 80 ^{o}C, (3) 90 ^{o}C, (4) 100 ^{o}C. Solid lines show the predicted initial reaction rates by the power law model.

The apparent activation energy of the reaction (31.0 kJ mol^{-1}) is lower than the activation energy of catalytic total oxidation of toluene by oxygen which has been reported to be between 75 and 106 kJ mol^{-1} [115]. The decrease of the activation energy can be considered to be the main reason for the effectiveness of the oxidation of VOCs by ozone which makes it possible to oxidize VOCs below 100 ^{o}C. The activation energy of the reaction (31.0 kJ mol^{-1}) is also lower than the activation energy of the homogeneous reaction between toluene and ozone (55.6 kJ mol^{-1}) reported for partial oxidation of toluene by ozone [116]. This indicates that the oxidation of toluene by ozone over MnO_x/γ-alumina is a heterogeneous reaction catalyzed by manganese oxides.

7.3.2. Langmuir-Hinshelwood mechanism (LH1) based on toluene activation by atomic oxygen

As mentioned before, this mechanism (LH1) is originally suggested by Oyama and co-workers for catalytic oxidation of acetone by ozone [51]. The elementary steps of LH1 mechanism are shown in Table 7.2. The mechanism consists of two catalytic cycles. The first cycle is ozone decomposition which is shown by steps (1) to (3) in Table 7.2. These three steps are considered for the decomposition of ozone to atomic oxygen and peroxide species which eventually decompose ozone to molecular oxygen. The second cycle is composed of quasi equilibrated adsorption of toluene by step (4) and reaction with atomic oxygen in step (5) to activate the adsorbed toluene molecule and to start the oxidation reaction. It is assumed that further steps after step (5) are fast and are not significant from kinetics point of view. The two cycles are coupled to each other by consuming atomic oxygen. If n oxygen atoms are consumed in step (5) in Table 7.2, the rate of toluene oxidation will be [51]:

$$r_{tol.} = K_{tol.} \frac{k'_1 P_{tol.} P_{ozo.}^{n}}{\left(1 + k'_2 P_{ozo.} + K_{tol.} P_{tol.}\right)^{n+1}} \tag{7.9}$$

In which, $K_{tol.}$ is expressed by Eq. (7.5). k'_1 and k'_2 are defined as follows:

$$k'_1 = \frac{k_1}{k_3} k_5 = k'_{1o} \exp\left(\frac{-E'_1}{RT}\right) \tag{7.10}$$

$$k'_2 = \frac{k_1}{k_3} = k'_{2o} \exp\left(\frac{-E'_2}{RT}\right) \tag{7.11}$$

Table 7.2. Elementary steps of LH1 mechanism

Elementary steps based on [51]		Reaction rate/Equilibrium constant
(1)	$O_3 + * \rightarrow O_2 + O^*$	k_1
(2)	$O_3 + O^* \rightarrow O_2 + O_2^*$	k_2
(3)	$O_2^* \rightarrow O_2 + *$	k_3
(4)	$C_6H_5\text{-}CH_3 + * \rightleftharpoons C_6H_5\text{-}CH_3^*$	$K_{tol.}$
(5)	$C_6H_5\text{-}CH_3^* + nO^* \rightarrow$ products	k_5

The first term in the denominator of Eq. (7.9) corresponds to the fraction of vacant catalyst active sites (θ^*) which are proposed to be Mn atoms. The second term in the denominator ($k'_2 P_{ozo.}$) is related to the fraction of active sites covered by peroxide species ($\theta_{O_2^*}$) and the last term ($K_{tol.} P_{tol.}$) is due to the fraction of active sites covered by toluene molecules ($\theta_{tol.^*}$). The concentration of surface atomic species is assumed to be negligible due to the high reactivity and short lifetime of these species. Oyama and co-workers have shown that peroxide species are spectators in the catalytic oxidation of acetone by ozone and atomic oxygen is responsible for the oxidation reaction [51]. However, they have considered the peroxide species in the calculation of the fraction of vacant active sites.

Results of the fitting of Eq. (7.9) to the initial reaction rates are shown in Table 7.3. It is found that 2 oxygen atoms are necessary to start the oxidation reaction by step (5) in Table 7.2. The first pre-exponential factor (k'_{1o}) is much larger than the second pre-exponential factor (k'_{2o}). The high value of k'_{1o} shows that step (5) is probably a fast step with high reaction rate constant since k'_1 is defined as the product of k_5 and k'_2. The value of E'_2 (89.3 kJ mol^{-1}) is

positive which shows that the activation energy of the desorption of oxygen molecule in step (3) is larger than the activation energy of ozone adsorption in step (1).

Table 7.3. Fitting result of LH1 mechanism based on Eq. (7.9)

n	k'_{1o} ($mol_{tol.}\ kg_{cat.}^{-1}\ s^{-1}\ atm^{-2}$)	E'_1 (kJ mol^{-1})	k'_{2o} (atm^{-1})	E'_2 (kJ mol^{-1})	$\Delta S^{o}_{tol.}$ (J $mol^{-1}\ K^{-1}$)	$\Delta H^{o}_{tol.}$ (kJ mol^{-1})
2	3×10^{10}	41	0.2	89	100	8

By calculating $K_{tol.}$ using Eq. (7.5) and the values reported in Table 7.3, one can conclude that $K_{tol.}P_{tol.} >> k'_2P_{ozo.}$. This shows that fraction of active sites covered by peroxide species are negligible in comparison with the ones occupied by toluene. This is in agreement with the findings of Oyama and co-workers, showing that peroxide species are spectators in the reaction and should not appear in the rate equation. Therefore, Eq. (7.9) can be reduced to a simpler rate equation by excluding the fraction of peroxide species:

$$r_{tol.} = K_{tol.}\frac{k'_1 P_{tol.} P^{n}_{ozo.}}{\left(1+K_{tol.}P_{tol.}\right)^{n+1}} \qquad (7.12)$$

The results of fitting Eq. (7.12) to the initial reaction rates are shown in Fig. 7.4 and Table. 7.4. The same values are estimated for n, k'_{1o}, E'_1, $\Delta S_{tol.}$, and $\Delta H_{tol.}$, showing that the surface peroxide species are most likely not involved in the reaction mechanism.

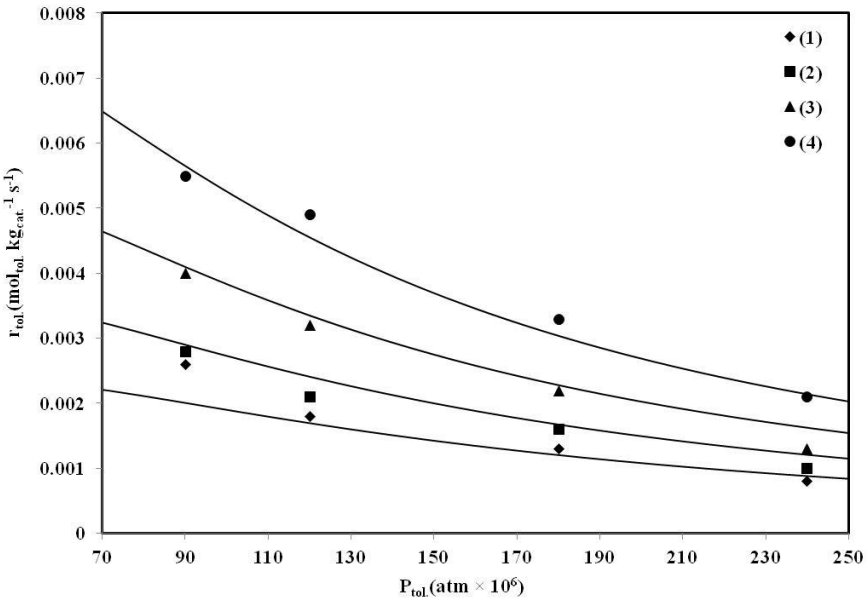

(A)

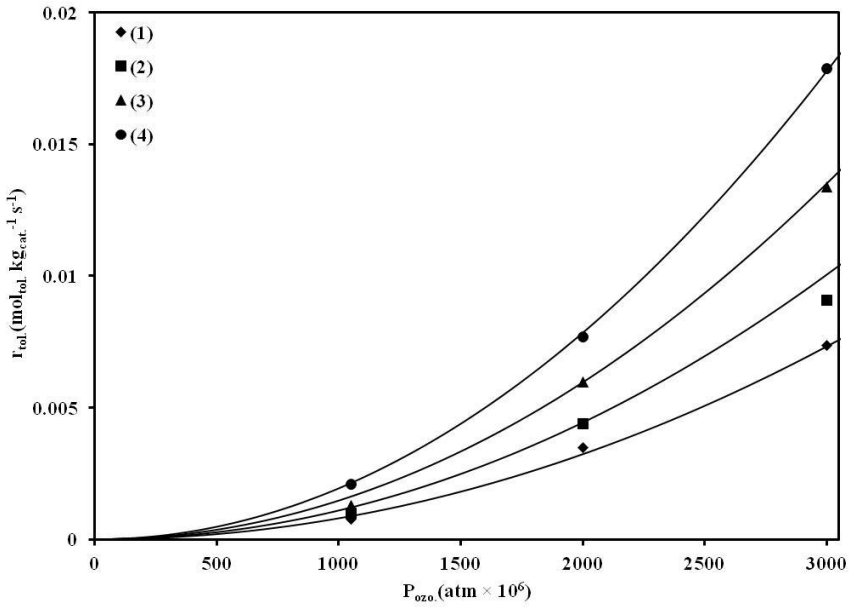

(B)

Fig. 7.4. Initial reaction rates and LH1 model; (A) Constant ozone partial pressure ($P_{ozo.}$) at 1050 $\times 10^{-6}$ atm; (B) Constant toluene partial pressure ($P_{tol.}$) at 240 $\times 10^{-6}$ atm; (1) 70 ^{o}C, (2) 80 ^{o}C, (3) 90 ^{o}C, (4) 100 ^{o}C. Solid lines show the predicted initial reaction rates by the power law model.

Table 7.4. Fitting result of LH1 mechanism based on Eq. (7.12) [a]

n	$k'_{1o} \times 10^{-10}$ ($mol_{tol.}\ kg_{cat.}^{-1}\ s^{-1}\ atm^{-2}$)	E'_1 (kJ mol^{-1})	$\Delta S^{o}_{tol.}$ (J $mol^{-1}\ K^{-1}$)	$\Delta H^{o}_{tol.}$ (kJ mol^{-1})	R^2	F_c
2.0 ± 0.1	3 ± 1.4	41.2 ± 19.4	100.1 ± 46.3	7.9 ± 16.2	0.997	1402

[a] Uncertainties are based on 95% confidence intervals.

The value of standard entropy ($\Delta S^{o}_{tol.}$) and enthalpy ($\Delta H^{o}_{tol.}$) of toluene adsorption are positive in Table 7.4. Considering the confidence intervals reported for $\Delta S_{tol.}$, it can be seen that the fitting of LH1 mechanism to experimental data results in a positive value for entropy of toluene adsorption. It has been mentioned by Froment and Vannice that adsorption entropy should satisfy the following criterion in catalytic reactions [114, 117]:

$$0 \langle -\Delta S^{o}_{ads} \langle S^{o}_{g} \tag{7.13}$$

ΔS^{o}_{ads} is the standard entropy of adsorption and S^{o}_{g} is the standard entropy in the gas phase with the value of 320.7 J $mol^{-1}\ K^{-1}$ [115]. It can be observed that the positive value of toluene entropy of adsorption does not satisfy Eq. (7.13), indicating that LH1 mechanism most probably cannot adequately explain the mechanism of catalytic oxidation of toluene by ozone.

Fisher's F_c values can be used to compare the power law model and LH1 mechanisms from statistical point of view. The F_c corresponding to the power law model (1705) is larger than that of the LH1 mechanism (1402) since the number of fitting parameters is less in the power law model. However, both models seem to perfectly follow the trend of the experimental data.

7.3.3. Langmuir-Hinshelwood mechanism (LH2) based on toluene activation by hydrogen abstraction

Even though the LH1 mechanism, presented in Table 7.2, agrees well with the experimental data, it results in a positive value for the entropy of toluene adsorption which is not acceptable for catalytic reactions following Langmuir-Hinshelwood mechanisms. In fact, LH1 mechanism has been originally proposed for acetone oxidation and it might not be necessarily suitable for the oxidation of other VOCs such as toluene. Thus, it was attempted to modify the LH1 mechanism based on evidences reported on the mechanism of catalytic oxidation of hydrocarbons and especially toluene by atomic oxygen.

It has been proposed that toluene interacts dissociatively with the surface of transition metal oxides via abstraction of one H atom from the methyl group producing one adsorbed proton and adsorbed radical benzyl species [118-120]. This step is considered to be the first step in the oxidation of toluene. Iglesia and co-workers also proved with isotopic data and density functional theory (DFT) calculations that C-H bond cleavage is the kinetically relevant step in the oxidation of alkanes (C_nH_{2n+2}) which occurs on catalyst active site pairs [121, 122]. The research group of Marin has also studied the reaction network of catalytic toluene oxidation by temporal analysis of products (TAP) and isotopic techniques [123]. They have observed that hydrogen abstraction from the methyl and phenyl groups occurs before the oxidation of carbon atoms, releasing H_2O before the detection of CO_2. The application of C-H bond cleavage model for catalytic oxidation of hydrocarbons by ozone has also been used by Li and Oyama for catalytic ozonation of ethanol, even though the authors did not propose a rate equation based on this mechanism [18].

Therefore, a second Langmuir-Hinshelwood mechanism (LH2) is proposed for the oxidation of toluene by ozone based on the initiation of the reaction by hydrogen abstraction

from the methyl group [51, 122, 123]. The scheme of the mechanism is shown in Table 7.5. No by-products other than CO, CO_2 and water vapor are considered in the scheme.

Table 7.5. Scheme of the Langmuir-Hinshelwood mechanism (LH2) based on C-H activation

	Step	Reaction rate/Equilibrium constant
(1)	$O_3 + * \rightarrow O_2 + O^*$	k_1
(2)	$O_3 + O^* \rightarrow O_2 + O_2^*$	k_2
(3)	$O_2^* \rightarrow O_2 + *$	k_3
(4)	$C_6H_5\text{-}CH_3 + * \rightleftharpoons C_6H_5\text{-}CH_3^*$	$K_{tol.}$
(5)	$C_6H_5\text{-}CH_3^* + * \rightarrow C_6H_5\text{-}CH_2^* + H^*$	k_5
(6)	$C_6H_5\text{-}CH_2^* + 7^* \rightarrow C_6\text{–}C^* + 7H^*$	k_6
(7)	$H^* + O^* \rightleftharpoons OH^* + *$	K_7
(8)	$2OH^* \rightleftharpoons H_2O^* + O^*$	K_8
(9)	$H_2O^* \rightleftharpoons H_2O + *$	K_9
(10)	$C_6\text{–}C^* + O^* \rightarrow C_6^* + CO^*$	k_{10}
(11)	$C_6^* + 6O^* \rightarrow 6CO^*$	k_{11}
(12)	$CO^* + O^* \rightarrow CO_2^* + *$	k_{12}
(13)	$CO^* \rightleftharpoons CO + *$	K_{13}
(14)	$CO_2 \rightleftharpoons CO_2 + *$	K_{14}

The first three steps in Table 7.5 are considered for the decomposition of ozone. The fourth step is quasi equilibrated adsorption of toluene on the first catalyst site. The fifth step is release of one proton on the second catalyst site from the adsorbed toluene molecule to produce $C_6H_5\text{-}CH_2^*$ and H^*. $C_6H_5\text{-}CH_2^*$ undergoes successive H abstractions to produce more H^* and a

hydrogen free carbon structure (C_6-C^*) shown in step 6. The protons react with adsorbed oxygen atoms to produce OH^* at the seventh step. The produced OH^* species combine and produce water through steps 8 and 9 in Table 7.5. The next step would be the reaction of the carbon atom from the methyl group in step 10 to produce an adsorbed CO molecule, leaving the C_6 ring (C_6^*). The ring opening occurs in step (11) of Table 7.5, in which adsorbed CO molecules are formed. The adsorbed CO molecules can be oxidized to CO_2 in step (12) or desorb via step (13). The generated CO_2 molecules can leave the surface in step (14).

It has to be noted that step (6) and (11) are not elementary steps. Step (6) represents successive abstraction of hydrogen from C_6H_5-CH_2^* while step (11) indicates successive oxidation of carbon atoms in the C_6 ring by atomic oxygen. Fig. 7.5 shows a simple illustration of the mechanism shown in Table 7.5. It indicates two catalytic cycles, consisting of ozone decomposition and the oxidation of toluene. Toluene is assumed to be adsorbed by the abstraction of one hydrogen atoms on two adjacent sites. The adsorbed toluene reacts with atomic oxygen to produce oxidation by-products.

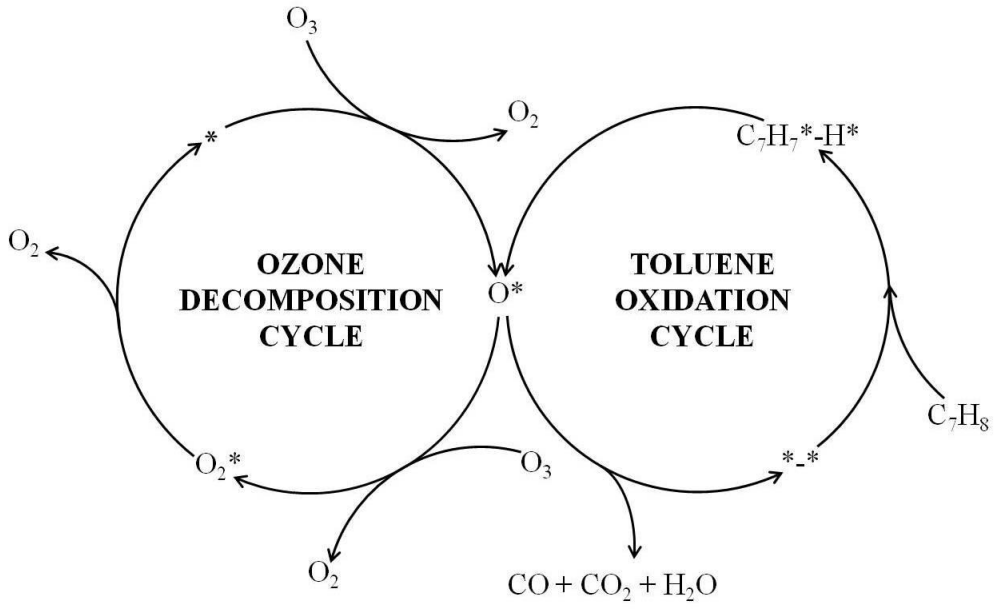

Fig. 7.5. Simple illustration of LH2 mechanism

Assuming that CO, CO_2, and H_2O are the only by-products of the reaction and all O^* atoms react with toluene, the steady state mass balance for O^* gives:

$$r_1 = r_7 - r_8 + r_{10} + 6r_{11} + r_{12} \tag{7.14}$$

In which, r_1 is the rate of generation of surface atomic oxygen (O^*) by step (1) in Table 7.5. r_7, r_{10}, r_{11}, and r_{12} are the rate of consumption of ozone by step (7), (10), (11), and (12), respectively. r_8 is the rate of recombination of OH^* in step (8). It should be noted that r_{11} is the reaction rate between one carbon atom from the C_6 ring (C_6^*) with one adsorbed oxygen atom (O^*) which can be expressed by:

$$r_{11} = k_{11}\theta_{O^*}\theta_{C_n^*}, n = 1,...,6 \tag{7.15}$$

Therefore, r_{11} is multiplied by 6 in Eq. (7.14) assuming that reaction rates of carbon atoms from the C_6^* ring with O^* are equal. Steady state mass balance for $C_6H_5\text{-}CH_2^*$ and H^* results in:

$$r_6 = r_5 \tag{7.16}$$

$$r_7 = r_5 + 7r_6 = 8r_5 \tag{7.17}$$

r_6 is the rate of successive abstraction of one hydrogen atom from $C_6H_5\text{-}CH_2^*$:

$$r_6 = k_6\theta^*\theta_{C_7H_n^*}, n = 1,...,7 \tag{7.18}$$

$C_6H_5\text{-}CH_2^*$ is shown by $C_7H_n^*$ in Eq. (7.18) for simplicity. Steady state mass balance for OH^* gives:

$$r_7 = 2r_8 \tag{7.19}$$

Therefore r_8 becomes:

$$r_8 = \frac{r_7}{2} = 4r_5 \tag{7.20}$$

Steady state mass balance for $C_6\text{-}C^*$, C_6^* and CO^* leads to Eq. (7.21), (7.22), and (7.23), respectively:

$$r_{10} = r_6 = r_5 \tag{7.21}$$

$$r_{11} = r_{10} = r_6 = r_5 \tag{7.22}$$

$$r_{12} + r_{13} = r_{10} + 6r_{11} = 7r_5 \tag{7.23}$$

Selectivity of $C_6H_5\text{-}CH_2^*$ to CO can be defined as:

$$S_{CO} = \frac{r_{13}}{7r_5} \tag{7.24}$$

Inserting (7.24) into (7.23):

$$r_{12} = 7(1 - S_{CO})r_5 \tag{7.25}$$

By substituting Eq. (7.17), (7.20), (7.21), (7.22), and (7.25) into Eq. (7.14), the rate of ozone decomposition by step (1) in Table 7.5 will be:

$$r_1 = [11 + 7(1 - S_{CO})]r_5 = \nu_{ozo.}r_5 \tag{7.26}$$

$\nu_{ozo.}$ is ozone theoretical stoichiometric coefficient which is expressed by:

$$\nu_{ozo.} = 11 + 7\left(1 - S_{CO}\right) \tag{7.27}$$

r_1 and r_5 are defined by Eq. (7.28) and (7.29), respectively:

$$r_1 = k_1 P_{ozo.} \theta^* \tag{7.28}$$

$$r_5 = k_5 \theta_{C_6H_5-CH_3^*} \theta^* \tag{7.29}$$

$\theta_{C_6H_5-CH_3^*}$ can be determined from step (4) in Table 7.5 by using pressure equilibrium constant of toluene:

$$\theta_{C_6H_5-CH_3^*} = K_{tol.} P_{tol.} \theta^* \tag{7.30}$$

Combining Eq. (7.28), (7.29), and (7.30) with Eq. (7.26), we have:

$$r_1 = k_1 P_{ozo.} \theta^* = \nu_{ozo.} r_5 = \nu_{ozo.} k_5 K_{tol.} P_{tol.} \theta^{*2} \tag{7.31}$$

Eq. (7.31) can be used to determine θ^*:

$$\theta^* = \frac{k_1 P_{ozo.}}{\nu_{ozo.} k_5 K_{tol.} P_{tol.}} \tag{7.32}$$

Substitution of Eq. (7.32) into Eq. (7.31), the rate of toluene oxidation becomes:

$$r_{tol.} = r_5 = \frac{r_1}{\nu_{ozo.}} = \frac{k_1^2 P_{ozo.}^2}{\nu_{ozo.}^2 k_5 K_{tol.} P_{tol.}} = k_{eff} P_{tol.}^{-1} P_{ozo.}^2 \tag{7.33}$$

$$k_{eff.} = \frac{k_1^2}{\nu_{ozo.}^2 k_5 K_{tol.}} \tag{7.34}$$

Eq. (7.33) is the rate equation of the LH2 mechanism showing that order of the reaction is -1 and 2 with respect to toluene and ozone, respectively. The rate equation of the LH2 model is the same as the rate expression obtained by the power law model via Eq. (7.8). Both models result in the same reaction orders for toluene and ozone. Therefore, one can estimate $k_{eff.}$ from the value

of pre-exponential factor (k_o) and the activation energy (E) reported in Table 7.1 for the power law model. Eq. (7.33) also shows that the rate of toluene oxidation is proportional to the square of k_1, indicating that higher rates of ozone decomposition accelerates the rate of toluene oxidation in agreement with the findings of Chapters 5 and 6. It can be seen that LH2 mechanism can be considered as the second Langmuir-Hinshelwood mechanism, proposing the elementary steps involved in oxidation of toluene. However, LH2 mechanism has been suggested based on what has been reported in the literature for similar reactions and more experimental and theoretical details are needed to prove the validity of the LH2 mechanism.

7.4. Summary

Chapter 7 presents a study on the kinetics and mechanism of catalytic oxidation of toluene by ozone. Kinetics data were analyzed based on the initial reaction rates. It was revealed that increasing the toluene partial pressure reduced the reaction rate while higher ozone partial pressures increased the rate of toluene oxidation. The apparent activation energy of the reaction was determined to be 31 kJ mol^{-1}, explaining the low temperature activity of the catalyst in the presence of ozone. The power law reaction orders were -1 and 2 for toluene and ozone, respectively.

A Langmuir-Hinshelwood mechanism (LH1) was used to explain the elementary steps involved in the oxidation of toluene by ozone. This mechanism was originally proposed for the catalytic oxidation of acetone by ozone over silica supported manganese oxides. Results showed that two surface oxygen atoms might be involved to start the oxidation of toluene. It was also observed that the concentration of surface peroxide species was low and these species could be considered as spectators in the reaction as it was suggested by Oyama and co-workers [51].

However, LH1 model resulted in a positive value for the standard entropy of toluene adsorption which is not commonly observed in catalytic reactions.

Therefore, a second Langmuir-Hinshelwood mechanism (LH2) was proposed to introduce an alternative approach to the reaction mechanism. The LH2 model explained the oxidation mechanism in more detail which was developed by considering the C-H bond cleavage from the methyl group. It was assumed that the adsorbed toluene molecule was dehydrogenated first to produce water vapor. The hydrogen free carbon structure was further oxidized to produce CO and CO_2. The LH2 model resulted in a simple power law model with the reaction orders of -1 and 2 for toluene and ozone, respectively. In fact, the LH2 mechanism is the same as the power law model with the same reaction orders.

The judgment about rejecting one of these models (LH1 or LH2) is possible by evaluating the reaction rates at toluene partial pressures close to zero while ozone partial pressure is kept constant. Basically, the LH1 mechanism predicts the rate of toluene oxidation to approach zero when the partial pressure of toluene decreases to zero. On the other hand, the LH2 (the power law model) predicts large reaction rates when toluene partial pressure is moving toward zero. However, the discrimination between the two models has not been carried out in this research work due to analytical limitations. Nevertheless, the goal of Chapter 7 was to introduce an alternative mechanism scheme which could also be considered to explain the mechanism of toluene oxidation. It is clear that further evidence is needed to fully understand the mechanism of this reaction which can be the subject of a future work.

CHAPTER 8
SUMMARY

8.1. Summary of the thesis

Catalytic ozonation of toluene by ozone over alumina supported manganese oxides was investigated in this thesis. The motivation behind this research was studying the effectiveness of catalysts in low temperature oxidation of indoor VOCs, contributing to sick building syndrome. It was concluded in Chapter 2 that sorption filtration was the most efficient method for indoor air purification. However, deactivation was reported in sorption filtration, making the regeneration of adsorbents necessary. Other methods such as photo-catalytic oxidation (PCO) and non-thermal plasma (NTP) needed more study in order to overcome the deficiencies related to these methods. Oxidation could be considered as an alternative method for the removal of VOCs from air. However, homogenous oxidation of VOCs was considered to be highly energy consuming, occurring at elevated temperatures. Catalysis might be applied to oxidation reactions in order to lower the reaction temperature. More energy saving in oxidation processes could also be achieved by replacing oxygen with ozone and using appropriate catalysts. A wide range of molecules such as ethanol, acetone, benzene, cyclohexane, formaldehyde, and toluene was oxidized by this method. Results showed that it was possible to convert these pollutants to CO, CO_2, and water vapor in the temperature range of 22-100 ^{o}C, depending on the reaction conditions. In addition to the energy saving, catalytic ozonation of VOCs had the advantage of using transition metals which were cheaper than noble metals used in the catalytic oxidation of VOCs by oxygen. Manganese oxides were reported to be the most active transition metal oxides in the decomposition of ozone and the oxidation of VOCs. The high activity of manganese oxides was related to the capability of these oxides to have different oxidation states during

catalytic cycle of VOCs oxidation. Therefore, the current research work was dedicated to study different aspects of catalytic oxidation of VOCs by ozone. Toluene was selected as the model compound since it was reported to be one of the major indoor air VOCs. In addition, there were a few reports on the catalytic oxidation of toluene by ozone published in the literature, making toluene to be a suitable model compound. The catalyst of interest was alumina supported manganese oxides due to the high activity of these oxides in ozonation reactions.

Oxidation of toluene was performed in a continuous fixed bed reactor. The pressure of the reactor was atmospheric and the temperature range was between 22-100 ^{o}C. Typical concentrations of ozone and toluene were 1050 and 120 ppm, respectively. The method of catalyst preparation was dry impregnation. The detail of the experimental set-up, analysis, and the catalyst preparation was given in Chapter 3. Catalyst characterization and activity tests were presented in Chapter 4. Characterization techniques such as XRD and laser Raman spectroscopy showed that MnO_2 and Mn_2O_3 were formed on the surface of the catalyst with 10% Mn loading. The weight percent of MnO_2 and Mn_2O_3 were determined by XANES analysis to be 9.0 and 91.0%, respectively. Activity tests indicated that the catalyst deactivated at room temperature. It was observed that 65 ^{o}C was the minimum temperature, at which the catalyst worked without deactivation. The main cause of the catalyst deactivation was the accumulation of carbonaceous species on the surface of the catalyst due to the incomplete oxidation of toluene. FT-IR analysis identified alcohols and carboxylic acids as the deposited species on the surface of the catalyst. Near 95% toluene conversion was achieved at 80 ^{o}C with CO and CO_2 as the major reaction products, resulting in 90% carbon balance. The minor by-products of the reaction were determined to be oxalic acid, acetic acid, benzene, and maleic anhydride.

Chapter 5 studied the effect of Mn loading (1, 5, 10, and 20%) on the oxidation of toluene by ozone. X-ray absorption spectroscopy including XANES and EXAFS was used in order to relate the electronic properties and the structure of the catalysts to Mn loading. Results showed that the catalysts with Mn loading less than 10% mostly contained Mn_2O_3 while a mixture of MnO_2 and Mn_2O_3 was observed at higher Mn loading. It was also found that the formal oxidation state of Mn increased with the increase of catalyst loading. EXAFS studies were first carried out on the reference materials (MnO_2 and Mn_2O_3) in order to estimate the amplitude reduction factors (S_o^2). EXAFS of Mn_2O_3 was studied in more detail due to the complicated unit cell structure of Mn_2O_3. Two methods based on the Bond Valence Model and averaging the Mn sites based on their site occupancies were used to construct Mn_2O_3 theoretical EXAFS signal. Fitting the results showed that the Bond Valence Model and the averaging method converged on the same fitting parameters. In fact, the Bond Valence Model was considered as the general method to model the EXAFS signal of complex crystals such as Mn_2O_3. Nevertheless, the Bond Valence Model proved the validity of the averaging method, simplifying the structure of Mn_2O_3 into one single Mn sites. Activity tests showed that the catalysts with lower Mn loading and lower Mn oxidation state had higher rate of toluene oxidation. It was suggested that lower oxidation states of Mn were more favorable in the reaction. This observation was related to the fact that Mn atoms at lower oxidation states were more capable in transferring electrons to ozone, accelerating the rate of ozone decomposition which eventually enhanced the rate of toluene oxidation.

Promotional effect of the noble metals on activity of MnO_x/γ-alumina (10%) was studied in Chapter 6. Two noble metals with loading of 1% were added to manganese oxides to decrease the oxidation temperature of toluene. XANES and EXAFS were applied in order to elucidate

inter-atomic interactions between the noble metals and manganese oxides. Activity tests indicated that the addition of Pt increased the activity of MnO_x/γ-alumina (10%) by lowering the temperature of maximum toluene conversion to 70 ^oC. Pd did not improve the catalyst activity, resulting in maximum toluene conversion at 80 ^oC. The characterization of the catalysts showed that Pt is mostly in metallic state on alumina. The oxidation state of Pt increased after the addition of Pt to Mn, showing that an atomic interaction occurred between Pt and Mn. On the other hand, Pd was present as PdO in the presence and absence of Mn. Results of EXAFS also showed the changes in oxygen and Pt coordination numbers after the addition of Pt to Mn. No changes in EXAFS of Pd were observed after the addition of Pd to Mn, showing that most probably there is no interaction between Pd and Mn atoms. It was concluded that Pt was attached to manganese oxides through the surface oxygen atoms of Mn_2O_3 clusters, forming Pt-O-Mn bonds. It was suggested that the higher activity of Pt-Mn bimetallic catalyst was related to the electronic effect of Pt on Mn by increasing Mn 3d electron occupancy. This was in agreement with the effect of Mn loading, showing that lower oxidation states of Mn were more favorable in the oxidation of toluene. Activity of the reduced catalysts with hydrogen supported the idea that Mn atoms with less degree of oxidation were more effective in the oxidation of toluene.

The kinetics and mechanism of the catalytic oxidation of toluene by ozone over manganese oxides were studied in Chapter 7. Initial reaction rates were obtained in order to fit different kinetic models to the experimental data. Power law model determined the apparent activation energy of the reaction to be 31.0 kJ mol^{-1}, explaining the low temperature activity of the catalyst. Reaction orders with respect to toluene and ozone were -1 and 2, respectively. This suggested that toluene was oxidized faster at lower toluene partial pressures while reaction rates increased by the increase of ozone partial pressure. A Langmuir-Hinshelwood mechanism (LH1)

was considered in order to fit the experimental data. This model was originally developed by Oyama and co-workers in order to explain the mechanism of acetone oxidation by ozone over silica supported manganese oxides. LH1 showed that most likely peroxide species were not involved in the reaction mechanism due the low surface coverage of peroxide species. It was also observed that 2 oxygen atoms were necessary to start the oxidation reaction. However, the entropy of toluene adsorption turned out to be positive by LH1 mechanism. The positive value of the adsorption entropy is not recommended in catalytic reactions, indicating that LH1 mechanism could not completely explain the mechanism of the reaction. Therefore a second Langmuir-Hinshelwood mechanism (LH2) was proposed as an alternative to LH1 mechanism. LH2 mechanism was built based on the abstraction of one hydrogen atom from the methyl group by the adsorption of toluene on one pair of active sites. It was assumed that toluene molecule was dehydrogenated first by atomic oxygen to produce a hydrogen free carbon structure. The carbon structure further reacted with atomic oxygen to produce CO and CO_2. It was shown that LH2 mechanism resulted in a power law model with the reaction orders of -1 and 2 with respect to toluene and ozone, respectively. The reaction orders were the same as the power law model obtained from the experimental data, explaining the relationship of the actual reaction rates and LH2 mechanism. Nevertheless, the goal of Chapter 7 was to look at the mechanism of the reaction from a new angle, introducing alternative models which might justify the reaction mechanism. More evidence was obviously needed to fully understand the mechanism of this reaction which could be the subject of future works.

8.2. Conclusions

The followings are the general conclusions of the thesis based on the objectives defined in Chapter 2:

- The active phase of the catalyst (MnO_x/γ-alumina) is made of MnO_2 and Mn_2O_3 effective in the oxidation of toluene below 100 ^oC. The main by-products of the catalytic ozonation of toluene are CO and CO_2. Catalyst deactivation occurs at room temperature due to the accumulation of carbonaceous species on the catalyst. At least, 65 ^oC is required for the stable operation of the catalyst.
- EXAFS signal of Mn_2O_3 can be modeled using the Bond Valence Model, proposing a general approach for EXAFS analysis of transition metal oxides with more than one absorbing atom in their unit cell structure. A direct relationship exists between the oxidation state and the loading of manganese on alumina. Mn_2O_3 is the dominant phase at Mn loadings lower than 10% while more MnO_2 is formed at higher loadings. Lower Mn loadings are more favorable in the oxidation of toluene by ozone.
- EXAFS and XANES show that Pt is attached to manganese oxides through surface oxygen atoms of Mn_2O_3 clusters, changing the atomic environment around Mn. The net effect is the oxidation of Pt atoms and a slight increase in Mn coordination number, enhancing the oxidation rate of toluene by ozone. No atomic interaction is found between Pd and Mn, explaining why the addition of Pd does not promote the activity of Mn_2O_3 in the oxidation of toluene.
- It is concluded form the activity of different loadings of Mn and the addition of Pt to Mn that the catalytic oxidation of toluene can be promoted by decreasing the oxidation state of Mn. The bottleneck of the oxidation reaction seems to be the rate of ozone decomposition, controlling the overall rate of toluene oxidation.
- The kinetic study of the catalytic ozonation of toluene shows that the activation energy of toluene oxidation can be greatly reduced using ozone and MnO_x/γ-alumina.

This explains the low temperature activity of the catalyst comparing to that of oxygen which proceeds at around 200 ^{o}C. It is also proposed that the oxidation of toluene starts with the abstraction of hydrogen atoms and production of water. The mechanism is followed by the oxidation of the carbon skeleton of toluene, leading to the production of CO and CO_2.

8.3. Recommendations

Even though the result of this thesis and other works reported in the literature prove the effectiveness of catalytic ozonation, there are still open questions related to this method. Deactivation of the catalysts at room temperature is in fact a limiting factor for operating the catalyst at ambient temperature. It has been reported that the deactivation of manganese oxides in the oxidation of formaldehyde and benzene can be prevented in the presence of water vapor [60, 61]. The support type also plays an important role in the long term activity of catalysts. Einaga et al. showed that ultra stable Y (USY) zeolite was stable for the oxidation of benzene in the presence of water vapor at room temperature [22]. Therefore, it is recommended to investigate the effect of water vapor using different supports in order to obtain the room temperature activity of manganese oxides. Understanding the mechanism of catalyst deactivation at room temperature can also provide fundamental knowledge about the interaction of reaction by-products and the catalyst surface. This can explain the accumulation of carbonaceous species such as alcohols and carboxylic acids produced as the result of incomplete oxidation of toluene.

Studying the kinetics and mechanism of the reaction is another important research area which can be explored in more details. It was shown in Chapter 7 that different molecules most likely follow different elementary steps in the catalytic oxidation of VOCs by ozone. An alternative mechanism (LH2) was introduced to the widely used mechanism proposed by Oyama

and co-workers (LH1). LH2 mechanism was basically developed based on the activation of the adsorbed toluene molecule by dehydrogenation, following the oxidation of the carbon structure. In order to show the validity of LH2 mechanism over LH1 mechanism, it is possible to track the reaction rates at wider toluene partial pressures at a constant ozone partial pressure. Fig. 8.1 shows the trend of toluene oxidation rate predicted by LH1 and LH2 mechanisms as a function of toluene partial pressure.

It can be seen in Fig. 8.1 (A) that LH1 mechanism predicts zero reaction rates at toluene concentration close to zero. By the increase of toluene partial pressure, the reaction rates pass through a maximum and approach zero at high toluene partial pressures. On the other hand, Fig. 8.1 (B) shows the reaction rates predicted by LH2 mechanism. It can be seen that the reaction rate increases by the decrease of toluene partial pressure and reaches high values at toluene concentrations close to zero. Therefore, it is possible to check the validity of LH1 and LH2 mechanisms by tracking the reaction rates at low toluene partial pressures. This requires accurate analytical devices such as an on-line FT-IR gas analyzer which might become available in the future to test the validity of these mechanisms. In addition to this approach, it is also possible to study the validity of LH2 mechanism by other techniques such as isotopic exchange, density functional theory (DFT) calculations and *in-situ* spectroscopy to elucidate the elementary steps involved in the catalytic oxidation of VOCs by ozone.

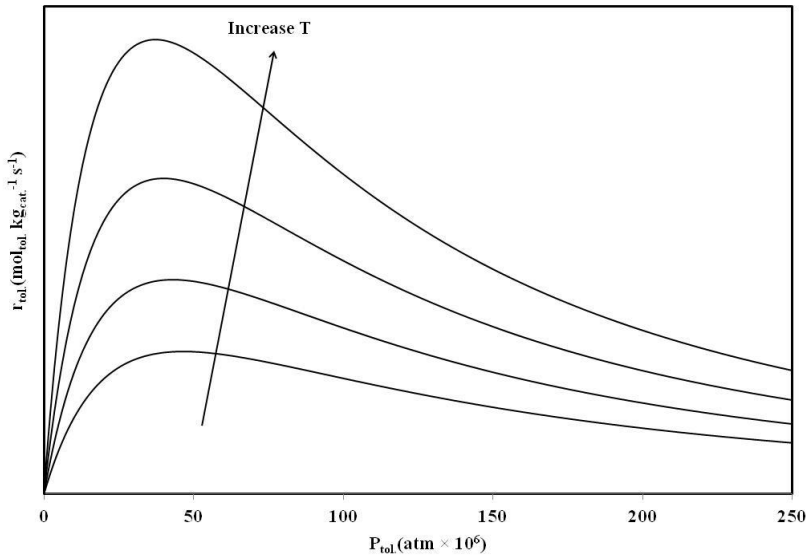

(A)

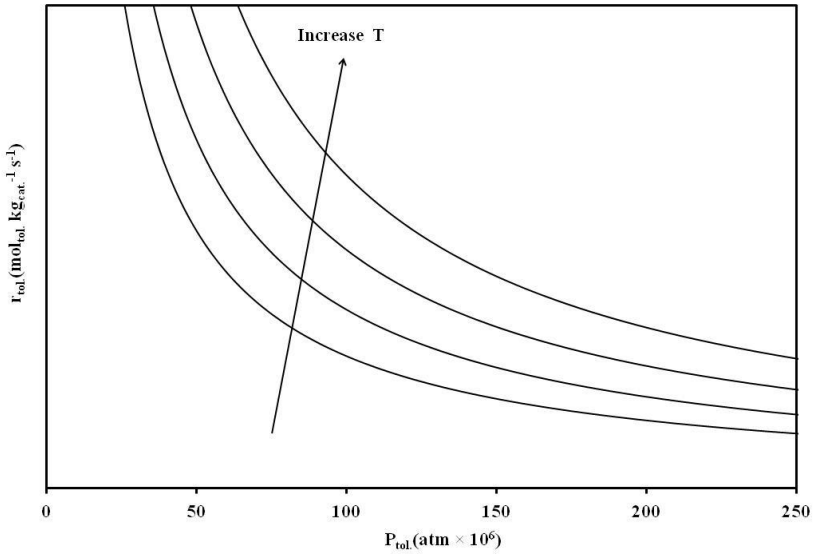

(B)

Fig. 8.1. Predicted reaction rates by (A) LH1 and (B) LH2 mechanisms.

Finally, technology development and reactor scale up can be considered if there is an industrial interest in this method. Catalytic ozonation can be integrated with HVAC systems as standalone units for the removal of VOCs from indoor environment. There is still need to explore

the effectiveness of this method in a real indoor air composition, consisting of a mixture of VOCs. Fine-tuning the reactions condition and the catalyst seems to be necessary for the treatment of actual air.

LIST OF REFERENCES

1. C.D. Cooper, F.C. Alley, Air Pollution Control; A design Approach, Third ed., Waveland Press, Inc., Prospect Heights, Illinois, United States of America, 2002.

2. T. Godish, Air Quality, First ed., Lewis Publisher, Inc., Michigan, The United States of America, 1986.

3. J.A. Hoskins, Health Effects due to Indoor Air Pollution, Indoor Built. Environ. 12 (2003) 427-433.

4. J. Namieśnik, T. Górecki, B. Kozdroń-Zabiega ła, J. Łukasiak, Indoor air quality (IAQ), pollutants, their sources and concentration levels, Build. Environ. 27 (1992) 339-356.

5. T. Godish, Indoor Environmetal Quality, First ed., CRC Press, The United States of America, 2001.

6. J. Zhang, K.R. Smith, Indoor air pollution: a global health concern, Br. Med. Bull. 68 (2003) 209-225.

7. C.J. Weschler, Changes in indoor pollutants since the 1950s, Atmos. Environ. 43 (2009) 153-169.

8. B.F. Yu, Z.B. Hu, M. Liu, H.L. Yang, Q.X. Kong, Y.H. Liu, Review of research on air-conditioning systems and indoor air quality control for human health, Int. J. Refrig. 32 (2009) 3-20.

9. S. Wang, H.M. Ang, M.O. Tade, Volatile organic compounds in indoor environment and photocatalytic oxidation: State of the art, Environ. Int. 33 (2007) 694-705.

10. W. Chen, J.S. Zhang, Z. Zhang, Performance of air cleaners for removing multiple volatile organic compounds in indoor air, ASHREA Transaction: Symposia (2005) 1101-1114.

11. B. Guieysse, C. Hort, V. Platel, R. Munoz, M. Ondarts, S. Revah, Biological treatment of indoor air for VOC removal: Potential and challenges, Biotechnol. Adv. 26 (2008) 398-410.

12. A. Gervasini, G.C. Vezzoli, V. Ragaini, VOC removal by synergic effect of combustion catalyst and ozone, Catal. Today 29 (1996) 449-455.

13. J.C. Wu, Z. Lin, F. Tsai, J. Pan, Low-temperature complete oxidation of BTX on Pt/activated carbon catalysts, Catal. Today 63 (2000) 419-426.

14. Q.-H. Xia, K. Hidajat, S. Kawi, Adsorption and catalytic combustion of aromatics on platinum-supported MCM-41 materials, Catal. Today 68 (2001) 255-262.

15. S. Baek, J. Kim, S. Ihm, Design of dual functional adsorbent/catalyst system for the control of VOC's by using metal-loaded hydrophobic Y-zeolites, Catal. Today 93-95 (2004) 575-581.

16. S. Huang, C. Zhang, H. He, Complete oxidation of o-xylene over Pd/Al_2O_3 catalyst at low temperature, Catal. Today 139 (2008) 15-23.

17. S.T. Oyama, Chemical and Catalytic Properties of Ozone, Catal. Rev. Sci. Eng. 42 (2000) 279-322.

18. W. Li, S. Ted Oyama, Ethanol oxidation using ozone over supported manganese oxide catalysts: An in situ laser Raman study, in: Stud. Surf. Sci. Catal., Elsevier, 1997, pp. 873-882.

19. M. Stoyanova, P. Konova, P. Nikolov, A. Naydenov, S. Christoskova, D. Mehandjiev, Alumina-supported nickel oxide for ozone decomposition and catalytic ozonation of CO and VOCs, Chem. Eng. J. 122 (2006) 41-46.

20. Y. Xi, C. Reed, Y.-.K. Lee, S.T. Oyama, Acetone oxidation using ozone on manganese oxide catalysts, J. Phys. Chem. B 109 (2005) 17587-17596.

21. H. Einaga, S. Futamura, Oxidation behavior of cyclohexane on alumina-supported manganese oxides with ozone, Appl. Catal. B 60 (2005) 49-55.

22. H. Einaga, Y. Teraoka, A. Ogat, Benzene oxidation with ozone over manganese oxide supported on zeolite catalysts, Catal. Today 164 (2011) 571-574.

23. H.C. Wang, H.S. Liang, M.B. Chang, Ozone-enhanced catalytic oxidation of monochlorobenzene over iron oxide catalysts, Chemosphere 82 (2011) 1090-1095.

24. H.C. Wang, H.S. Liang, M.B. Chang, Chlorobenzene oxidation using ozone over iron oxide and manganese oxide catalysts, J. Hazard. Mater. 186 (2011) 1781-1787.

25. M. Li, K.N. Hui, K.S. Hui, S.K. Lee, Y.R. Cho, H. Lee, W. Zhou, S. Cho, C.Y.H. Chao, Y. Li, Influence of modification method and transition metal type on the physicochemical properties of MCM-41 catalysts and their performances in the catalytic ozonation of toluene, Appl. Catal. B 107 (2011) 245-252.

26. E. Rezaei, J. Soltan, N. Chen, Catalytic oxidation of toluene by ozone over alumina supported manganese oxides: Effect of catalyst loading, Appl. Catal. B 136–137 (2013) 239-247.

27. D. Zhao, C. Shi, X. Li, A. Zhu, B.W.-L. Jang, Enhanced effect of water vapor on complete oxidation of formaldehyde in air with ozone over MnOx catalysts at room temperature, J. Hazard. Mater. 239–240 (2012) 362-369.

28. B. Dhandapani, S.T. Oyama, Gas Phase ozone decomposition catalysts, Appl. Catal. B 11 (1997) 129-166.

29. C. Reed, Y.-.K. Lee, S.T. Oyama, Structure and oxidation state of silica-supported manganese oxide catalysts and reactivity for acetone oxidation with ozone, J. Phys. Chem. B 110 (2006) 4207-4216.

30. P. Brimblecombe, M. Cashmore, Indoor air polluion, J. Phys. IV France 121 (2004) 209-221.

31. P. Wolkoff, G.D. Nielsen, Organic compounds in indoor air—their relevance for perceived indoor air quality?, Atmos. Environ. 35 (2001) 4407-4417.

32. A.P. Jones, Indoor air quality and health, Atmos. Environ. 33 (1999) 4535-4564.

33. J. Mo, Y. Zhang, Q. Xu, J.J. Lamson, R. Zhao, Photocatalytic purification of volatile organic compounds in indoor air: A literature review, Atmos. Environ. 43 (2009) 2229-2246.

34. J. Van Durme, J. Dewulf, W. Sysmans, C. Leys, H. Van Langenhove, Efficient toluene abatement in indoor air by a plasma catalytic hybrid system, Appl. Catal. B 74 (2007) 161-169.

35. J. Van Durme, J. Dewulf, C. Leys, H. Van Langenhove, Combining non-thermal plasma with heterogeneous catalysis in waste gas treatment: A review, Appl. Catal. B 78 (2008) 324-333.

36. F. Holzer, U. Roland, F.-. Kopinke, Combination of non-thermal plasma and heterogeneous catalysis for oxidation of volatile organic compounds: Part 1. Accessibility of the intra-particle volume, Appl. Catal. B 38 (2002) 163-181.

37. X. Fan, T.L. Zhu, M.Y. Wang, X.M. Li, Removal of low-concentration BTX in air using a combined plasma catalysis system, Chemosphere 75 (2009) 1301-1306.

38. J. Van Durme, J. Dewulf, K. Demeestere, C. Leys, H. Van Langenhove, Post-plasma catalytic technology for the removal of toluene from indoor air: Effect of humidity, Appl. Catal. B 87 (2009) 78-83.

39. M.F. Boeniger, Use of Ozone Generating Devices to improve Indoor Air Quality, Am. Ind. Hyg. Assoc. J. 56 (1995) 590-598.

40. F.j. Beltran., Ozone Reaction Kinetics for Water and Wastewater Systems, 1st ed., CRC Press LLC, United States of America, 2003.

41. A. Naydenov, D. Mehandjiev, Complete oxidation of benzene on manganese dioxide by ozone, Appl. Catal. A 97 (1993) 17-22.

42. D. Mehandjiev, E. Zhecheva, G. Ivanov, R. Ioncheva, Preparation and catalytic activity of nickel–manganese oxide catalysts with an ilmenite-type structure in the reactions of complete oxidation of hydrocarbons, Appl. Catal. A 167 (1998) 277-282.

43. D. Mehandjiev, A. Naydenov, G. Ivanov, Ozone decomposition, benzene and CO oxidation over $NiMnO_3$-ilmenite and $NiMn_2O_4$-spinel catalysts, Appl. Catal. A 206 (2001) 13-18.

44. D. Mehandjiev, K. Cheshkova, A. Naydenov, V. Georgesku, Catalytic oxidation of CO and C_6H_6 on alumina supported Cu-Cr and Co-Cr oxide catalysts in the presence of ozone, React. Kinet. Catal. Lett. 76 (2002) 287-293.

45. P. Konova, M. Stoyanova, A. Naydenov, S. Christoskova, D. Mehandjiev, Catalytic oxidation of VOCs and CO by ozone over alumina supported cobalt oxide, Appl. Catal. A 298 (2006) 109-114.

46. B. Dhandapani, S.T. Oyama, Kinetics and Mechanism of Ozone Decomposition on a Manganese oxide Catalyst, Chem. Lett. 24 (1995) 413-414.

47. W. Li, G.V. Gibbs, S.T. Oyama, Mechanism of ozone decomposition on a manganese oxide catalyst. 1. In Situ Raman spectroscopy and Ab Initio molecular orbital calculations, J. Am. Chem. Soc. 120 (1998) 9041-9046.

48. W. Li, S.T. Oyama, Mechanism of ozone decomposition on a manganese oxide catalyst. 2. Steady-state and transient kinetic studies, J. Am. Chem. Soc. 120 (1998) 9047-9052.

49. R. Radhakrishnan, S.T. Oyama, Ozone decomposition over manganese oxide supported on ZrO_2 and TiO_2: A kinetic study using in Situ laser Raman spectroscopy, J. Catal. 199 (2001) 282-290.

50. R. Radhakrishnan, S.T. Oyama, J.G. Chen, K. Asakura, Electron transfer effects in ozone decomposition on supported manganese oxide, J. Phys. Chem. B 105 (2001) 4245-4253.

51. C. Reed, Y. Xi, S.T. Oyama, Distinguishing between reaction intermediates and spectators: A kinetic study of acetone oxidation using ozone on silica-supported manganese oxide catalyst, J. Catal. 235 (2005) 378-392.

52. H. Einaga, S. Futamura, Comparative study on the catalytic activities of alumina-supported metal oxides for oxidation of benzene and cyclohexane with ozone, React. Kinet. Catal. Lett. 81 (2004) 121-128.

53. H. Einaga, S. Futamura, Catalytic oxidation of benzene with ozone over alumina-supported manganese oxides, J. Catal. 227 (2004) 304-312.

54. H. Einaga, S. Futamura, Catalytic oxidation of benzene with ozone over Mn ion-exchanged zeolites, Catal. Commun. 8 (2007) 557-560.

55. H. Einaga, M. Harada, A. Ogata, Relationship between the structure of manganese oxides on alumina and catalytic activities for benzene oxidation with ozone, Catal. Lett. 129 (2009) 422-427.

56. H. Einaga, A. Ogata, Benzene oxidation with ozone over supported manganese oxide catalysts: Effect of catalyst support and reaction conditions, J. Hazard. Mater. 164 (2009) 1236-1241.

57. H. Einaga, A. Ogata, Catalytic oxidation of benzene in the gas phase over alumina-supported silver catalysts, Environ. Sci. Technol 44 (2010) 2612-2617.

58. H. Einaga, Y. Teraoka, A. Ogata, Catalytic oxidation of benzene by ozone over manganese oxides supported on USY zeolite, J. Catal. 305 (2013) 227-237.

59. H. Einaga, N. Maeda, Y. Teraoka, Effect of catalyst composition and preparation conditions on catalytic properties of unsupported manganese oxides for benzene oxidation with ozone, Appl. Catal. B 142–143 (2013) 406-413.

60. H. Einaga, S. Futamura, Effect of water on catalytic oxidation of benzene with ozone on alumina-supported manganese oxides, J. Catal. 243 (2006) 446-450.

61. D. Zhao, C. Shi, X. Li, A. Zhu, B.W.-L. Jang, Enhanced effect of water vapor on complete oxidation of formaldehyde in air with ozone over MnO_x catalysts at room temperature, J. Hazard. Mater. 239-240 (2012) 362-369.

62. Z. Hao, D. Cheng, Y. Guo, Y. Liang, Supported gold catalysts used for ozone decomposition and simultaneous elimination of ozone and carbon monoxide at ambient temperature, Appl. Catal. B 33 (2001) 217-222.

63. M. Petersson, D. Jonsson, H. Persson, N. Cruise, B. Andersson, Ozone promoted carbon monoxide oxidation on platinum/γ-alumina catalyst, J. Catal. 238 (2006) 321-329.

64. M. Yuan, C. Chang, J. Shie, C. Chang, J. Chen, W. Tsai, Destruction of naphthalene via ozone-catalytic oxidation process over Pt/Al_2O_3 catalyst, J. Hazard. Mater. 175 (2010) 809-815.

65. P. Monneyron, M.-.H. Manero, S. Mathe, A combined selective adsorption and ozonation process for VOCs removal from air, Can. J. Chem. Eng. 85 (2007) 326-332.

66. C.Y.H. Chao, C.W. Kwong, K.S. Hui, Potential use of a combined ozone and zeolite system for gaseous toluene elimination, J. Hazard. Mater. 143 (2007) 118-127.

67. C.W. Kwong, C.Y.H. Chao, K.S. Hui, M.P. Wan, Catalytic Ozonation of Toluene Using Zeolite and MCM-41 Materials, Environ. Sci. Technol. 42 (2008) 8504-8509.

68. C.W. Kwong, C.Y.H. Chao, K.S. Hui, M.P. Wan, Removal of VOCs from indoor environment by ozonation over different porous materials, Atmos. Environ. 42 (2008) 2300-2311.

69. M. Sugasawa, A. Ogata, Effect of different combination of metal and zeolite on ozone-assisted catalysis for toluene removal, Ozone: Sci. Eng. 33 (2011) 158-163.

70. E. Park, S. Chin, J. Kim, G.-.N. Bae, J. Jurng, Preparation of MnO_x/TiO_2 ultra fine nanocomposite with large surface area and its enhanced toluene oxidation at low temperature, Powder Technol. 208 (2011) 740-743.

71. L. Long, J. Zhao, L. Yang, M. Fu, J. Wu, B. Huang, D. Ye, Room Temperature Catalytic Ozonation of Toluene over MnO_2/Al_2O_3, Chin. J. Catal. 32 (2011) 904-916.

72. S.M. Saqer, D.I. Kondarides, X.E. Verykios, Catalytic activity of supported platinum and metal oxide catalysts for toluene oxidation, Top. Catal. 52 (2009) 517-527.

73. T. Garcia, B. Solsona, D. Cazorla-Amorós, Á. Linares-Solano, S.H. Taylor, Total oxidation of volatile organic compounds by vanadium promoted palladium-titania catalysts: Comparison of aromatic and polyaromatic compounds, Appl. Catal. B 62 (2006) 66-76.

74. B. Grbic, N. Radic, B. Markovic, P. Stefanov, D. Stoychev, T. Marinova, Influence of manganese oxide on the activity of Pt/Al_2O_3 catalyst for CO and n-hexane oxidation, Appl. Catal. B 64 (2006) 51-56.

75. D.T. Jiang, N. Chen, W. Sheng, Wigglerbase Hard Xray Spectroscopy Beamline at CLS, AIP Conf. Proc. 879 (2007) 800-803.

76. B. Ravel, M. Newville, ATHENA, ARTEMIS, HEPHAESTUS: data analysis for X-ray absorption spectroscopy using IFEFFIT, J. synchrotron radiat. 12 (2005) 537-541.

77. J.J. Rehr, R.C. Alber, Theoretical approaches to x-ray absorption fine structure, Rev. Mod. Phys. 72 (2000) 621-654.

78. M. Newville, IFEFFIT: interactive EXAFS analysis and FEFF fitting, J. synchrotron radiat. 8 (2001) 322-324.

79. B. Ravel, EXAFS Analysis with FEFF and FEFFIT, Part 2: Commentary (2001).

80. Mineral Powder Diffraction File Data book: Sets 1-42 (1993).

81. J.W. Niemantsverdriet, Spectroscopy in Catalysis, Third ed., WILEY-VCH Verlag GmbH & Co. KGaA, Weinheim, 2007.

82. C. Reed, VOC Catalytic Oxidation on Manganese Oxide Catalysts Using Ozone, PhD Thesis, Virginia Polytechnic Institute and State University (2005).

83. F. Buciuman, F. Patcas, R. Craciun, D.R.T. Zahn, Vibrational spectroscopy of bulk and supported manganese oxides, Phys. Chem. Chem. Phys. (1999) 185-190.

84. F. Kapteijn, A.D. Vanlangeveld, J.A. Moulijn, A. Andreini, M.A. Vuurman, A.M. Turek, J.M. Jehng, I.E. Wachs, Alumina-Supported Manganese Oxide Catalysts: I. Characterization: Effect of Precursor and Loading, J. Catal. 150 (1994) 94-104.

85. M. Ferrandon, J. Carno, S. Jaras, E. Bjornbom, Total oxidation catalysts based on manganese or copper oxides and platinum or palladium I: Characterisation, Appl. Catal. A 180 (1999) 141-151.

86. A. Longo, F.L. Liotta, G. Di Carlo, F. Giannici, A.M. Venezia, A. Martorana, Structure and the Metal Support Interaction of the Au/Mn Oxide Catalyst, Chem. Mater. 22 (2010) 3952-3960.

87. A.K.S. Sinha K., M. Takahara, H. Azuma, T. Nonaka, N. Suzuki, N. Takahashi, Preparation and Characterization of Mesostructured γ-Manganese Oxide and Its Application to VOCs Elimination, J. Phys Chem. C 112 (2008) 16028-16035.

88. A.K.S. Sinha K., M. Takahara, H. Azuma, T. Nonaka, K. Fukumoto, Mesostructured Manganese Oxide/Gold Nanoparticle Composites for Extensive Air Purification, Angew. Chem. Int. Ed. 46 (2007) 2891-2894.

89. S.D. Kelly, D. Hesterberg, B. Ravel, Analysis of soils and minerals using X-ray absorption spectroscopy, in: Methods of soil analysis, Part 5 -Mineralogical methods, Soil Science Society of America, Inc, Madison, WI, USA, 2008, pp. 387-463.

90. M. Newville, Fundamentals of XAFS, XAFS. ORG (2004) 1-40.

91. J.J. Rehr, A. Ankudinov, S.I. Zabinsky, New developments in NEXAFS/EXAFS theory, Catal. Today 39 (1998) 263-269.

92. D.C. Koningsberger, B.L. Mojet, G.E. van Dorssen, D.E. Ramaker, XAFS spectroscopy; fundamental principles and data analysis, Top. Catal. 10 (2000) 143-155.

93. J. Yano, V.K. Yachandra, X-ray absorption spectroscopy, Photosynth. Res. 102 (2009) 241-254.

94. M. Newville, IFEFFIT: interactive XAFS analysis and FEFF fitting, J. synchrotron radiat. 8 (2001) 322-324.

95. M. Newville, Using Bond Valence Sums as Restraints in XAFS Analysis, Phys. Scr. T115 (2005) 159-161.

96. I.D. Brown, D. Altermatt, Bond-Valence Parameters Obtained from a Systematic Analysis of the Inorganic Crystal Structure Database, Acta. Cryst. B41 (1985) 244-247.

97. D.L. Pavia, G.M. Lampman, G.S. Kriz, J.R. Vyvyan, Introduction to Spectroscopy (2009).

98. E. Rezaei, J. Soltan, Low temperature oxidation of toluene by ozone over MnO_x/γ-alumina and MnO_x/MCM-41 catalysts, Chem. Eng. J. 198–199 (2012) 482-490.

99. D. Andreeva, T. Tabakova, L. Ilieva, A. Naydenov, D. Mehandjiev, M.V. Abrashev, Nanosize gold catalysts by vanadium oxide supported on titania and zirconia for complete benzene oxidation, Appl. Catal. A 209 (2001) 291-300.

100. M.C. Alvarez-Galvan, de la Pena O'Shea, V.A., J.L.G. Fierro, P.L. Arias, Aluminum-supported manganese and manganese-palladium oxide catalysts for VOCs combustion, Catal. Commun. 4 (2003) 223-228.

101. M.C. Alvarez-Galvan, B. Pawelec, de la Pena O'Shea, V.A., J.L.G. Fierro, P.L. Arias, Formaldehyde/methanol combustion on alumina-supported manganese-palladium oxide catalyst, Appl. Catal. B 51 (2004) 83-91.

102. de la Pena O'Shea, V.A., M.C. Alvarez-Galvan, J.L.G. Fierro, P.L. Arias, Influence of feed composition on the activity of Mn and PdMn/Al_2O_3 catalysts for combustion of formaldehyde/methanol, Appl. Catal. B 57 (2005) 191-199.

103. F. N. Aguero, B. P. Barbero, M.F. R. Pereira, J.L. Fiueiredo, L.E. Cadus, Mixed platinum-manganese oxide catalysts for combustion of volatile organic compounds, Ind. Eng. Chem. Res. 48 (2009) 2795-2800.

104. J. Carno, M. Ferrandon, E. Bjornbom , S. Jaras, Mixed manganese oxied/platinum catalysts for total oxidation of model gas from wood boilers, Appl. Catal. A 155 (1997) 265-281.

105. M. Ferrandon, J. Carnö, S. Järås, E. Björnbom, Total oxidation catalysts based on manganese or copper oxides and platinum or palladium I: Characterisation, Appl. Catal. A 180 (1999) 141-151.

106. L. Wang, C. Huang, C. Chang, W. Lin, K. Chao, Formation of Pd nanoparticles in surfactant-mesoporous silica composites and surfactant solutions, Microporous and Mesoporous Mater. 110 (2008) 451-460.

107. K.J. Stevens, B. Ingham, M.F. Toney, S.A. Brown, A. Lassesson, Structure of palladium nanoclusters for hydrogen gas sensors, Curr. Appl. Phys. 8 (2008) 443-446.

108. M. Pan, J.M. Cowley, The structure of Pt particles on γ-Al_2O_3 support, J. Appl. Cryst. 20 (1987) 300-305.

109. S. Schneider, D. Bazin, F. Garin, G. Maire, M. Capelle, G. Meunier, R. Noirot, NO reaction over nanometer scale platinum clusters deposited on γ-alumina: an XAS study, Appl. Catal. A 189 (1999) 139-145.

110. V.A. de la Peña O'Shea, M.C. Alvarez-Galvan, J. Requies, V.L. Barrio, P.L. Arias, J.F. Cambra, M.B. Güemez, J.L.G. Fierro, Synergistic effect of Pd in methane combustion $PdMnO_x/Al_2O_3$ catalysts, Catal. Commun. 8 (2007) 1287-1292.

111. S. Hosokawa, M. Taniguchi, K. Utani, H. Kanai, S. Imamura, Affinity order among noble metals and CeO_2, Appl. Catal. A 289 (2005) 115-120.

112. M.P. Heynderickx, J.W. Thybaut, H. Poelman, D. Poelman, G.B. Marin, Kinetic modeling of the total oxidation of propane over $CuO\text{-}CeO_2/\gamma\text{-}Al_2O_3$, Appl. Catal. B 95 (2010) 26-38.

113. A.M. Brown, A step-by-step guide to non-linear regression analysis of experimental data using a Microsoft Excel spreadsheet, Comput. Methods Programs Biomed. 65 (2001) 191-200.

114. G.F. Froment, K.B. Bischoff, J. De Wilde, Chemical Reactor Analysis and design, 3rd ed., John Wiley & Sons, Inc., United States of America, 2011.

115. J. Bedia, J.M. Rosas, J. Rodríguez-Mirasol, T. Cordero, Pd supported on mesoporous activated carbons with high oxidation resistance as catalysts for toluene oxidation, Appl. Catal. B 94 (2010) 8-18.

116. S. Toby, L.J. Van de Burgt, F.S. Toby, Kinetics and chemiluminescence of ozone-aromatic reactions in the gas phase, J. Phys Chem. 89 (1985) 1982-1986.

117. M.A. Vannice, Kinetics of Catalytic Reactions, 1st ed., Springer, United States of America, 2005.

118. S.L.T. Andersson, Reaction networks in the catalytic vapor-phase oxidation of toluene and xylenes, J. Catal. 98 (1986) 138-149.

119. G. Busca, F. Cavani, F. Trifirò, Oxidation and ammoxidation of toluene over vanadium-titanium oxide catalysts: A Fourier transform infrared and flow reactor study, J. Catal. 106 (1987) 471-482.

120. B. Irigoyen, A. Juan, S. Larrondo, N. Amadeo, The adsorption of toluene on V–Sb oxides. Theoretical aspects, Surf. Sci. 523 (2003) 252-266.

121. Y.-H. Chin, C. Buda, M. Neurock, E. Iglesia, Reactivity of Chemisorbed Oxygen Atoms and Their Catalytic Consequences during CH4–O_2 Catalysis on Supported Pt Clusters, J. Am. Chem. Soc. 133 (2011) 15958-15978.

122. M. García-Diéguez, Y.-H. Chin, E. Iglesia, Catalytic reactions of dioxygen with ethane and methane on platinum clusters: Mechanistic connections, site requirements, and consequences of chemisorbed oxygen, J. Catal. 285 (2012) 260-272.

123. U. Menon, V.V. Galvita, G.B. Marin, Reaction network for the total oxidation of toluene over $CuO–CeO_2/Al_2O_3$, J. Catal. 283 (2011) 1-9.

124. H.S. Fogler, Elements of Chemical Reaction Engineering, 2nd ed., Prentice-Hall Inc. A Simon & Schuster Company, Upper Saddle River, NJ 07458, 1992.

APPENDIX A: GC-MS CALIBRATION DATA

Tables A.1 to A.3 contain the TIC peak area at each toluene, CO, and CO_2 concentrations, respectively. Measurements were repeated three times. Figures A.1 to A.3 show the GC-MS calibration curves of toluene, CO, and CO_2, respectively.

Table A.1. Toluene TIC peak area

Toluene Concentration (ppm)	Peak Area	Average	Standard Deviation
0	0 0 0	0	0
30	7582078 8150093 7922682	7884951	285881
90	24341002 26313710 25826375	25493696	1027570
150	41562510 43210098 43169525	42647378	939742
270	74333456 74942023 74651025	74642168	304380

Table A.2. CO TIC peak area

CO (ppm)	Peak Area	Average	Standard Deviation
0	0	0	0
	0		
	0		
70	147947	145438	4269
	140509		
	147858		
210	451161	456939	5680
	457141		
	462515		
350	802245	808464	5401
	811977		
	811171		
630	1494342	1518051	29145
	1550589		
	1509221		

Table A.3. CO_2 TIC peak area

CO_2 (ppm)	Peak Area	Average	Standard Deviation
0	0	0	0
	0		
	0		
68	643949	657777	31421
	693741		
	635642		
204	2048713	2053549	22370
	2033993		
	2077941		
340	3536519	3587814	100677
	3523116		
	3703808		
612	6518239	6649503	130394
	6779009		
	6651262		

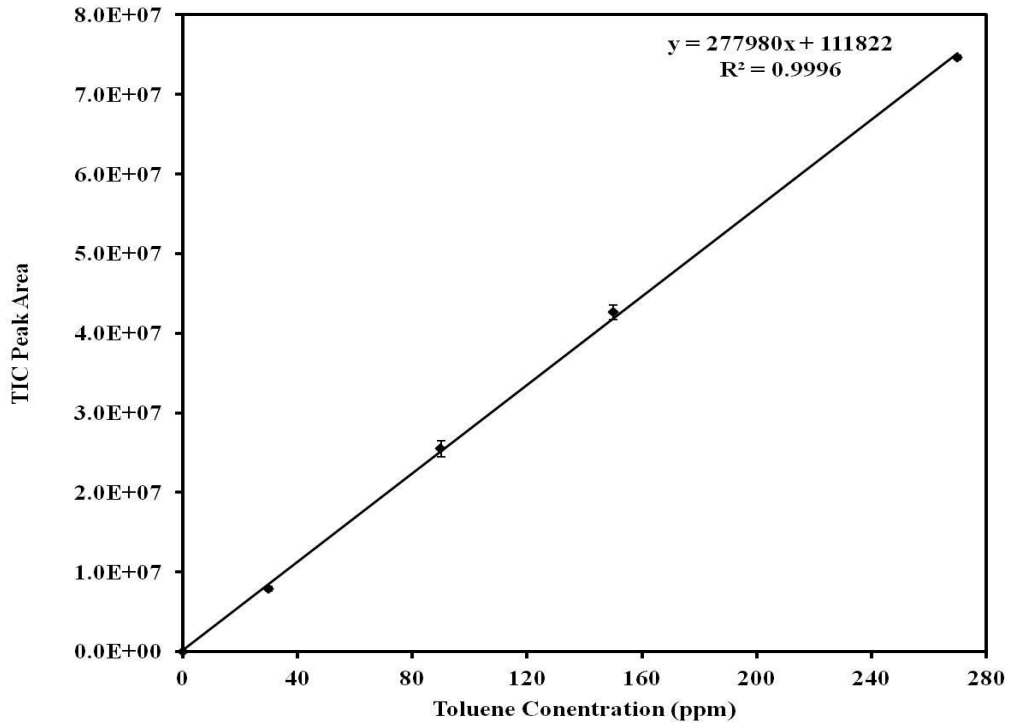

Fig. A.1. Toluene calibration curve; error bars are standard deviations.

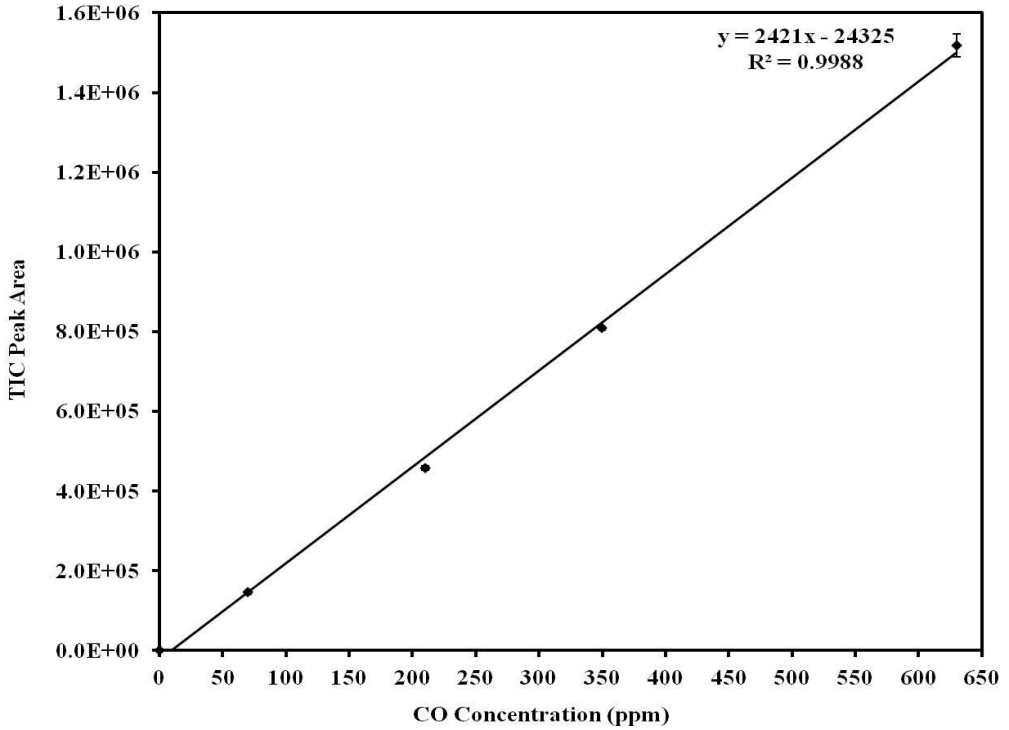

Fig. A.2. CO calibration curve; error bars are standard deviations.

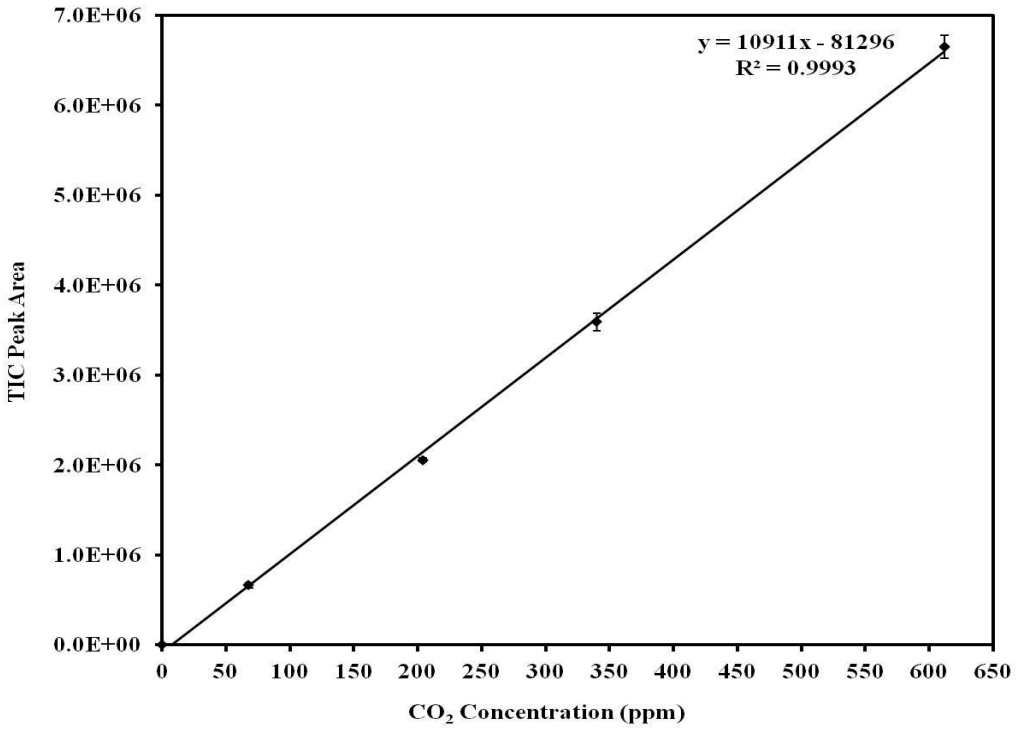

Fig. A.3. CO_2 calibration curve; error bars are standard deviations.

APPENDIX B: EFFECT OF PARTICLE SIZE ON THE CATALYST ACTIVITY

0.2 g of MnO_x/γ-alumina (10%) with different particle sizes (dp) of dp<80 μm, 80 μm< dp<208 μm, 208 μm< dp< 355 μm and 355 μm< dp<417 μm were tested in the temperature range of 22-100 ^oC to select the appropriate particle size which did not impose internal mass transfer limitation on the reaction rate. The flow rate of toluene/nitrogen and ozone/oxygen streams were 400 and 600 ml min^{-1}, respectively which resulted in a weight hour space velocity (WHSV) of 300 l hr^{-1} g^{-1}. This combination gave toluene and ozone concentration of 120 and 1050 ppm, respectively. The mole percent of oxygen and nitrogen were 59.94 and 39.94%, respectively.

Activity of the catalyst with different particle size ranges are shown in Fig. B.1. Results show that by the increase of particle size to higher than 208 μm, the activity of the catalyst in toluene oxidation decreases. Therefore, it is decided to use a particle size with diameter less than 208 μm for the reaction rate studies.

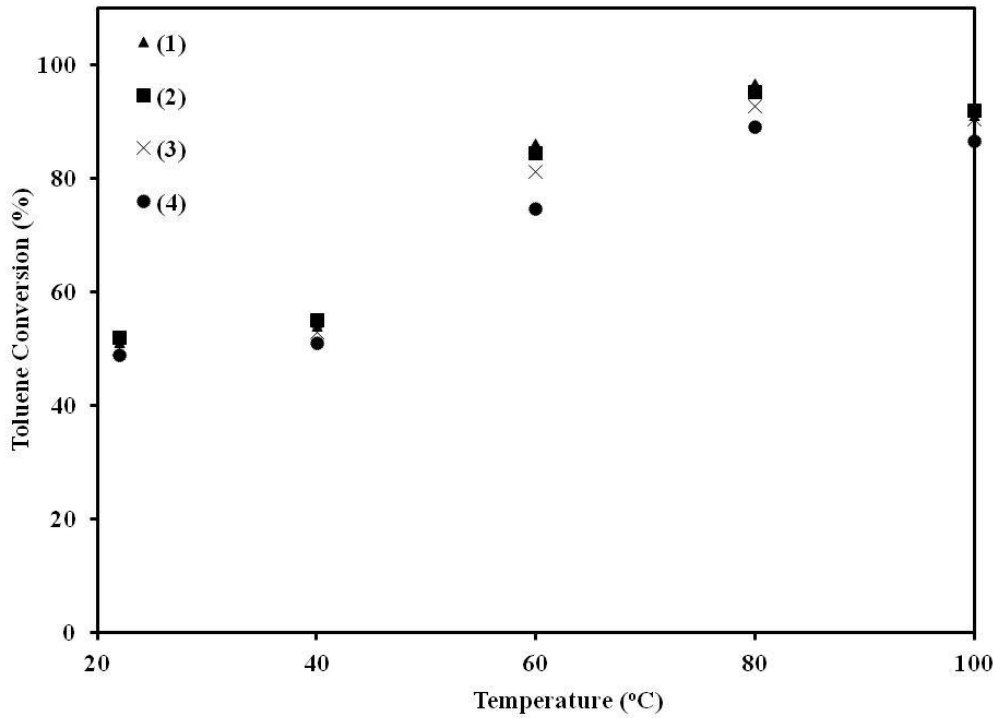

Fig. B.1. Effect of particle size (d_p) on activity of MnO_x/γ-alumina (10%), (1) d_p<80 μm, (2) 80 μm< d_p<208 μm, (3) 208 μm< d_p< 355 μm, (4) 355 μm< d_p<417 μm.

APPENDIX C: MEAR'S CRITERION FOR EXTERNAL MASS TRANSFER

Mear's equation can be expressed as [124]:

$$\frac{-r_A^{'}\rho_b Rn}{k_c C_A} < 0.15 \qquad \text{(C.1)}$$

in which,

n = reaction order

R = radius of the catalyst particle (m)

ρ_b = catalyst bed bulk density (kg m^{-3})

C_A = concentration of A in the gas phase (kg mol m^{-3})

$r_A^{'}$ = reaction rate of A (kg mol kg^{-1} s^{-1})

k_c = external mass transfer coefficient (m s^{-1})

k_c around a spherical particle can be estimated by [124]:

$$Sh = 2 + 0.6\, Re^{1/2} Sc^{1/3} \qquad \text{(C.2)}$$

Sherwood number (Sh), Schmidt number (Sc), and Reynolds number (Re) are expressed by equations (C.3), (C.4), and (C.5), respectively:

$$Sh = \frac{k_c d_p}{D_{AB}} \qquad \text{(C.3)}$$

$$Sc = \frac{\mu_g}{\rho_g D_{AB}} \qquad \text{(C.4)}$$

$$Re = \frac{U \rho_g d_p}{\mu_g} \qquad \text{(C.5)}$$

d_p (m) and D_{AB} (m^2 s^{-1}) are the particle diameter and the diffusivity coefficient of A in B, respectively. μ_g is the viscosity of the gas phase in kg m^{-1} s^{-1}. U is superficial velocity in m s^{-1}. ρ_g represents the gas phase density in kg m^{-3}.

The following information is used as the typical conditions of the reactor to examine the effect of the external mass transfer:

Gas composition: 40% nitrogen and 60% oxygen

Total gas flow rate: 1000 ml min^{-1}

Reactor internal diameter: 1/4 in

Temperature: 60 ^oC

Gas viscosity (μ_g): 2.1×10^{-5} kg m^{-1} s^{-1}

Gas density (ρ_g): 1.1 kg m^{-3}

Catalyst particle diameter (d_p): 208×10^{-6} m

Toluene diffusivity coefficient (D_{AB}): 9.9×10^{-6} m^2 s^{-1}

Using the above information along with Eq. (C.2) to (C.5), one can show that the external mass transfer coefficient can be found as 0.18 m^2 s^{-1}.

The conversion of toluene over 0.2 g of the catalyst at 60 ^oC is about 80% for the inlet toluene concentration of 120 ppm. Therefore, it is reasonable to assume an average toluene concentration of 70 ppm (2.6×10^{-6} kg mol m^{-3}) at 60 ^oC inside the reactor. For 80% toluene conversion with the inlet toluene concentration of 120 ppm, the average rate of the reaction is 3.3×10^{-7} kg mol kg^{-1} s^{-1}. By considering the reaction order of one with respect to toluene and bulk density of 500 kg m^{-3} for the catalyst bed, the Mear's criterion is satisfied as $0.037<0.15$, showing that external mass transfer does not control the rate of toluene oxidation.

APPENDIX D: RAW DATA OF THE CATALYTIC OXIDATION OF TOLUENE BY OZONE

Toluene was oxidized over 0.2 g of MnO_x/γ-alumina (10%) and the experiment was repeated in order to evaluate the repeatability of the data. Inlet concentration of toluene and ozone were 120 and 1050 ppm, respectively. Reaction conditions have been presented in section 3.3. Tables D.1 and D.2 represent the concentrations and conversions of toluene and ozone at room temperature, respectively. Concentrations and conversions of toluene and ozone at higher temperature are included in Tables D.3 and D.4, respectively.

Table D.1. Toluene concentration and conversion at room temperature

		Time (min)				
		6	41	76	118	150
Outlet toluene concentration (ppm)	Run #1	1	14	37	53	65
	Run #2	1	17	35	50	61
	Average (ppm)	1	16	36	51	63
	Standard deviation (ppm)	0	2	2	2	3
Toluene conversion (%)	Run #1	99	88	69	56	46
	Run #2	99	86	71	58	50
	Average (%)	99	87	70	57	48
	Standard deviation (%)	0	1	2	2	3

Table D.2. Ozone concentration at conversion at room temperature

		Time (min)				
		6	41	76	118	150
Outlet ozone concentration (ppm)	Run #1	0	285	553	700	800
	Run #2	30	300	515	670	770
	Average (ppm)	15	293	534	685	785
	Standard deviation (ppm)	2	11	27	21	21
Ozone conversion (%)	Run #1	100	73	47	33	24
	Run #2	97	71	51	36	27
	Average (%)	99	72	49	35	25
	Standard deviation (%)	2	1	3	2	2

Table D.3. Toluene concentration and conversions at higher temperatures

		Temperature (^{o}C)			
		40	60	80	100
Outlet toluene concentration (ppm)	Run #1	59	18	10	10
	Run #2	54	23	7	8
	Average (ppm)	56	20	9	9
	Standard deviation (ppm)	4	4	2	1
Toluene conversion (%)	Run #1	51	85	92	92
	Run #2	55	81	94	93
	Average (%)	53	83	93	93
	Standard deviation (%)	3	3	2	1

Table D.4. Ozone concentration and conversion at higher temperatures

		Temperature (°C)			
		40	60	80	100
Outlet ozone concentration (ppm)	Run #1	685	239	0	0
	Run #2	695	259	53	0
	Average (ppm)	690	249	26	0
	Standard deviation (ppm)	7	14	37	0
Ozone conversion (%)	Run #1	35	77	100	100
	Run #2	34	75	95	100
	Average (%)	34	76	98	100
	Standard deviation (%)	1	1	4	0

APPENDIX E: UNCERTAINTIES OF BET, ICP-MS, AND CHNS ANALYSES

MnOx/γ-alumina (10%) was selected to show the uncertainties of BET, ICP-MS, and CHNS analyses. Carbon content of 0.2 g of the same catalyst was measured after 150 minutes oxidation of toluene at room temperature by ozone. Inlet toluene and ozone concentrations were 120 and 1050 ppm, respectively. BET and ICP-MS data is presented in Table E.1 while Table E.2 shows the CHNS data.

Table E.1 MnO_x/γ-alumina (10%) BET and ICP-MS data

BET surface area (m^2 g^{-1})	Run #1	171
	Run #2	187
	Run #3	172
	Average (m^2 g^{-1})	177
	Standard deviation (m^2 g^{-1})	9
Pore volume (cm^3 g^{-1})	Run #1	0.51
	Run #2	0.52
	Run #3	0.49
	Average (cm^3 g^{-1})	0.51
	Standard deviation (cm^3 g^{-1})	0.02
Mn loading (wt%)	Run #1	9.8
	Run #2	9.2
	Average (wt%)	9.5
	Standard deviation (wt%)	0.4

Table E.2. Deposited carbon content of MnO_x/γ-alumina (10%) at room temperature

Carbon content (wt%)	Run #1	11.29
	Run #2	9.79
	Run #3	9.67
	Average (wt%)	10.25
	Standard deviation (wt%)	0.90

APPENDIX F: REDUCTION OF BIMETALLIC CATALYSTS BY HYDROGEN; XRD AND ACTIVITY

Pt-MnO_x/γ-alumina and Pd-MnO_x/γ-alumina were reduced by pure hydrogen at 250 ^oC for 2 hrs. The XRD spectra of the reduced catalysts are shown in Fig. F.1. It can be seen that all Mn_2O_3 and MnO_2 are transformed to MnO after the reduction.

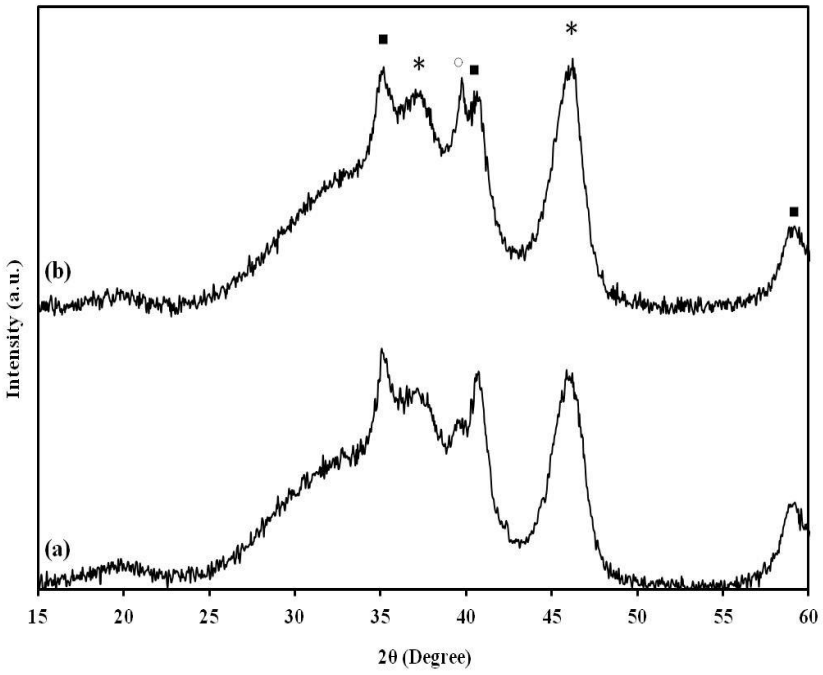

Fig. F.1. XRD spectra of reduced catalysts by hydrogen, (a) Pd-MnO_x/γ-alumina, (b) Pt-MnO_x/γ-alumina, *: γ-alumina, ○: Platinum, ▪: MnO.

The activity of the reduced and reduced catalysts are indicated in Fig. F.2 and Fig. F.3 in terms of toluene and ozone conversions, respectively. It can be seen that the reduced Pd-MnO_x/γ-alumina show almost the same activity as Pt-MnO_x/γ-alumina, implying that lower oxidation state of manganese (higher 3d electron occupancy) are more favorable in the oxidation of

toluene. It has to be noted that room temperature activities (22 ^{o}C) are reported after 150 min running the reaction.

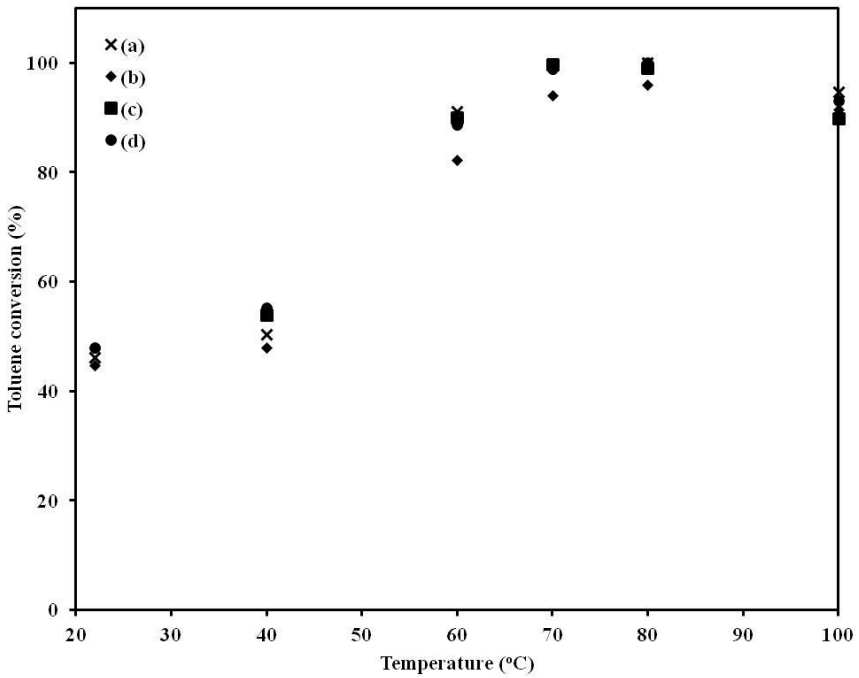

Fig. F.2. Toluene conversion, (a) Pt-MnO_x/γ-alumina (unreduced), (b) Pd-MnO_x/γ-alumina (unreduced), (c) Pd-Mn/γ-alumina (reduced), and (d) Pt-MnO_x/γ-alumina (reduced).

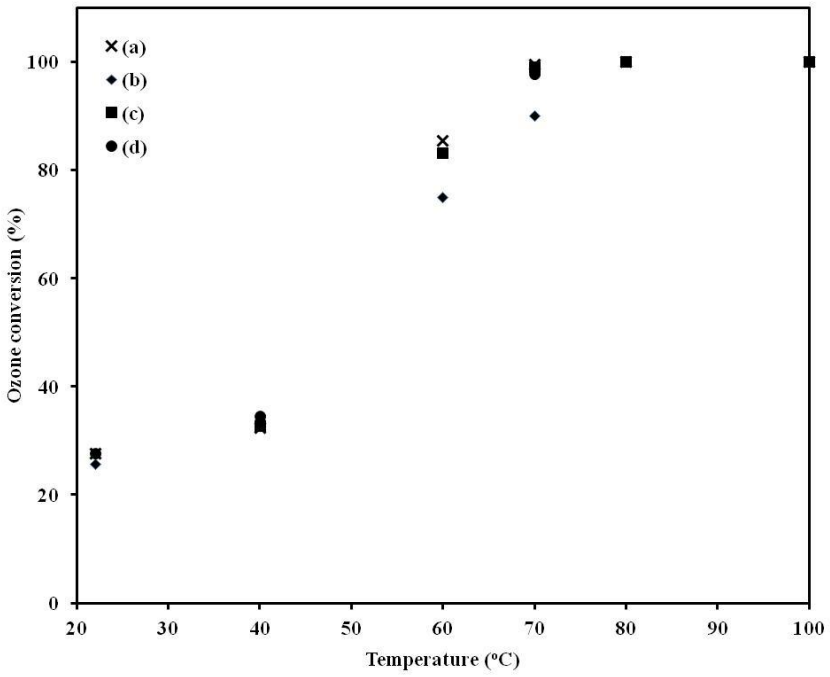

Fig. F.3. Ozone conversion, (a) Pt-MnO_x/γ-alumina (unreduced), (b) Pd-MnO_x/γ-alumina (unreduced), (c) Pd-Mn/γ-alumina (reduced), and (d) Pt-MnO_x/γ-alumina (reduced).